CHAPTER 6

THERMO-HYDRO-MECHANICAL OEDOMETER RESULTS

6.1 Stress and Strain State Variables under Isothermal Conditions used in the Research

6.1.1 General aspects of stress state variables

The approach followed in this research under isothermal conditions is to use two independent stress state variables to describe the volume change behaviour of isothermal, unsaturated and chemically inert clays: the net stress state variable (σ_{ij}-$u_a\delta_{ij}$) and the matric suction stress state variable (u_a-u_w)δ_{ij}, where the first tensor is the total stress, and u_a and u_w are the gas and liquid phase pressures (Bishop and Blight, 1963; Matyas and Radhakrishna, 1968; Fredlund and Morgenstern, 1977). This combination among others results advantageous because under a constant air pressure, which is the case of the experimental programme, the effects of a change in net stress inducing changes on contact forces between aggregates can be separated from the effects caused by pore-water pressure affecting soil skeleton via interface actions. In addition, uncertainty in only one stress variable is introduced when dealing with negative values of pore-water absolute pressures or when performing non-isothermal paths under restricted drainage conditions, where some water pressure build-up during the quasi-undrained stages is expected. For axially symmetric conditions, three independent stress parameters are defined: the net mean stress $p = (\sigma_v+2\sigma_h)/3-u_a = \sigma_m-u_a$, the deviatoric stress $q = \sigma_v-\sigma_h$ and the matric suction $s = u_a-u_w$, where σ_v and σ_h are the principal axial and radial total stresses, respectively. An additional independent macroscopic osmotic suction stress state variable $\pi\delta_{ij}$ has been proposed by Miller and Nelson (1992, 1993) to account for changes in soil states associated with changes in chemistry of soil solution. In addition, temperature requires to be incorporated as an additional state variable to tackle non-isothermal soil behaviour. The validity of the first-mentioned two stress state variables, which has produced an adequate description of unsaturated soil behaviour, has been demonstrated based on equilibrium equations of differential elements of a multiphase soil mixture and several null volume tests performed using axis translation technique and maintaining positive water pressures (Fredlund and Morgenstern, 1977). Recently, an experimental procedure under null deformation and water content change has been developed to validate this assumption in the case of negative water pressures measured with IC tensiometers, where the pore air pressure is modified and changes in matric suction and net stress are directly measured (Mongiovi and Tarantino, 1998).

Recent constitutive models have mainly followed this trend of using these two independent variables (Alonso *et al.*, 1990; Gens, 1993; Wheeler and Sivakumar, 1995; Maâtouk *et al.*, 1995; Wheeler, 1996; Cui and Delage, 1996; Thomas and He, 1998); however, some problems appear related to the transition from unsaturated and saturated state variables with adequate physical meaning. This way, under nearly saturated conditions, the effects of net stress and matric suction can be combined in a single intergranular stress with the following independent stress variables: $p' = (\sigma_m-u_a)+(u_a-u_w)$ and $s = u_a-u_w$, where the first expression recovers mean effective stress and the fact that a small change of suction has approximately the same effect as a change in net mean stress. A consistent set of experimental results at different temperatures is presented in Fig. 6.47 and Fig. 6.49 using these independent stress variables. At higher suction values the effects of net stress and suction on soil deformation are not equivalent and are preferable to treat them separately, as further discussed.

The proposal of a single-valued stress state variable is usually related to the direction first proposed by Bishop (1959): $\hat{\sigma}_{ij} = \sigma_{ij} - u_a \delta_{ij} + \chi(u_a - u_w)\delta_{ij}$, where χ is a material parameter via an effective area for matric suction action that mainly depends on degree of saturation. While this equation has been extensively used in describing shear strength behaviour (Fredlund *et al.*, 1995; Oloo and Fredlund, 1996; Vanapalli *et al.*, 1996; Öberg and Sällfors, 1997; Khalili and Khabbaz, 1998), it has several limitations (Edgar, 1993): first, χ is a function of the degree of saturation, the past stress history and the soil type, and secondly, the above expression uses a material property to define a stress state. Usually in non-active porous media, the state of stress (summation of forces) is separated from the material properties (constitutive properties). Another shortcoming of this single intergranular stress is that collapse behaviour as a result of wetting under high enough constant total stress is in apparent contradiction to this single stress variable. The addition of water increases the pore water pressure reducing the single intergranular stress, and hence expansion might be expected, which occurs at microscale (aggregate swelling) as well as at macroscale. Nevertheless, also at macroscale, the meta-stable aggregate packing rearranges due to shear contact failure caused by weakening of these contacts because capillary forces between aggregates become smaller, which originated the previous macrostructural swelling. As a consequence, soil skeleton loses its stiffness and displacements between aggregates take place reducing inter-aggregate pores. Mitchell (1993) suggested that this anomaly of volume decrease under decreasing single effective stress results because of the application of continuum concepts to a phenomenon that is controlled by particulate behaviour. Further experimental evidence indicating that the single-valued intergranular stress is inadequate for unsaturated soils is presented in Wheeler and Karube (1996) using critical state data.

As discussed in section 5.1.3, it appears that hysteretic hydraulic effects under the preponderance of inter-aggregate water may play an important role on mechanical behaviour specially in high and medium active clays, due to the different arrangements of soil water within the voids in main wetting and drying paths, affecting soil skeleton in different ways (Wheeler and Karube, 1996). In addition, the requirement of recovering effective stress assumption under nearly saturated conditions with a more appropriate transition from unsaturated to saturated states, have promote the need of generalising it to the case of partially saturated soils, but focusing in the use of more than one stress state variables. The incorporation of this water content (via a function of Sr or w) within at least one of the independent variables have been proposed in some constitutive models to describe deformational and strength behaviour (Jommi and Di Prisco, 1994, Bolzon *et al.*, 1996). With reference to Bishop's type intergranular stress, material parameter χ needs to decrease sharply with decreasing degree of saturation in order to separate the effects arising from applied net stresses and from matric suction. In addition, the purely mechanical concept of capillary pressure acting between aggregates is lost at higher suction values, where suction represents a conceptualisation of the energy status of water in soil (Gray and Hassanizadeh, 1991). Under these circumstances, it is inadequate to incorporate mechanistic stress variables with adsorption energy per unit volume in a single macroscopic stress state variable. Nevertheless, water under tension with absolute negative pressures (curved liquid-gas interface) is assumed to remain in a meta-stable state when the phase boundary is transgressed without the liquid changing phase, as indicated in section 4.1.1, where values lower than -2 MPa have been reported (refer to compiled values presented by Marinho and Chandler, 1995 and Guan *et al.*, 1998). Furthermore, following the ideas presented in section 5.1.1, water contained at intra-aggregate scale that accounts for 38% (high-porosity packing) and 59% (high-density fabric) of the total volume of water in soil, is not operative for matric suction action as a mechanical concept between aggregates. This way, as a first tentative and following Eq. (5.15), material parameter $\chi(Sr,e)$ is proposed as:

$$\chi(Sr,e) = \left\langle \frac{Sr - Gs.w_{ref}/e}{1 - Gs.w_{ref}/e} \right\rangle^{k} \qquad (6.1)$$

where $\langle\ \rangle$ designates the Macauly brackets applied to the effective bulk water saturation with reference to a cut-off degree of saturation, which is expressed in terms of the maximum quasi-immobile water content contained at intra-aggregate scale ($w_{ref} \approx 15\%$, according to the discussion presented in section 5.1.1). k is an empirical constant to efficiently blockade matric suction effects on intergranular stress at medium levels of saturation.

Drying paths performed under constant volume conditions (isochoric shrinkage pressure tests) presented in section 6.5 and in Romero *et al.* (1999b), allow to determine a weighting factor for matric suction effects of around $\chi(Se) = 0.52 \pm 0.25$ for both packings at a relatively high degree of saturation of around (89±8)%. In order to obtain equivalent values under the assumption of an effective free water saturation ratio, an empirical exponent of around $k \approx 3$ needs to be considered. Fredlund *et al.* (1995) and Vanapalli *et al.* (1996) proposed Θ^k for the contribution of matric suction to the intergranular normal stress for shear strength behaviour, where Θ stands for the normalised volumetric water content with respect to the residual volumetric water content and k is a soil parameter. According to these authors, k is close to 1 in silty soils, which is the case of the material tested in their experimental programme, but can be greater than 1 when plasticity increases (maximum values are around $k \approx 2.4$ for an unsaturated till).

Typical stress paths in a s : p plane for a wetting-drying-wetting cycle under oedometer conditions (lateral stress cell) and constant net vertical stress are presented in Fig. 6.1 for the stable high-density packing ($(\sigma_v - u_a) = 0.085$ MPa) and in Fig. 6.2 for the meta-stable high-porosity packing ($(\sigma_v - u_a) = 0.600$ MPa). Time evolution of water content has been converted into time evolution of mean matric suction using the retention curve plots presented in Fig. 5.20, Fig. 5.21, Fig. 5.26 and Fig. 5.27, and under the assumption that local equilibrium between liquid and vapour phases is reached despite the transient wetting stage. The relative characteristic times of vapour diffusion and of liquid flow in a typical macropore diameter scale of d = 1 μm is around $\tau_v / \tau_l = d\, k_w / D_a \approx 4 \times 10^{-13}$, considering a molecular diffusivity of water vapour in air of $D_a = 2.8 \times 10^{-5}$ m^2/s and a maximum water permeability of $k_w = 1 \times 10^{-11}$ m/s, which justifies the previous assumption (Milly, 1982). Stress state evolution of the high-density packing reaches a maximum net mean stress upon main wetting at a matric suction of around 0.5 MPa due to net lateral stress build-up. This maximum lateral stress can be associated to an incipient passive failure under a Mohr-Coulomb criterion at a relatively high value of $K_0 = (\sigma_h - u_a)/(\sigma_v - u_a) \approx 4.7$. With respect to the collapsible packing, the stress path reaches the loading-collapse LC yield surface (Alonso *et al.*, 1990) during main wetting, which is dragged along during imbibition originating a macrostructural strain hardening of soil structure. Equalisation values under steady state conditions are presented in both figures, where deviatoric stresses are also indicated. The following drying-wetting cycles of both packings, without considerably exceeding their air-entry values, show a remarkable elastic behaviour with a stress ratio between $\delta s/\delta p \approx -2.1$ for the high-density fabric and $\delta s/\delta p \approx -3.0$ for the high-porosity packing. These values correspond to $\delta u_w/\delta\sigma_h \approx$ (1.4 to 2.0) under $\delta\sigma_v = \delta u_a = 0$ conditions. Stress paths in a $\log s : \hat{p}$ (mean intergranular stress) plane for the same wetting-drying-wetting cycles are presented in Fig. 6.3 for the high-density packing and in Fig. 6.4 for the high-porosity packing. Stress state evolutions are indicated in terms of intergranular stresses using $\chi = Sr$ (dashed lines) and using the effective saturation with a reference cut-off water content of $w_{ref} = 15\%$ as previously indicated (solid lines). An exponent k = 1 has been selected. Stress paths using parameter $\chi = Sr$ display a monotonic decrease of intergranular stress during imbibition process for both packings. Nevertheless, the physical meaning of the high intergranular stress at the beginning of the path is not clear. The paths with parameter $\chi = Se$ start from nearly the initial net mean stress, evolving progressively towards higher intergranular stresses, due to the contribution of increasing saturation degrees, despite the decrement of suction. In the case of the high-density packing there is also a contribution from net mean stress increase. Finally, the stress paths are reverted due to the decrease in matric suction with no important degree of saturation change, tending towards the net mean stress values under nearly saturated conditions, with a stress variable ratio of around $\delta s/\delta\hat{p} \approx 0.78$ in the case of the high-density packing and around $\delta s/\delta\hat{p} \approx 0.53$

for the high-porosity fabric. Equalisation values under steady state conditions are presented in both figures, where deviatoric stresses are also indicated. The following main drying – scanning wetting cycles of both packings show a remarkable elastic behaviour within the nearly saturated zone. Typical stress variable ratios are around $\delta s/\delta\hat{p} \approx 3.12$ for the high-density fabric and $\delta s/\delta\hat{p} \approx 2.22$ for the high-porosity fabric.

As observed, the inclusion of the effects of hydraulic hysteresis within the mechanical stress state variables results in an additional complexity, mainly related to the physical interpretation of intergranular stress and to the difficulty of measuring degree of saturation changes in conventional suction controlled tests.

6.1.2 General aspects of work conjugate strain variables

External mechanical power input per unit volume of soil P_i, assuming that motions of air and water components related to the skeleton are slow and considering the porous material as a deformable open system, is given by the following expression (Alcoverro *et al.*, 1998):

$$P_i = \boldsymbol{\sigma} : \dot{\boldsymbol{\varepsilon}} + \rho_d \mu_a \dot{m}_a + \rho_d \mu_w \dot{m}_w \; ; \quad s(\mu_a, \mu_w) = u_a(\mu_a) - u_w(\mu_w) \tag{6.2}$$

where $\boldsymbol{\sigma}$ and $\boldsymbol{\varepsilon}$ are the total stress and strain tensor, μ_a (or μ_w) the chemical potential per unit mass of air (or water) that are related at a given temperature to the fluid pressures, and m_a (or m_w) is the specific mass (per unit mass of solid) of dry air (or water, both liquid and vapour) and ρ_d the dry density. The second expression corresponds to a global definition of suction, which incorporates the capability of a soil of retaining soil water as well as air. To release the absorbed and adsorbed water, as well as air, external energy has to be applied to counteract the water or air retention forces. For ideal mixtures, chemical potential μ_α can be identified with $\mu_\alpha = \psi_\alpha + (u/\rho)_\alpha$, where u_α , ρ_α and ψ_α are the pressure, mass density and specific free energy of the fluid α, respectively (Dangla and Coussy, 1996).

The work input corresponding to the term $\rho_d \mu_w \, \delta m_w$ under the approximation that water phase may be regarded as incompressible ($\mu_w = (u_w - u_{wo})/\rho_{wo}$, where u_{wo} is a reference pressure) is equivalent to $u_w \, \delta V_w/V$ or $u_w \, \delta\theta_w$, where the water pressure is associated to the volumetric water content change. This work input, which can be related to the work performed on water being pushed through the boundary of the system due to pressure action (piston analogy), can also be expressed in terms of the gravimetric water content change δw, which is usually preferred when performing experimental tests, specially at high temperatures: $u_w \, Gs \, \delta w/(1+e)$, where Gs is the specific gravity of soil particles at a specified temperature and e stands for void ratio.

Assuming an isotropic stress state σ_m, the work input to the soil per unit of initial volume δW by the application of total stress, water and air pressures, can be expressed in a simple way as (solid and water phases are regarded as incompressible):

$$\delta W = -\sigma_m \frac{\delta V}{V} + u_w \frac{\delta V_w}{V} + u_a \frac{\delta V_a}{V} + u_a \frac{V_a}{V} \frac{\delta \rho_a}{\rho_a} \quad \text{or}$$

$$\delta W = \sigma_m \delta \varepsilon_v + u_w \delta\theta_w + u_a \delta\theta_a + u_a \theta_a \frac{\delta \rho_a}{\rho_a} \tag{6.3}$$

$$\text{with} \quad \theta_w = n\,Sr \quad \text{and} \quad \theta_a = n(1 - Sr)$$

where positive compression doing positive work results in a volume decrease and ρ_a is the density of the air phase. Interfacial tension between water and air is not included, since the energy expended in deforming the interface is reflected in the different pressures of the two fluids (Edgar, 1993) or also

interpreted under the assumption of air-water menisci moving with soil skeleton (Houlsby, 1997). The above expression is equivalent to that proposed by Houlsby (1997), neglecting the work dissipated by the flow of water and air through the soil. The positive work input to compress the air phase is given by $u_a\,\theta_a\,\delta\rho_a/\rho_a$. Considering dry air mixture as an ideal gas, this term can be rewritten as $n(1-Sr)u_a/(u_a+u_{atm})\delta u_a$. This way, it appears that the first three terms of the expression of Eq. (6.3) are sufficiently adequate providing that usual experimental tests are carried out under $\delta u_a = 0$ conditions. Assuming incompressibility of solid material, total volume change is equivalent to the water and air phases volume changes (volumetric strain is only due to the variation of porosity in a Lagrangian sense as defined by Kaczmarek and Hueckel, 1998: $\delta\varepsilon_v = -\delta n$): $\delta V = \delta V_a + \delta V_w$, and the above expression may be rewritten as (work input to compress the air phase is not considered):

$$
\begin{aligned}
&\text{a) } \delta W = -(\sigma_m - u_a)\delta V/V - (u_a - u_w)\delta V_w/V = (\sigma_m - u_a)\delta\varepsilon_v - (u_a - u_w)\delta\theta_w \quad \text{or}\\
&\delta W = (\sigma_m - u_a)\delta\varepsilon_v - (u_a - u_w)(n\,\delta Sr - Sr\,\delta\varepsilon_v)\\
&\delta W = [(\sigma_m - u_a) + Sr(u_a - u_w)]\delta\varepsilon_v - (u_a - u_w)n\,\delta Sr\\
&\\
&\text{b) } \delta W = -(\sigma_m - u_w)\delta V/V + (u_a - u_w)\delta V_a/V = (\sigma_m - u_w)\delta\varepsilon_v + (u_a - u_w)\delta\theta_a\\
&\text{with } \delta\theta_a = -(1-Sr)\delta\varepsilon_v - n\delta Sr = -(\delta\varepsilon_v + \delta\theta_w)\\
&\\
&\text{c) } \delta W = -(\sigma_m - u_a)\delta V_a/V - (\sigma_m - u_w)\delta V_w/V = -(\sigma_m - u_a)\delta\theta_a - (\sigma_m - u_w)\delta\theta_w
\end{aligned}
\tag{6.4}
$$

which indicate the appropriate work conjugate extensive variables associated with the different combinations of significant intensive stress variables. Matric suction is work conjugated with the extensive strain variable $-n\,\delta Sr$ when dealing with Bishop's effective stress (Houlsby, 1997), while it is associated to $-\delta\theta_w = -n\,\delta Sr + Sr\,\delta\varepsilon_v$ when incorporating the net mean stress (Edgar, 1993; Wheeler and Sivakumar, 1995; Dangla *et al.*, 1997, Houlsby, 1997), or to $\delta\theta_a = -(\delta\varepsilon_v + \delta\theta_w)$ when working with effective stress (Edgar, 1993). In this research, $-\delta\theta_w = -Gs\,\delta w/(1+e) = -(\gamma_d/\gamma_w)\delta w$ has been selected as work conjugate extensive variable for matric suction, independently of dealing with net stress or intergranular stress as the second independent state variable. In the thesis, this work conjugate variable is normalised with respect to the initial soil volume $(1+e_o)$ following a Lagrangian description as defined by Kaczmarek and Hueckel (1998).

For principal net stress and principal strain increments, the work input to the sample ($\delta u_a \approx 0$ conditions) can be expressed as (equivalent to that proposed by Wheeler and Sivakumar, 1993):

$$\delta W = (\sigma_m - u_a)\delta\varepsilon_v + (\sigma_1 - \sigma_3)\delta\varepsilon_s - (u_a - u_w)\delta\theta_w \tag{6.5}$$

where $\delta\varepsilon_s = 2/3\,(\delta\varepsilon_1 - \delta\varepsilon_3)$ stands for the shear strain increment.

6.2 Suction Controlled Swell / Shrinkage under Constant Load Results on Low-Porosity Packings

6.2.1 Isothermal paths

6.2.1.1 General aspects. Main wetting and drying paths

Clay volume change behaviour is associated to swelling, shrinkage, collapse and compression phenomena caused by changes in applied stresses, changes in pore fluid pressures affecting moisture environment, temperature, chemical and time duration / strain rate effects. Chemically induced deformations on clay skeleton have not been analysed, although the dissolution / precipitation

phenomena and redistribution of soluble salts in response to thermal gradients (Bear and Gilman, 1995) may certainly induced additional physico-chemical interactions between pore water and clay microstructural organisation (Cuevas *et al.*, 1998). The existence of an important saline environment in the upper part of the samples in contact with the coarse porous stone at high temperatures, where water evaporation consequences are of certain consideration, is a fact that has been detected when dismantling the equipment and observing the specimens. Nevertheless, attention is focused on the effects induced by macroscopic state variables that are measurable or imposed on the boundary of the sample, i.e. to loading, suction and temperature effects. In addition, time effects are expected to be of lesser importance for processes of relatively short duration such as those followed in this research, where a constant strain rate of around, or somewhat less than, 10^{-8} s^{-1} at the end of the equalisation stages has been maintained (strain resolution / day). However, it is recognised that strain rate during creep increases with temperature (refer to the secondary swelling at low stress levels observed in Fig. 4.13, Fig. 4.14 and Fig. 4.15; as well as to the secondary compression at high stress levels observed in Fig. 4.17 and Fig. 4.18), and further aspects of ageing effects, both of skeleton viscosity and time-dependent flow of adsorbed water, have to be investigated. This way, control rate of strain tests at different temperatures and strain rates, such as those reported by Akagi and Komiya (1995) and Boudali *et al.* (1994), these last tests interpreted within a elasto-thermo-viscoplastic model by Oka *et al.* (1997), isothermal control rate of loading tests at constant suction and isothermal control rate of suction tests at constant net stress and at different temperatures, as well as creep-type tests at different matric suctions and temperatures, are required for extending the rheologic soil volume change behaviour.

A qualitative classification of unsaturated soils can be established according to their volumetric stability under stress, suction or temperature changes. Taking into account this pattern, they can be divided into stable structured packings (usually related to high-density packings with swelling tendency upon wetting and drained heating) and meta-stable packings (usually related to high-porosity packings with collapsible tendency upon wetting and compressive behaviour upon drained heating). In addition, changes in volume associated to a stable packing can cause changes in strength and deformation properties that influences further stability (destructuration of the stable packing). Swelling stable path as a result of the reduction of stress or the addition of water can be associated to a single intergranular stress (refer to section 6.1.1), though two independent stress variables are commonly used, and irreversible aspects are usually related to a suction decrease SD yield locus as originally defined by Gens and Alonso (1992). Secondary expansive phenomena as a consequence of aggregate hydration from inter-aggregate water transfer have been theoretically formulated by Alonso *et al.* (1989) and Alonso *et al.* (1991). However, even in these stable paths certain phenomena affecting the generalised swelling of a double porosity network can appear, such as inter-aggregate pore invasion in open macrostructures, which can arise to macroporosity decrease at expense of aggregate swelling, although the overall volume expansion is dominant. This mechanism has been described by Komine and Ogata (1994, 1996a), observed with electron microscopy by Komine and Ogata (1996b) and incorporated within an elastoplastic framework by Vaunat *et al.* (1998) and Alonso *et al.* (1998b).

On the phenomenological level, meta-stable collapse and drained thermal compression phenomena are not included in the elastic expressions because they are associated to the plastic behaviour of soil (slippage of inter-aggregate contacts and yielding of aggregations). Thermal strains in the normal consolidation range are usually considered within a thermoplastic hardening theory (Hueckel and Borsetto, 1990; Hueckel and Baldi, 1990; Seneviratne *et al.*, 1993; Robinet *et al.*, 1993, 1996a,b; Picard, 1994; Modaressi and Laloui, 1997) in an equivalent description given to the suction induced collapse (loading-collapse LC yield locus as defined by Alonso *et al.*, 1990). This way, temperature appears as a state parameter and as an internal variable modifying the yield surface, where usually it is admitted that during a drained heating process the yield locus shrinks at a rate governed by a thermal softening function and an uncoupled ductilisation effect controlling strain hardening through its dependence on the preconsolidation stress (refer to Fig. 7.42 and section 7.2.3). Gens (1995) presented a rate independent formulation including both suction and temperature induced effects,

mainly applicable to normally consolidated and slightly overconsolidated states, which has been implemented in a numerical code by García (1998). In addition, Modaressi and Modaressi (1995) combined a thermoplastic model with an elastoplastic model developed for unsaturated soils (Modaressi and AbouBekr, 1994a,b). Modaressi and Laloui (1992, 1993, 1997) extended the framework to a rate-dependent thermoviscoplastic constitutive model. Sultan *et al.* (1998) proposed additional plastic mechanisms to account for some limitations of existing models, namely to reproduce some thermal hardening phenomenon induced by heating on normally consolidated samples, also observed by Towhata *et al.* (1993) and Kuntiwattanakul *et al.* (1995) (heat-induced hardening on shear strength), and to reproduce thermal expanding – contracting behaviour at moderate overconsolidation ratios. The temperature at which the initial thermal volume change trend is reversed is dependent on the overconsolidation ratio, as experimentally observed by Sultan *et al.* (1998). However, heat-induced hardening or thermal preconsolidation effect has been a subject of certain controversy, mainly associated to the effects of pore-water dissipation upon quasi-drained heating (refer to the discussion by Burghignoli *et al.*, 1995 and closure by Towhata *et al.*, 1995). Experiments reported in the literature are usually not true drained tests, being pore-water dissipation allowed after thermal equilibrium has been established. This way, positive pore-water pressures could be generated during this quasi-drained stage originating certain unloading effect at constant total stress, which is reversed upon water pressure dissipation, and inducing certain tendency of detecting a higher preconsolidation pressure.

With respect to these meta-stable compression phenomena, as confining stress is increased the amount of collapse and drained thermal compression increases up to a certain maximum, decreasing afterwards, due to the impossibility of further rearrangement due to inter-aggregate porosity reduction (maximum collapse zone as observed in Fig. 6.40).

Shrinkage or suction consolidation, usually associated to aggregate interactions and rearrangements as a result of pore water tension developed by inter-aggregate receding capillary menisci, is described in section 5.1.7.2 in a parallel qualitative framework related to water content changes. Irreversible aspects associated to a suction increase SI yield locus as defined by Alonso *et al.* (1990) and associated to the air-entry value, a property inherent to the packing and not to the maximum fabrication or past suction ever experienced by the soil, are further presented and discussed.

In this section, swelling / shrinkage behaviour under the isothermal wetting and drying paths indicated in Fig. 4.6 and carried out on the different oedometer cells described in section 3.2, are presented and discussed. Experimental tests have been represented in different stress state planes and independent on any model adopted. Therefore, only limited reference is made to any specific constitutive function. For a more detailed description, the reader is referred to the original formulations.

Time evolution of typical oedometer test results (both volumetric strain and water content change) conducted on these heavily overconsolidated packings in main wetting paths at two different temperatures are presented in Fig. 4.13 and Fig. 4.14. These plots indicate that suction induced volume changes at 22°C are smaller than at 80°C. Time evolution of volumetric strain, net lateral stress, water content and degree of saturation at 22°C for different matric suction steps along the complete wetting-drying-wetting process obtained with the lateral stress oedometer cell are indicated in Fig. 6.5 and Fig. 6.6. In general, a monotonic evolution is observed for this stable packing in the first wetting phase. However, net lateral stress evolution reaches a maximum at some intermediate state tending gradually to somewhat lower values under steady state conditions. This aspect, mainly related to the main wetting stage, can be associated to a spurious experimental problem caused by the sensitivity of the lateral stress system to the pressure distribution along the ring wall as suggested by Jucá and Frydman (1996). Early lateral stress readings result from a concentrated lateral load acting on the wetted lower part of the ring, which tends to advance gradually with time covering a higher area of application. This way, it seems that steady state values acting over the height are more representative of calibration curves obtained by air pressure application (refer to section 3.2.3.1). In addition, relatively high values of K_0 are consistent with results reported by Ofer (1981) for this type

of compensating system, where the soil is first allowed to swell at a small magnitude (related to an active lateral pressure) and then brought back to a condition of zero lateral strain (more related to a passive lateral pressure), which is the pressure being measured. Quasi-reversible features without significantly exceeding air-entry value are detected in the main drying-scanning wetting paths represented in Fig. 6.6, where the net lateral pressure is cancelled when a suction of 0.45 MPa is reached. The results corresponding to the equalisation stages are indicated in Fig. 6.7, where main features of irreversible expansion upon main wetting and somewhat irreversible shrinkage upon main drying are detected. Couplings between volume change behaviour and water content changes are readily observed.

Fig. 6.8 shows the comparison of swelling strains, water content and degree of saturation changes for two different temperatures developed during wetting-drying-wetting paths under a constant net vertical stress of $(\sigma_v\text{-}u_a) = 0.026$ MPa, where suction induced volume and water content changes upon main wetting are smaller at lower temperatures. Similar patterns of behaviour are observed in Fig. 6.9 ($(\sigma_v–u_a) = 0.085$ MPa), in Fig. 6.10 ($(\sigma_v–u_a) = 0.300$ MPa) and in Fig. 6.11 ($(\sigma_v–u_a) = 0.550$ MPa). An overall comparison in terms of volume change behaviour is indicated in Fig. 6.12, where higher suction induced swelling and shrinkage deformations are observed at higher temperatures. Clear irreversible features upon main wetting and main drying are observed at lower net vertical stresses. Swelling under load curves for two different temperatures departing from the initial state are shown in Fig. 6.13. The initial vertical overconsolidation ratio OCR_{vo} at 22°C varies between 173 and 8 for the different paths (refer to Fig. 4.6) and reaches a ratio OCR_{vs} between 27 and nearly 1 on arriving to saturated conditions. These last values are estimated based on an average saturated preconsolidation pressure of $(\sigma_v - u_a)_o^* \approx 0.7$ MPa, which is reached after the progressive softening of the sample during wetting and calculated from constant volume suction controlled swelling pressure tests presented in section 6.5. However, lower saturated preconsolidation pressures are expected upon main wetting in the less loaded specimens and at higher temperatures, due to macrostructural volumetric strain softening effects on clay skeleton induced by the irreversible swelling as suggested by Gens and Alonso (1992). A somewhat lower swelling pressure of around 0.5 MPa to that indicated in Fig. 2.33 (around 0.6 MPa), which started from hygroscopic humidity, is detected from swell under load results. This fact shows some small dependence of initial water content on swelling pressure for these stable packings. In addition, this swell under load swelling pressure is lower than that determined with the constant volume method (around 0.7 MPa), which at the same time are both lower than the swelling pressure value of 0.8 MPa estimated by the loading after free swell method reported in section 2.6.2.2 departing from the same initial humidity. These results show stress path dependence as suggested by Gens and Alonso (1992) and Gens (1993), who analysed this dependence within an elastoplastic model, and are consistent with swelling pressure results reported by Justo *et al.* (1984), Sridharan *et al.* (1986), El-Sohby *et al.* (1989) and Feng *et al.* (1998). Results are also influenced by the testing procedure, since the loading after swell and the swell under load methods are very sensible to lateral friction spurious effects, as commented in section 4.5.1. In addition, constant volume methods depend on the apparatus deformability, testing and correction procedures followed, giving usually intermediate values between the maximum pressure of the loading after swell method and the swell under load result (Justo *et al.*, 1984; Sridharan *et al.*, 1986; Feng *et al.*, 1998) or higher values (El-Sohby *et al.* 1989; Feng *et al.*, 1998). Also, swelling pressure as reported by swell under load results seems not to be greatly affected by temperature. This is consistent with observations presented by Pusch *et al.* (1991), who detected no increase in swelling pressure during temperature change in low-porosity clays.

Fig. 6.14 presents the results of measured water content and degree of saturation values (determined in a free water sense) under steady state conditions for the different matric suction steps followed during main wetting. The constant volume swelling pressure path presented in section 6.5, as well as its different equalisation stages, are also plotted in the previous figure. Greater water content changes induced by suction changes upon main wetting are associated with the hotter specimens, in agreement with volumetric strain results. However, at higher net vertical stresses and consequently lower

volumetric changes, this trend is reversed due in part to the smaller storage capacity of water mass due to thermal dilatation that offers the hotter soil. Also, higher equalisation degrees of saturation are detected at higher temperatures, condition that is more remarkable at low net vertical stresses and higher suctions. These isothermal results are consistent with non-isothermal test data presented in section 6.2.2. Water content and degree of saturation values under steady state conditions for the different matric suction steps during main drying are indicated in Fig. 6.15. Constant volume shrinkage pressure paths at 22°C without surpassing the air-entry value of the packing are also represented. A striking aspect is that equalisation results are reversed with respect to the previous results, showing that the air-entry value of the packing that is associated to the suction increase yielding, is reached before under low net vertical stresses and high temperatures, where lower degrees of saturation are detected. In appendix A, low-vacuum environmental scanning photomicrographs (ESEM at × 2500) at absolute pressures over the water triple point pressure (> 4.58 torr) are presented for a high-density aggregate in a wetting path (apparent relative humidity from 28% up to 81%). A maximum swelling strain of around 12% obtained from 2-D image analysis complements the information of aggregate swelling at microscale. Further aspects of the wetting path, sample preparation and equipment description are indicated in this appendix. Controlled drying tests after main wetting are being currently analysed to observe irreversible features and spurious experimental aspects, but they are not included in the thesis.

Total and reversible swelling and shrinkage strains measured in a suction cycle (0.45 MPa → 0.01 MPa → 0.45 MPa) at a constant net vertical stress of 0.026 MPa and at 80°C are shown in Fig. 6.16. The existence of important plastic swelling deformations associated with the first suction reduction is a relevant feature of the data. After main wetting, the drying-wetting path shows again a remarkable plastic shrinkage behaviour. An apparent yield suction s_I may be identified in Fig. 6.16, where irreversible strains are detected for matric suctions higher than this air-entry value. Finally, under further suction change cycles the specimen presents a quasi-elastic behaviour with some hysteretic loop. On the drying path, when the air overpressure is maintained above the soil air-entry point, the degree of saturation decreases sharply, expelling a certain amount of inter-aggregate water that is not recoverable upon subsequent wetting due to irrecoverable effects on clay skeleton induced by oblique intergranular forces exceeding the shear strength between aggregates. This desaturation pressure (activation of the suction increase SI yield locus as originally defined by Alonso *et al.*, 1990), which appears mainly dependent on inter-aggregate voids with the widest entry routes, increases with the applied vertical stress as indicated in Fig. 6.17, in a consistent way according to the previous history of wetting. The heated and less loaded samples experience higher swelling strains upon main wetting that affect in an irreversible way clay skeleton, inducing a more open structure and developing larger macropores, which present a smaller air-entry value and consequently a smaller yield shrinkage suction. Within an elastoplastic point of view, this condition is associated to a macrostructural softening induced by the activation of the suction decrease SD yield locus as defined by Gens and Alonso (1992) upon main wetting, which affects via volumetric plastic strain the position of the suction increase SI yield locus. In addition, SI yield locus is sensible to temperature, where a lower air-entry value under surface-tension reasoning is expected at higher temperatures. All these effects acting on the meniscus mechanism at inter-aggregate level may be expressed as:

$$\mathrm{SI}:\ s - \left[s_o + \langle \mathrm{Se} \rangle^k \left(s_I(\varepsilon_v^p, \Delta T) - s_o \right) \right] = 0 \tag{6.6}$$

where $\langle \mathrm{Se} \rangle$ designates the Macauly brackets applied to the effective bulk water saturation as defined by Eq. (5.15), k is an empirical constant and ΔT stands for the temperature difference with respect to a reference state. Under low effective saturation ratios, $s \approx s_o$ has the meaning of the maximum past suction ever experienced by the soil ($s_o \approx 1.9$ MPa arising from the water content maintained during the compaction process). However, during the main wetting process this suction increase yield locus is progressively lowered attaining soil packing air-entry value under nearly saturated conditions:

$s \approx s_I(\varepsilon_v^p, \Delta T)$ (the yield limit has been reduced without implying that yielding has taken place). This yield locus under isothermal conditions is further modified according to the hardening law: $\delta s_I = [(1+e_o)(s_I + p_{atm})/(\lambda_s - \kappa_s)]\delta\varepsilon_v^p$ (Alonso *et al.*, 1990), where λ_s is the post-yield compressibility parameter for changes in suction when the air-entry zone is surpassed, κ_s is the elastic compressibility parameter under nearly saturated conditions and p_{atm} a reference atmospheric pressure. The concept of yield suction upon main drying being substantially lower than the maximum suction experienced by the sample during compaction has also been considered by Sivakumar and Ng (1998). In addition, recent experimental results confirm that SI is somewhat inclined at a positive angle in the s : p space (Sivakumar and Ng, 1998). Temperature effects acting on SI yield locus have also been proposed by Navarro (1997).

Total and reversible swelling and shrinkage strains measured in a suction cycle (0.45 MPa → 0.01 MPa → 0.45 MPa) at different net vertical stresses and different temperatures are shown in Fig. 6.18 and Fig. 6.19. Total swelling strains are higher at elevated temperatures, condition that is more obvious at low stress levels. Also, reversible strains are somewhat higher at elevated temperatures, tending to lower differences at elevated stress levels. Friction effects affecting volumetric strains are readily observed in the previous figures, reason why it is very important to maintain a constant height to radius ratio in order to detect temperature effects. As expected for the strong coupling with water content changes, shrinkage strains are more important at higher temperatures, in consistency with the arguments previously outlined. Irreversible features, both under main wetting and main drying paths, are also more significant at higher temperatures, as indicated in Fig. 6.20 and Fig. 6.21. The main wetting volumetric results due to the activation of a suction decrease SD yield locus offer a consistent pattern of plastic deformations as the external load is increased, offering an interesting challenge for constitutive modelling in terms of the actual overconsolidation ratio. This expression is proposed for scaling elastic deformations, following microstructural volumetric strain scaling as suggested by Gens (1993) and Alonso *et al.* (1994):

$$\frac{\delta\varepsilon_v^p}{\delta\varepsilon_v^e} = t_D\left(1 - \frac{(\sigma_v - u_a)}{(\sigma_v - u_a)_o^*}\right)^{n_D} \tag{6.7}$$

where net vertical stresses are normalised with respect to a reference preconsolidation stress of the original packing for saturated conditions $(\sigma_v - u_a)_o^* \approx 0.7$ MPa , and t_D and n_D are model parameters. Typical values of these parameters are $t_D \approx 1.26$ and $n_D \approx 2.94$ at 22°C, and $t_D \approx 1.29$ and $n_D \approx 0.80$ at 80°C, according to results presented in Fig. 6.20, where a higher thermal sensitivity is reflected on parameter n_D. An equivalent plot of volumetric plastic strains in the main shrinkage path is followed in Fig. 6.21, where volumetric strain ratios do not display so good consistent patterns of behaviour in terms of overconsolidation ratios and higher volumetric strain ratios are detected at higher temperatures. Two reference preconsolidation stresses have been selected: a constant value of $(\sigma_v - u_a)_o^* \approx 0.7$ MPa, corresponding to the original packing and represented in small symbols, and after the global macrostructural softening induced by the main wetting (strain softening) and main drying (strain hardening) cycle and represented in bigger symbols. Typical values of saturated preconsolidation stresses after a main wetting – main drying cycle are indicated in Fig. 6.58, where a value of $(\sigma_v - u_a)_o^* \approx 0.20$ MPa is selected at 22°C for the net macrostructural softening at $(\sigma_v - u_a) = 0.026$ MPa, and a value of $(\sigma_v - u_a)_o^* \approx 0.35$ MPa is considered at $(\sigma_v - u_a) = 0.085$ MPa.

6.2.1.2 Reversible features under nearly saturated conditions

Reversible volume change features under isothermal conditions are associated within an aggregated material to macrostructural effects mainly caused by changes in inter-aggregation forces and deformations of aggregation of particles, which can be expressed in a general form as:

$$\delta\varepsilon_v^e = (1-\chi)\left[\frac{\delta p}{K_p}+\frac{\delta s}{K_s}\right]+\chi\frac{\delta(p+\chi s)}{K_{p+s}}$$
$$K_p=\frac{(1+e_o)p}{\kappa};\quad K_s=\frac{(1+e_o)(s+p_{atm})}{\kappa_s};\quad K_{p+s}=\frac{(1+e_o)(p+\chi s)}{\kappa} \tag{6.8}$$

where the first term recovers at low degrees of saturation (preponderance of meniscus water) the non-linear isotropic elastic expression proposed by Alonso *et al.* (1990) for macrostructural elastic behaviour expressed as a function of net mean stress and suction. Bulk moduli due to net stress and suction changes are expressed in terms of the slope of the unloading-reloading line in a v – ln(p) diagram (κ) and the slope of the reversible wetting-drying line in a v – ln(s) diagram (κ_s), with p_{atm} being a reference atmospheric pressure. At nearly saturated states (preponderance of bulk water), the effective stress is recovered, where a change of suction has approximately the same effect as a change of net mean stress of the same magnitude. Similar concepts have been recently proposed by Wheeler (1997a), when studying elastic volume changes under the preponderance of bulk water. In addition, some small pre-yield compressibility decrease (κ) is detected with increasing suction, as observed in Fig. 6.67.

Isothermal changes in elastic strain associated with changes in intergranular vertical stress $\delta\varepsilon_v^e/\delta[(\sigma_v-u_a)+(u_a-u_w)]$ under nearly saturated states ($\chi\rightarrow 1$) are represented in Fig. 6.22 for constant (σ_v-u_a) data and in Fig. 6.23 for constant (u_a-u_w) data, where the following interpolations are obtained (represented with wider lines and indicated with letter A):

$$\left.\frac{\delta\varepsilon_v^e}{\delta[(\sigma_v-u_a)+(u_a-u_w)]}\right|_{T=const}=\frac{0.0118}{(\sigma_v-u_a)+(u_a-u_w)}\quad\text{at}\quad T=22^oC$$
$$\left.\frac{\delta\varepsilon_v^e}{\delta[(\sigma_v-u_a)+(u_a-u_w)]}\right|_{T=const}=\frac{0.0149}{(\sigma_v-u_a)+(u_a-u_w)}\quad\text{at}\quad T=80^oC \tag{6.9}$$

The first result is associated to $\kappa_{oed}\approx 0.019$, whereas a somewhat higher value of $\kappa_{oed}\approx 0.024$ is obtained at 80°C, which adequately correspond to κ_{oed} values obtained from unloading oedometer tests under constant suction (refer to Fig. 6.57, where subscript oed refers to oedometer conditions). Another type of interpolation (represented with letter B) has also been adopted: $\varepsilon_v^e=\beta_m\exp[\alpha_m(p+s)]$, following the proposal of microstructural elastic volumetric strains outlined in Gens (1993):

$$\left.\frac{\delta\varepsilon_v^e}{\delta[(\sigma_v-u_a)+(u_a-u_w)]}\right|_{T=const}=0.406\exp[-11.1((\sigma_v-u_a)+(u_a-u_w)]\quad\text{at}\quad 22^oC$$
$$\left.\frac{\delta\varepsilon_v^e}{\delta[(\sigma_v-u_a)+(u_a-u_w)]}\right|_{T=const}=0.406\exp[-8.83((\sigma_v-u_a)+(u_a-u_w)]\quad\text{at}\quad 80^oC \tag{6.10}$$

where intergranular vertical stress is expressed in MPa and temperature effects are mainly affecting α_m parameter. However, Eq. (6.9) is preferred since it is equivalent to the expression for elastic

volume change in saturated soils according to the modified Cam-clay model (Wood, 1990). In addition, this equation is recovered in section 7.1.1.3 within a simple mechanical-physicochemical model under nearly saturated conditions, relating it under certain hypothesis to the specific surface, pore fluid properties and concentration and valence of the prevailing ion via double layer thickness.

Isothermal reversible changes in work conjugate extensive variable of matric suction with changes in intergranular vertical stress $[Gs/(1+e_o)]\delta\varepsilon_v^e/\delta[(\sigma_v - u_a)+(u_a - u_w)]$ under nearly saturated states are represented in Fig. 6.24 for constant (σ_v-u_a) and (u_a-u_w) data. The following interpolations are obtained:

$$\left.\frac{[Gs/(1+e_o)]\delta w_e}{\delta[(\sigma_v - u_a)+(u_a - u_w)]}\right|_{T=const} = -\frac{0.021}{(\sigma_v - u_a)+(u_a - u_w)} \quad \text{at} \quad T = 22^oC$$
$$\left.\frac{[Gs/(1+e_o)]\delta w_e}{\delta[(\sigma_v - u_a)+(u_a - u_w)]}\right|_{T=const} = -\frac{0.034}{(\sigma_v - u_a)+(u_a - u_w)} \quad \text{at} \quad T = 80^oC \qquad (6.11)$$

where consistently higher values are obtained at higher temperatures and mainly at low net vertical stresses. Further aspects of the pre-yield compressibility parameter in terms of water content changes ($\kappa_w = -Gs\,\delta w/\delta \ln p$) and under nearly saturated conditions are indicated in section 6.4.1 (refer to Fig. 6.50) and in section 6.4.2 (refer to Fig. 6.59). Higher compressibility parameters in terms of water content changes are obtained from the previous curve fitting results ($\kappa_w \approx 0.033$ at 22°C and $\kappa_w \approx 0.053$ at 80°C) if compared with the equivalent values obtained from Eq. (6.9), purportedly related to the resolution of the experimental technique with reference to water content readability (refer to section 3.2.2). As indicated in Fig. 6.50, similar pre-yield compressibility values in terms of water content changes and skeleton deformation are expected. However, the general trend of obtaining higher compressibility values at elevated temperatures is detected.

6.2.1.3 Thermal induced reversible features under nearly saturated conditions (isothermal data)

Quasi-reversible phenomena during drained heating can be associated at aggregate level to expansion of the mineralogical components and the remaining adsorbed water, which is admitted to be lower than that of free water as suggested by Baldi *et al.* (1988), physico-chemical changes on diffusive double layers (repulsion of adjacent stacks are expected to increase in analogy to heat-induced increase in osmotic pressure) and certain particle rearrangement, since expanding bulk water is free to leave the clay mass. Although the effects of heating on adsorbed water are not well understood, it has also been suggested that temperature rise can reduce the thickness of double-layers (Morin and Silva, 1984) causing a reduction in interparticle distances. In addition, increasing temperatures appear to generate structural disturbances of the interlayer water lattice in clays at temperatures above 70°C (Ma and Hueckel, 1992, 1993; Zhang *et al.*, 1993), and consequently inducing aggregate contraction upon heating due to a denser grouping of stacks of flakes and favouring the transition from adsorbed water to free water. Therefore, the thermal loading generates two opposite microscopic mechanisms affecting thermal expansion, which can even induce positive thermal expansion coefficients due to clay dehydration effects. Another reversible deformational effect occurs at macroscale where thermal induced actions affect clay skeleton, as well as changes in inter-aggregation forces. The contribution of all these mechanisms have shown to be dependent on temperature and on stress state or overconsolidation ratio (Baldi *et al.*, 1988; Hueckel and Borsetto, 1990; Seneviratne *et al.*, 1993; Robinet *et al*., 1996b; Modaressi and Laloui, 1997).

Thermal induced reversible features under nearly saturated conditions can be inferred from isothermal reversible strain data implying a constant temperature difference of $\Delta T = 58$°C. For test conditions

prevailing at constant intergranular stress level $\hat{p}$, this reversible volumetric thermal strain ε_v^e is given in incremental form, following a similar expression to that described in Baldi *et al.* (1988), as:

$$\varepsilon_v^e = \varepsilon_v^e\left(\ln(\hat{p}/\hat{p}_r), \Delta T\right)$$
$$\left.\frac{\delta\varepsilon_v^e}{\delta T}\right|_{\hat{p}} = \alpha(\Delta T, \hat{p}) = \alpha_m + \alpha_o(\hat{p}) + \alpha_1(\hat{p})\Delta T \quad \text{with} \quad \alpha_i(\hat{p}) = \alpha_i^a + \alpha_i^b \ln\frac{\hat{p}}{\hat{p}_r} \tag{6.12}$$

where $\Delta T = T - T_r$ is the temperature difference with respect to a reference state and $\hat{p}_r$ a reference intergranular stress. The drained thermal expansion coefficient $\alpha(\Delta T, \hat{p})$ includes that of the clay solid mineral α_m, which is assumed not to depend on stress level, and that of the porous skeleton ($\alpha - \alpha_m$), dependent on stress state or stress ratio and temperature. Linear thermal expansion coefficients of clay minerals have been studied by McKinstry (1965). Volumetric coefficient of expansion is given by $\alpha_m = \alpha_1 + 2\alpha_2$, with typical values of $\alpha_1 = -(18.6\pm1.3)\times10^{-6}$ °C^{-1} (perpendicular to layering), $\alpha_2 = -(5.2\pm1.7)\times10^{-6}$ °C^{-1} (parallel to layering) and $\alpha_m = -(2.90\pm0.47)\times10^{-5}$ °C^{-1} for a kaolinite. Numerical values of above parameters under isotropic stress states and non-isothermal paths are indicated in section 7.2.3. Drained reversible thermal coefficients under constant net vertical stress are represented in Fig. 6.25 for high-density and high-porosity data under a constant $\Delta T = 58$°C (isothermal tests). Reversible data for cooling - heating cycles at constant $(\sigma_v - u_a) = 0.026$ MPa and different constant matric suction values, which are presented in section 6.2.2, are also indicated. The following expression approximately represents data trend for $\Delta T = 58$°C conditions:

$$\alpha(\Delta T = 58^o\text{C}, \hat{\sigma}_v) = \left[-(5.7\pm1.9) + 1.1\ln\left(\frac{\hat{\sigma}_v}{0.01\,\text{MPa}}\right)\right]\times10^{-5}\ {}^o\text{C}^{-1}$$
$$\alpha_m + \alpha_o^a + \Delta T\alpha_1^a = -(5.7\pm1.9)\times10^{-5}\ {}^o\text{C}^{-1}; \quad \alpha_o^b + \Delta T\alpha_1^b = 1.1\times10^{-5}\ {}^o\text{C}^{-1} \text{ at } \Delta T = 58^o\text{C} \tag{6.13}$$

where $\hat{\sigma}_v$ represents the vertical intergranular stress. Drained thermal expansion coefficient is observed to be dependent on stress level or in a more generalised way with the actual overconsolidation ratio to introduce certain dependence on hardening parameters under a coupled elastoplasticity concept. This drained thermal expansion coefficient also varies with temperature as discussed and presented in section 7.2.3, but no conclusive trend is detected in the previous figure.

To ensure that the experimental functions of Eq. (6.9) (intergranular stress changes at constant temperature and $\chi \to 1$) and Eq. (6.12) (heating step at constant intergranular stress) are derivable from a unique relationship, the equality of the second order mixed derivatives of both experimental functions should be imposed, assuming continuous experimental functions (Baldi *et al.*, 1988). From Eq. (6.12) and Eq. (6.9), result the following functions:

$$\frac{\hat{p}\delta\alpha(\Delta T, \hat{p})}{\delta\hat{p}} = \alpha_o^b + \Delta T\alpha_1^b$$
$$\frac{\hat{p}\delta\varepsilon_v^e}{\delta\hat{p}} = \frac{\kappa(\Delta T)}{1+e_o} = \frac{\kappa_{T_o}}{1+e_o} + \alpha_o^b\Delta T + \frac{\alpha_1^b}{2}\Delta T^2; \quad \frac{\delta\kappa(\Delta T)}{(1+e_o)\delta T} = \alpha_o^b + \Delta T\alpha_1^b \tag{6.14}$$

According to experimental values of κ at different temperatures presented in the previous section (refer also to Fig. 6.57), and the relationships between coefficients reported in Eq. (6.13), the following coefficients are obtained:

$$\kappa_{T_o} \approx 0.019; \quad \alpha_o^b \approx 9.59\times10^{-5}\ {}^o\text{C}^{-1}; \quad \alpha_1^b \approx -1.46\times10^{-6}\ {}^o\text{C}^{-2} \tag{6.15}$$

The following expression for thermal induced reversible features under nearly saturated conditions can be obtained from isothermal reversible water content data presented in Fig. 6.26, implying a constant temperature difference of $\Delta T = 58°C$ and different constant vertical intergranular stress values (reversible cooling – heating data at constant $(\sigma_v\text{-}u_a) = 0.026$ MPa, different constant suction values and $\Delta T = 58°C$ are also represented in the previous figure):

$$\frac{\overline{Gs}}{1+e_o}\frac{\delta w_e}{\delta T}\bigg|_{\hat{\sigma}_v} = \left[(26.7 \pm 6.1) - 5.3\ln\left(\frac{\hat{\sigma}_v}{0.01\,\text{MPa}}\right)\right]\times 10^{-5}\ {}^{o}\text{C}^{-1} \quad \text{for} \quad \Delta T = 58^{o}\,\text{C} \tag{6.16}$$

where $\hat{\sigma}_v$ represents the vertical intergranular stress and $\overline{Gs} \approx 2.73$ an average specific gravity of soil grains representative of the temperature range. As observed, temperature induced reversible features on water content changes are shown to be dependent on intergranular stress level and ΔT, following an equivalent expression to that given for the drained thermal expansion coefficient (Eq. (6.12)).

6.2.2 Non-isothermal paths

Non-isothermal paths have been carried out on the calibrated thermal oedometer cells, according to the experimental procedure outlined in section 4.2.1. Fig. 6.27 shows time evolution of corrected volumetric strain, water content and degree of saturation during a drained heating path at constant $(\sigma_v\text{-}u_a) = 0.026$ MPa and $(u_a\text{-}u_w) = 0.20$ MPa, where a monotonic increase in water content, degree of saturation (calculated in a free water sense according to section 3.2.4.2) and volumetric strain is detected in accordance to Fig. 6.13 and Fig. 6.14. It is important to indicate that initial stages are not true drained paths with prevailing restricted drainage conditions due to soil permeability and ceramic disc impedance effects, being pore-water dissipation allowed after thermal equilibrium has been established. Pore-water pressure build-up is generated during this initial quasi-undrained stage inducing certain matric suction decrease. This way, multiple heating stages and slow heating rates are imposed in order to minimise pore-water pressure perturbations and to maintain pressure changes below matric suction in such a way that no water overpressure is generated. The increase in pore-water pressure with no change in boundary confining stress is analysed in section 7.2.1 assuming volumetric compatibility between soil matrix and its constituents and taking into account both thermal expansion and compressibility coefficients.

Corrections have been applied according to section 3.2.4.2, where aspects of volumetric strain results possibly affected by a certain loss of K_0 condition during heating-cooling cycles caused by ring expansion and contraction are also discussed. Early quasi-undrained heating stages and evaporative fluxes under steady state conditions are also indicated in the previous figure. Fig. 6.28 shows another drained heating path performed at constant $(u_a\text{-}u_w) = 0.06$ MPa. Very marked stress-path dependence is observed in Fig. 6.29 under drained heating-cooling-heating cycles, where reversible and irreversible components of volumetric strains and matric suction work conjugate variable are identified along these paths. It is assumed that clay aggregates formed during dry-side compaction deform in a quasi-reversible manner upon main wetting and main heating paths and depending on stress state, affecting in an irreversible way the rearrangement of the macrostructure of clay skeleton, whose effects are not erased by the following stage of quasi-reversible cooling and heating paths. However, irreversible features on clay skeleton are not solely explained in terms of this last aspect, because at inter-aggregate level and according to macroscopic experimental measurements, free water content increases during heating. This swell potential induced by temperature due to water sorption was also observed in bentonite : sand mixtures by Sherif *et al.* (1982). It is expected that the larger swelling strains that experience the hotter samples under heavily overconsolidated states are probably more associated at aggregate level with this last mechanism of dilatancy due to water sorption and its effect on inter-aggregate pores. Quasi-reversible cooling and heating paths appear to accumulate strains as observed in Fig. 6.29, following a similar trend to strain accumulation during suction cycles (Pousada,

1984). This aspect has also been observed in FEBEX bentonite tested in the laboratory, but further experimental results are needed to verify this fact. This phenomenon appears to be related to the different mechanisms of clay swelling: water sorption between layers until a maximum and further subdivision of clay particles increasing the distances between them, as observed by Saiyouri *et al.* (1998) on high-density smectitic clays.

A striking aspect in Fig. 6.29 is the apparent overconsolidation effect detected at higher suction values and lower temperatures, where a clear yield point is found. The first heating stage up to 40°C takes place without an appreciable volumetric strain and water content increase. Nevertheless, when surpassing this temperature the volumetric deformations and water content variations increase remarkably, tending to open the macrostructure and activate a yield surface that generates the development of irreversible volumetric strains. This yield surface is associated to the suction decrease SD yield locus, as defined for isothermal conditions by Gens and Alonso (1992) and Gens (1993), which is inclined (parallel to the neutral line with constant intergranular stress) in a s : p plane. When the stress path reaches this SD yield curve, which is admitted to depend on temperature as further indicated, a further reduction of $p + \chi s$ or an increase in temperature leads to plastic swelling of the macrostructure, coupled to an inward movement of the LC yield curve (macrostructural strain softening) and to an downward movement of the SI yield locus inducing a lower air-entry value of the packing. At a matric suction of 0.06 MPa and 22°C the stress path has already met the SD yield locus and a further temperature increase will tend to move upward this yield locus, regardless of the current state of yielding. This way, drained heating at constant intergranular stress generates a plastic volumetric swelling, with the thermal hardening induced by the increase in temperature being compensated for by the mechanical softening. In contrast, drained cooling at constant intergranular stress is assumed to be an elastic process during which the yield surface moves downward, but further experimental evidence is needed. This SD yield locus, taken parallel to the neutral line $p + \chi s = \text{const.}$, is defined as:

$$\begin{aligned} &\text{SD}: \; s_D(\varepsilon_v^p, \Delta T) - (p + \chi s) = 0 \\ &s_D(\varepsilon_v^p, \Delta T) = s_{DO}(\varepsilon_v^p) + B(\Delta T) \end{aligned} \tag{6.17}$$

The dependence on hardening parameter $s_D(\varepsilon_v^p, \Delta T)$ is modelled assuming an uncoupled thermal hardening and volumetric strain softening through a thermal hardening function $B(\Delta T) = b_1 \Delta T + b_2 \Delta T^2$, where b_1 and b_2 are coefficients of thermal sensitivity of the yield locus and ΔT stands for the temperature increase with respect to a reference state (alternatively, the term $b_2 \Delta T |\Delta T|$ is introduced to take into account equivalent features in cooling paths). $s_{DO}(\varepsilon_v^p)$ is the usual hardening parameter that depends on plastic volumetric strains according to $\delta s_{DO} = K_{p+s} \, \delta \varepsilon_v^p \big/ f_D(p / p_o)$ (Alonso *et al.*, 1998b), where K_{p+s} is defined according to Eq. (6.8). Gens (1993) suggested that the increment of irreversible plastic swelling of the macrostructure be given by coupling ratio fD (p/po) affecting reversible strains. Fig. 6.20 presents experimental data for two different temperatures, where this positive coupling ratio decreases with overconsolidation ratio (refer to Eq. (6.7)). Negative values have been suggested by Alonso *et al.* (1998b) to take into account macropore invasion by expanded microstructure, but further experimental evidence is needed for stress states apart from the LC yield locus to avoid its influence during main wetting processes. In addition, movements of the SD and SI yield loci are cross-coupled, as previously indicated for the influence of SD yield curve movement on air-entry yield locus. The induced movement of LC yield locus (unidirectional coupling) due to the activation of SD is also clear due to strain softening that experiences the macrostructure caused by the irreversible swelling. Nevertheless, the activation of curve LC and its influence on SD yield locus is not so evident until more experimental data becomes available.

The consistency condition for an temperature increment δT at constant stress state $\delta\hat{p} = 0$ at yielding, implies that:

$$\frac{\partial s_D}{\partial T}\delta T + \frac{\partial s_D}{\partial \varepsilon_v^p}\delta\varepsilon_v^p = 0\,; \quad \frac{\delta\varepsilon_v^p}{\delta T} = -\frac{\dfrac{\partial s_D}{\partial T}}{\dfrac{\partial s_D}{\partial \varepsilon_v^p}} \approx -\frac{\dfrac{\partial B(\Delta T)}{\partial T}}{\dfrac{\partial s_{DO}}{\partial \varepsilon_v^P}}\,; \tag{6.18}$$

where the approximation holds under the assumption of no thermal dependence of elastic compressibility parameter for changes in net mean stress ($\partial\kappa/\partial T = 0$; $\kappa \approx 0.019$), as well as no significant changes of $f_D(p/p_o) \approx 1$ with increasing temperatures under high overconsolidation ratios (refer to Fig. 6.20). The above expression transforms to:

$$\frac{\delta\varepsilon_v^p}{\delta T} \approx -\frac{\kappa\, f_D(p/p_o)\ (b_1 + 2b_2\Delta T)}{(1+e_o)\hat{p}} \approx -3.3\times10^{-4}\ {}^{o}C^{-1} + 6.0\times10^{-7}\ {}^{o}C^{-2}\ \Delta T \tag{6.19}$$

where linear interpolation has been adopted to fit $\delta\varepsilon_v^p/\delta T$ data under nearly constant intergranular stress $\hat{p} \approx 0.09$ MPa for $(u_a\text{-}u_w) = 0.06$ MPa, which is shown in Fig. 6.29. For soil conditions prevailing at the beginning of the heating path (e_o = 0.591, T_r = 22°C), coefficients of thermal sensitivity of the yield surface are: $b_1 \approx 2.5\times10^{-3}$ MPa.°C^{-1} and $b_2 \approx -2.3\times10^{-6}$ MPa.°C^{-2}, remaining the thermal hardening function always positive.

Fig. 6.30 shows volume change results of heating-cooling drained cycles compared to isothermal main wetting paths at constant net vertical stress and at different temperatures, while Fig. 6.31 presents equivalent results in terms of water content changes. Vertical overconsolidation ratio at the beginning of the heating path is between 30 and 38 with respect to the unsaturated preconsolidation stress at equivalent matric suction. In general, quite good agreement is observed in terms of swelling strain development and water content increase upon initial heating when compared to isothermal paths. Swelling strains in wetting paths of heavily overconsolidated and active clays, in addition to depending on initial water content and applied confining stress, also depend on temperature. However, it should also be emphasised that suction induced strains are usually much larger than thermal strains.

6.3 Suction Controlled Collapse (Swell) / Shrinkage under Constant Load Results on High-Porosity Packings (Isothermal Paths)

6.3.1 Main wetting and drying paths

In this section, collapse (swell) / shrinkage behaviour under the isothermal main wetting and drying paths indicated in Fig. 4.7 and carried out on the different oedometer cells described in section 3.2, are presented and discussed. Time evolution of typical oedometer test results (both volumetric strain and water content change) conducted on these high-porosity packings in main wetting paths at two different temperatures are presented in Fig. 4.15, Fig. 4.16, Fig. 4.17 and Fig. 4.18. At low stress levels, Fig. 4.15 indicates that suction induced swelling strains at 22°C are smaller than at 80°C, which is the general trend observed under heavily overconsolidated conditions. However, at higher net vertical stresses a collapsible phenomenon is detected, which appears to generate somewhat higher compressive strains at higher temperatures and matric suction values (refer to Fig. 4.17) and is reverted at lower suction values (refer to Fig. 4.18). Time evolution of volumetric strain, net lateral stress, water content and degree of saturation at 22°C for the different matric suction steps along the complete wetting-drying-wetting process obtained with the lateral stress oedometer cell are indicated

in Fig. 6.32 and Fig. 6.33, where a monotonic compressive evolution is observed for this meta-stable packing in the main wetting phase. Net lateral stress increases during the first wetting step up to a maximum $K_{0nc} \approx 0.45$, which is maintained approximately constant during the different main wetting stages. The general trend of increasing K_{0nc} as suction is reduced is consistent with test results on collapsible lateritic soils reported by Machado and Vilar (1997) and Vilar *et al.* (1998), tending to K_{0nc} values close to those obtained in saturated soil tests. However, a reduction is observed in the last wetting stage that is not consistent with the previous argument and further tests are required to study this effect under nearly saturated states. This increase of K_{0nc} with increasing degree of saturation is indicated in Fig. 2.14, where main wetting suction controlled results (the last part under nearly saturated conditions is not indicated) are plotted in conjunction with virgin compression results at constant water content (refer to Fig. 2.12 and Fig. 2.13) and virgin loading results at constant matric suction (refer to Fig. 6.50). A peak is detected during the different transient wetting steps, which could be associated to a spurious problem caused by the sensitivity of the lateral stress system to the pressure distribution along the ring wall as indicated in section 6.2.1.1. Relatively low values of K_0 are consistent with the compensation of the system, where the soil is first allowed to contract at a small magnitude and then brought back to a condition of zero lateral strain (more related to an active lateral pressure), which is the pressure being measured. In addition, K_0 values are in agreement with low K_0 values reported by Machado and Vilar (1997) and Vilar *et al.* (1998), when testing collapsible lateritic soils under suction controlled wetting. Shrinkage irreversible features when air-entry value is surpassed are detected in the main drying-scanning wetting paths represented in Fig. 6.33, where the net lateral pressure is again cancelled when a suction of 0.45 MPa is reached (similar to the behaviour observed when testing the high-density fabric and represented in Fig. 6.7). The results corresponding to the equalisation stages are indicated in Fig. 6.34, where main features of irreversible compression upon main wetting and irreversible shrinkage upon main drying (coupled to water content changes) are detected. As observed, net horizontal stress evolution presents a recoverable behaviour upon scanning wetting.

Fig. 6.35 shows the comparison of swelling strains, water content and degree of saturation changes for two different temperatures developed during wetting-drying-wetting paths under a constant net vertical stress of $(\sigma_v - u_a) = 0.600$ MPa, where suction induced compressive strains are somewhat higher at elevated temperatures. An equivalent plot is given in Fig. 6.36 under a constant net vertical stress of $(\sigma_v - u_a) = 1.20$ MPa, where an opposite trend with respect to thermal effects on suction induced compressive strains is detected. In addition, equalisation water content values are somewhat lower at higher temperatures for both cases. An overall comparison in terms of volume change behaviour is indicated in Fig. 6.37, where clear irreversible features upon main wetting and main drying are observed. At lower net vertical stresses and higher temperatures, higher suction induced swelling and shrinkage strains are observed. At intermediate net vertical stress values, higher suction induced compressive strains are detected at elevated temperatures. This trend is reversed at higher stress values and near the maximum collapse zone.

Swelling / collapse under load curves for two different temperatures starting from the initial state are shown in Fig. 6.38 and Fig. 6.39. The initial vertical overconsolidation ratio OCR_{vo} at 22°C varies between 15 and 1 for the different paths (refer to Fig. 4.7). Test results define a series of virgin compression lines that tend to converge in the maximum collapse zone. Also, Wheeler and Sivakumar (1995) presented data for compacted kaolin that showed increasing slopes at higher suction values. Josa *et al.* (1992) modified the model of Alonso *et al.* (1990) to reduce the wetting-induced collapse at high net mean stresses, displaying diverging normal compression lines (in agreement with the original model) up to a certain limit and then reversing the trend to converge in the maximum collapse zone, where normal consolidation lines at higher suction values are no longer straight lines in the conventional v : ln p plot. This condition arises from the fact that maximum collapse behaviour was considered in the shape of the loading-collapse yield curves and not on the form of the normal compression lines (Wheeler and Karube, 1996). Compressibility parameter values for changes in net vertical stress under saturated virgin states are around $\lambda_{oed}(0) \approx 0.136$ at 22°C and $\lambda_{oed}(0) \approx 0.150$ at

80°C, which show certain temperature dependence and are in agreement with post-yield compression results presented in Fig. 6.67. Swelling pressure values from swell / collapse under load results and at different suctions are also presented in Fig. 6.38. In general, decreasing values are detected for decreasing suctions, following a similar trend to that shown in Fig. 6.73, though with somewhat lower values compared to those reported with the constant volume method in correspondence with testing results reported by Justo *et al.* (1984), Sridharan *et al.* (1986) and Feng *et al.* (1998). No clear temperature effect is found on swell / collapse under load swelling pressure, though a somewhat higher value compared to that obtained under isochoric conditions is detected (refer to Fig. 6.75), possibly related to some influence of the testing procedure.

As observed in Fig. 6.39, the main influence of temperature is reflected in the first loading stage at constant water content contained at intra-aggregate scale, which results in a rearrangement of soil structure to a more densely packed position mainly related to a decrease in the shearing strength of aggregate contacts. The overall conceptual framework of volume change behaviour of the two packings normalised with respect to the initial overconsolidation ratio with values between 173 and 1, in loading at constant water content and main wetting stages, is indicated in Fig. 6.40. A similar plot for the permanent reduction in void ratio due to temperature cycling under constant effective stress for values of overconsolidation ratios between 8 and 1 is given in Demars and Charles (1982). One of the most outstanding aspects is the loading effect, where skeleton rearrangement as a result of heating is more important at lower overconsolidation ratios. The successive wetting stages reflect similar patterns of behaviour, displaying the heated samples higher swelling strains at higher overconsolidation ratios. Also, heated samples at normally consolidated states present higher compression strains in the early wetting stage, but this situation is reversed in the final phases. In summary, contracting or dilating thermal behaviour is strongly dependent on overconsolidation ratio and the recent stress history, where loading and main wetting paths followed at low overconsolidation degrees reflect temperature effects mainly in the previous loading stage while at higher overconsolidation values the thermal influence is induced in the wetting process. This way, it appears that temperature, loading and suction effects are not coupled at low overconsolidation ratios, while at higher overconsolidation ratios there is an important coupled phenomenon due to water sorption induced by temperature. Maximum collapse zone is detected in the second wetting stage, where at higher net vertical stresses the collapse is smaller due to the remarkable reduction of inter-aggregate spaces that the sample has experienced in the previous loading and wetting stages. The normally consolidated condition, which is indicated with an arrow in the different stages of the figure, is modified as irreversible rearrangement on skeleton develops. Positions to the right of the arrow indicate normally consolidated conditions.

Fig. 6.41 presents the results of measured water content and degree of saturation values (determined in a free water sense) under steady state conditions for the different matric suction steps followed during main wetting. Constant volume swelling pressure paths at different temperatures and presented in Fig. 6.75, as well as their different equalisation stages, are also plotted in the previous figure, where two clear swell and collapse under load zones are identified. An opposite trend to that presented for the high-density packing is detected, where lower equalisation water content values upon main wetting are associated with the hotter specimens, in agreement with volumetric strain results due to the lower storage capacity of water mass that offers the hotter soil that has undergone a higher compression. Also, somewhat higher equalisation degrees of saturation are detected on the heated samples, condition that is more remarkable at higher suctions. An overall picture for both packings is presented in Fig. 6.42 in terms of matric suction work conjugate variable changes (volumetric water content changes normalised with respect to the initial soil volume) for different suction steps upon main wetting as a function of the initial overconsolidation ratio varying between 173 and 1. This plot is not as appropriate as the equivalent one associated to volume changes, since the gap between both packings increases as the wetting stages advance. As observed, thermal induce water sorption is more important at high overconsolidation ratios, in a coupled behaviour to thermal induce swelling.

Temperature effects on volumetric water content changes do not offer a clear trend in normally consolidated states (points to the right of the arrow).

Water content and degree of saturation values under steady state conditions for the different matric suction steps during main drying are indicated in Fig. 6.43. Constant volume shrinkage pressure paths at different temperatures without surpassing the air-entry value of the packing are also represented. Degree of saturation values are reversed with respect to main wetting results, showing that the air-entry value of the packing is reached before at higher temperatures, where lower degrees of saturation are detected at higher suction values. After main wetting, the drying-wetting paths show again a remarkable plastic shrinkage behaviour, condition that is less outstanding at higher net vertical stresses. Apparent yield suction values, where important irreversible strains are detected for matric suctions higher than this air-entry value, are represented in Fig. 6.44 for both temperatures, different fabrics (high-porosity aggregated and 2-mm pellet fabrics) and at different net vertical stresses. In general, increasing values of desaturation pressures are detected at higher net vertical stresses, because of the higher compressive strains developed upon main wetting and at higher temperatures that affect in an irreversible way clay skeleton, inducing a more closed structure that presents a higher air-entry value. Within an elastoplastic point of view, this condition is associated to a macrostructural strain hardening induced by the activation of the loading-collapse LC yield surface upon main wetting, which affects via volumetric plastic strain the position of the suction increase SI yield locus (refer to Eq. (6.6)). This way, if different yield surfaces are admitted to describe the main wetting path (activation of LC in high-porosity packings or activation of SD in low-porosity fabrics inducing macrostructural softening), their consequences on plastic volumetric strains must be reflected on the SI hardening law, irrespective of their origin or admitting certain weighting functions. Shrinkage strains (suction change from 0.01 MPa to 0.45 MPa) for both temperatures, different fabrics (aggregated and 2-mm pellet fabrics) and different net vertical stresses are shown in Fig. 6.45. As observed, shrinkage strains are higher at elevated temperatures and at lower vertical stresses. In addition, the different fabrics appear to generate some effects on the development of shrinkage strains, where lower strains are detected in the pellet structure. Nevertheless, the differences observed between both structures can be partly associated to testing spurious problems, mainly due to ring friction effects, but this fact is not possible to be stated due to the lack of the height to radius ratio of the pellet fabric test.

After the main wetting and drying cycle the specimens present a quasi-elastic behaviour with some hysteretic loop. Reversible strains for a suction change between 0.45 MPa and 0.01 MPa are also presented in Fig. 6.45, where somewhat higher values are detected at elevated temperatures and tending to lower differences at elevated stress levels. In this case a quite good agreement is detected when comparing high-porosity aggregated and pellet fabrics.

6.3.2 Reversible features under nearly saturated conditions

Isothermal changes in elastic strain associated with changes in intergranular vertical stress $\delta\varepsilon_v^e/\delta[(\sigma_v - u_a) + (u_a - u_w)]$ under nearly saturated states are represented in Fig. 6.46 for constant (σ_v-u_a) and (u_a-u_w) data and for different intergranular vertical stresses. The same interpolations (type A according to Eq. (6.9) and type B according to Eq. (6.10)) and parameters to those presented for the high-density packings have been used, showing an adequate agreement with test results at different temperatures. In addition, both high-porosity structures at 22°C (aggregated and 2-mm pellet fabrics) present similar trends of behaviour. The overall picture for the different artificially prepared packings is indicated in Fig. 6.47, where temperature effects are more important at lower intergranular stresses.

Isothermal reversible changes in work conjugate extensive variable of matric suction with changes in intergranular vertical stress $[Gs/(1+e_o)]\delta\varepsilon_v^e/\delta[(\sigma_v - u_a) + (u_a - u_w)]$ under nearly saturated states are represented in Fig. 6.48 for constant (σ_v-u_a) and (u_a-u_w) data and for different intergranular vertical

stresses. The same interpolations and parameters indicated in Eq. (6.11) are used. The overall picture of both packings is represented in Fig. 6.49, where higher values are obtained at higher temperatures and mainly at low net vertical stresses.

6.4 Loading-Unloading Paths under Controlled Suction

6.4.1 Results on low-porosity packings

Isothermal net stress increase and decrease under different constant matric suctions and after a main wetting and drying path were carried out at different temperatures following the test calibrations and procedures detailed in section 3.2.4.1 and section 4.2.1.1, respectively. Time evolutions of typical oedometer test results (both volumetric strain and water content changes) in loading paths at controlled matric suction and at two different temperatures are presented in Fig. 4.28. These plots indicate that loading induced volume changes at 22°C are somewhat lower than at 80°C. The variations of specific volume v, state variable Gs.w (associated to the work conjugate variable of matric suction), coefficient of earth pressure at rest K_0 and degree of saturation with net vertical stress or net mean stress at a constant suction of 0.20 MPa is shown in Fig. 6.50. Specific volume, state variable Gs.w and degree of saturation show clear pre and post-yield zones. Since the transition towards yielded states is usually a gradual process, care has been taken in following a systematic procedure in order to identify the yield stress based on strain energy concepts (Tavenas *et al.*, 1979). Only volumetric incremental work input per unit volume has been considered (refer to Eq. (6.5)):

$$\left.\frac{\delta W}{\delta p}\right|_{s=const.} = \frac{\kappa}{1+e_o} \quad \text{or} \quad \left.\frac{\delta W}{\delta(\sigma_v - u_a)}\right|_{s=const.} = \frac{\kappa_{oed}}{1+e_o} \quad (\text{pre}-\text{yield range})$$
$$\left.\frac{\delta W}{\delta p}\right|_{s=const.} = \frac{\lambda(s)}{1+e_o} \quad \text{or} \quad \left.\frac{\delta W}{\delta(\sigma_v - u_a)}\right|_{s=const.} = \frac{\lambda_{oed}(s)}{1+e_o} \quad (\text{post}-\text{yield range}) \tag{6.20}$$

where κ (under isotropic conditions, v : ln p plane) or κ_{oed} (under oedometer conditions, v : ln (σ_v-u_a) plane) represent the compressibility parameters in the pre-yield range, and $\lambda(s)$ $(=-\delta v/\delta \ln p)$ or $\lambda_{oed}(s)$ $(=-\delta v/\delta \ln(\sigma_v - u_a))$ the equivalent compressibility parameters in the post-yield range. The yield stress state is identified by the intersection of linear extrapolations of the pre and post-yield zones. However, in the pre-yield region the compressibility parameter steadily increases with stress level until attaining a nearly constant value in the post-yield range. This way, a different plot is considered, representing the cumulated volumetric work input per unit volume against the logarithmic of the net stress level, where a nearly linear behaviour is obtained in the pre-yield zone, whereas the post-yield behaviour appears to deviate from linearity only at high stress levels. This method, which can be seen as an equivalent representation to that adopted by Butterfield (1979) for the compression law, has been used and analysed by Senol (1996) in saturated oedometer tests comparing yield values with known preconsolidation pressures. An equivalent framework is followed for describing state variable Gs.w change with increasing net mean stress, where only the incremental work input per unit volume associated to water content changes has been considered (refer to Eq. (6.5):

$$\left.\frac{\delta W}{\delta \ln p}\right|_{s=const.} = \frac{s\,\kappa_w}{1+e_o} \quad (\text{pre}-\text{yield range})$$
$$\left.\frac{\delta W}{\delta \ln p}\right|_{s=const.} = \frac{s\,\lambda_w}{1+e_o} \quad (\text{post}-\text{yield range}) \tag{6.21}$$

where $\kappa_w = -Gs\,\delta w/\delta \ln p$ represents the equivalent parameter in terms of water content change in the pre-yield range, whereas $\lambda_w = -Gs\,\delta w/\delta \ln p$ corresponds to the post-yield zone. As observed in Fig. 6.50, compression results in Gs.w – ln p plane show clear pre and post-yield zones. The limit between these two domains is in agreement with compression yield stress determined from volumetric considerations. Typical compressibility parameters for the different diagrams are also indicated in the previous figure, where values in terms of net vertical stresses are somewhat lower than the corresponding ones in terms of net mean stresses ($\kappa_{oed} \approx 0.006$ and $\lambda_{oed}(s) \approx 0.043$ compared to $\kappa \approx 0.011$ and $\lambda(s) \approx 0.051$, where the same symbols as under isotropic conditions are used). The value of the parameter associated to water content changes in the post-yield zone is slightly lower ($\lambda_w(s) \approx 0.040 < \lambda(s)$), presenting the same value under pre-yield conditions ($\kappa_w \approx 0.011$). These last aspects, which are also detected in Fig. 6.59 and Fig. 7.20, are in accordance to model predictions as proposed by Wheeler (1996), who included specific water volume changes within an elastoplastic framework. According to this model, the elastic variation of the specific volume under a loading path at constant suction is identical to the corresponding variation of the specific water volume ($v_w = 1+Gs.w$), i.e. $\kappa \approx \kappa_w$, being this fact a consequence of admitting no significant elastic changes of macropore volume (macrovoid variations are associated to plastic processes). Also, Zakaria (1995) observed no appreciable changes in both specific volumes when isotropically unloading compacted kaolin at a relatively low and constant suction value. According to Wheeler (1996), the slope of the normal compression line for v_w under certain assumptions for the loading-collapse yield curve is given by:

$$\lambda_w(s) = \lambda(s) - \frac{\alpha(s)(\lambda(s) - \kappa)}{\lambda(0) - \kappa} \tag{6.22}$$

where the parameter $\alpha(s)$ tends to zero at zero suction and to $\lambda(0)$-κ at a suction s_c, corresponding to the air overpressure required to desaturate macropores while maintaining micropores completely saturated. This value approximately corresponds to the delimiting point in the retention curve of $s_c \approx 1.9$ MPa, separating 'inter-aggregate governing suction' and 'intra-aggregate governing suction' zones, as defined in section 5.1.1. For a value of $\lambda(0) \approx 0.060$ (refer to Fig. 6.57), the parameter is around $\alpha(0.20\text{MPa}) \approx 0.013 < \lambda(0)$-$\kappa$, which presents an adequate value within the previous range. Further values of this parameter are indicated in section 6.4.2 and in section 7.1.1.4.

As shown in Fig. 6.50, the lateral stress coefficient K_0 decreases upon loading tending to a nearly constant value in the post-yield zone of approximately $K_{0nc} \approx 0.43$, in agreement with results presented in Fig. 2.14. During the following unloading path, the value increases up to the initial condition, tending to drop in the subsequent reloading stage and following a reversible behaviour. Values of K_0 at nearly saturated conditions and at $OCR_v \approx 2.4$ are also represented in Fig. 2.14, where an adequate agreement is obtained compared to values at the same overconsolidated ratio using compression test results at constant water content. The evolution of the degree of saturation exhibits an increasing trend in the post-yield zone, while it is nearly constant in the pre-yield stages. This fact is associated to the higher efficiency of loading effects in deforming soil skeleton than expelling water, in opposed way to what happens during suction consolidation, where it is more efficient to remove water by desaturating a pore than to deform soil skeleton (the degree of saturation diminishes, refer to Fig. 5.31).

Loading and unloading results at different temperatures and different suctions are plotted in Fig. 6.51 (u_a-u_w = 0.45 MPa), Fig. 6.52 (u_a-u_w = 0.30 MPa) and Fig. 6.53 (u_a-u_w = 0.01 MPa). Yield stresses and compressibility parameter evolutions with applied stresses are also indicated. No clear trend is detected for the different yield stresses, where similar results are observed at both temperatures. This yield stress is highly dependent on the previous main wetting path, which induces a macrostructural softening due to the activation of the suction increase yield locus, and to the main drying path that induces a further strain hardening due to the activation of the suction increase yielding (refer to Fig.

6.12). Yield points in relation to the loading-collapse LC yield locus of the original high-density packing are presented in Fig. 6.58, where a dominating strain softening induced on main wetting is detected (yield points to the left of the original packing). A striking aspect is that systematically higher values of the compressibility parameter in the post-yield range are detected at higher temperatures (for an overall picture at different suctions refer to Fig. 6.57). Possibly, certain temperature induced effects are associated to the previous main wetting and drying stages, where an overall strain softening is detected and inducing a higher skeleton compressibility (the data shown in Fig. 6.57 and Fig. 6.67 confirm that $\lambda_{oed}(s)$ increases at higher void ratios). This trend is not in agreement with existing data, where usually no temperature dependence of the virgin compressibility parameter is reported (Campanella and Mitchell, 1968; Eriksson, 1989; Tidfors and Sällfors, 1989; Lingnau *et al.*, 1995; Lingnau *et al.*, 1996; Belanteur *et al.*, 1997; Robinet *et al.*, 1997). However, Plum and Esrig (1969) and Akagi and Komiya (1995) detected some small thermal dependence on compressibility indexes (higher values at elevated temperatures). Sultan *et al.* (1998) presented data on saturated Boom clay, where certain convergence trend of the virgin compression lines is observed at high stress levels and where curves associated to higher temperatures show somewhat higher compressibility values. On the other hand, the convergence of the curves at higher stresses was also mentioned by Tanaka *et al.* (1995,1997) testing reconstituted illitic clay, but in this case showing higher compressibility values at lower temperatures. As observed in Fig. 6.51 to Fig. 6.54, the pre-yield compressibility parameter shows somewhat higher values at higher temperatures (for an overall picture at different suctions refer to Fig. 6.57).

Fig. 6.54 shows v : ln (σ_v-u_a) plots of the different loading - unloading paths followed by the different high-density packings at different temperatures and under nearly saturated conditions. Previous compression under constant water content and main wetting and drying paths are also indicated. Higher compressibility parameters in the post-yield range are obtained at lower suctions for both temperatures, where virgin compression lines tend to converge at high net stress levels. Higher compressibility values for the virgin line at lower suctions are in agreement with previous results reported by Josa (1988), Vicol (1990), Cui (1993), Sivakumar (1993) (for suctions higher than 100 kPa), Maâtouk *et al.* (1995), Cui and Delage (1996), Laloui *et al*. (1997) and Cui *et al.* (1998b) (for suctions between 12.6 MPa and 113 MPa). In addition, somewhat lower elastic compressibility indexes are detected at higher suctions for both temperatures, also in agreement with results reported by Vicol (1990) at ambient temperature. Pre and post-yield compressibility parameters at different matric suctions and temperatures are presented in Fig. 6.57. Fig. 6.55 shows v : ln [(σ_v-u_a)+(u_a-u_w)] plots of the different loading paths under nearly saturated states, where the constant suction paths tend to a unique relationship in virgin states (virgin compression line, also represented in Fig. 6.54) in terms of specific volume and the equivalent effective stress. At yielding and under $\chi \to 1$ conditions, volume change behaviour considering intergranular stress or net stress can be described by:

$$\delta e = -\lambda^*(0)\left.\frac{\delta(p+\chi s)}{p+\chi s}\right|_{s=const.} = -\lambda^*(0)\left.\frac{\delta p}{p+\chi s}\right|_{s=const.} \quad ; \quad \delta e = -\lambda(s)\frac{\delta p}{p}$$
$$\lambda(s) = \frac{p}{p+\chi s}\lambda^*(0) \tag{6.23}$$

where the last expression is obtained eliminating void ratio differences and solving for $\lambda(s)$. $\lambda^*(0)$ is the equivalent compressibility parameter in the post-yield range, in terms of intergranular stresses and under nearly saturated conditions. Typical values are around $\lambda^*_{oed}(0) \approx 0.081$ at 22°C and $\lambda^*_{oed}(0) \approx 0.110$ at 80°C, where a higher compressibility is detected at higher temperatures (refer to Fig. 6.57). The last expression, valid for nearly saturated states under constant suction where the approximation to an effective stress can be made, recovers $\lambda^*(0)$ under zero suction conditions and indicates that $\lambda(s) < \lambda^*(0)$ for s > 0. However, $\lambda(s)$ in addition of depending on matric suction varies

with net mean stress, which hinders its use in conventional diagrams. Relationships analogous to Eq. (6.23), where matric suction acts as a stress component without an explicit incorporation as an independent stress state variable have been used by Karube (1988) and Rohlf *et al.* (1997) for characterising compressibility and strength properties. The approach followed in the previous plot is only intended to demonstrate the extension of effective stress under nearly saturated states and to derive some relationships related to nearly saturated states, where the unique relationship can be seen as a state boundary line separating attainable from unattainable states under nearly saturated conditions at suctions lower than the air-entry value of the packing (refer to Fig. 6.57). However, this state boundary can be transgressed at higher suction values under the preponderance of meniscus water.

Equivalent suction induced loading - unloading v : ln $[(\sigma_v-u_a)+(u_a-u_w)]$ plots have been represented in Fig. 6.56 for both temperatures (main drying and scanning wetting paths), where under nearly saturated and normally consolidated states the curves try to follow a unique theoretical virgin drying line as defined by Toll (1995) that is equivalent to the virgin compression line (represented in dashed lines). However, this aspect is not clearly detected in this figure due to the slightly overconsolidated state of the packings that reach this line with small induced strains and transgress it when passing to the preponderance of meniscus water conditions. Nevertheless, this aspect is observed when plotting the same diagrams under normally consolidated states corresponding to the high-porosity fabrics represented in Fig. 6.66. Maximum compressibility is detected when the quasi-saturated packing approaches and remains in this virgin drying line with dominating oblique intergranular forces to the tangent planes of aggregate contacts, and after passing the air-entry value further changes in suction do not lead to significant changes in soil volume (the suction induced loading is less efficient than the mechanical loading due to dominating normal intergranular forces to the tangent planes of aggregate contacts). Coupled aspects related to water content changes in main drying paths are more detailed in section 5.1.7.2.

Loading-collapse LC yield curves at different temperatures, presented in Fig. 6.58, have been fitted to a modified form of Alonso *et al.* (1990) to take into account aggregate deformability and strength at high suction values. As observed in Fig. 2.15, somewhat higher fabrication stresses at a specified dry density are required as total suction is increased in the 'intra-aggregate governing suction' zone, where water is mainly contained at intra-aggregate scale (total suction values higher than 2 MPa). This condition is equivalent to the higher compactive effort required to compact at lower water contents in the dry-side and at a specified dry density (refer to Fig. 2.11). As intra-aggregate water content increases, the aggregates with lower suction values decrease in strength and are prone to suffer more deformation during compaction. The general expression is proposed as:

$$\frac{p_o}{p^c}=\left(\frac{p_o^*}{p^c}\right)^{(\lambda(0)-\kappa)/(\lambda(s)-\kappa)} \quad ; \quad \lambda(s)=\lambda(0)\left[r+(1-r)\exp(-\beta s)-\gamma\ln\left(\frac{s}{s_{min}}\right)\right] \tag{6.24}$$

where p_o^* stands for the saturated preconsolidation stress, p^c is a reference stress, r is a constant related to the maximum stiffness of soil in the 'inter-aggregate governing suction' zone, β is a parameter that controls the rate of soil stiffness with suction in the same 'inter-aggregate governing suction' zone, γ a parameter that induces further stiffness in the 'intra-aggregate governing suction' zone, and s_{min} a reference suction value. This way, the trend of the original equation is corrected to take into account a further stiffness effect at high suctions, and the original expression is maintained at low suction values. For $(\sigma_v-u_a)_o^*=0.7\,\text{MPa}$, $(\sigma_v-u_a)^c$ = 0.1 MPa and $s_{min}=0.01$ MPa, the following parameters are obtained at 22°C using a non-linear curve-fitting algorithm (least-squares method with some restrictions on the compressibility coefficients, according to Fig. 6.57): $\lambda_{oed}(0) \approx 0.062$, $\kappa \approx 0.010$, $r \approx 0.645$, $\beta \approx 1.336\,\text{MPa}^{-1}$ and $\gamma \approx 0.015$. For equivalent saturated net vertical overconsolidation stress and reference stresses, the following parameters are obtained at 80°C:):

$\lambda_{oed}(0) \approx 0.090$, $\kappa \approx 0.010$, $r \approx 0.625$, $\beta \approx 1.361$ MPa^{-1} and $\gamma \approx 0.015$, where main difference in terms of temperature effects are reflected in post-yield compressibility parameter. In Fig. 6.57, the same post-yield compressibility expression (Eq. (6.24)) is represented, where an adequate agreement is observed, although the values correspond to nearly saturated conditions in contrast to LC curve fitting results that represent main wetting conditions. Pre-yield compressibility parameters at different suctions and temperatures are also indicated in Fig. 6.57, where a small dependence on suction is observed (refer to the fitted expressions in the same figure). Further aspects of loading-collapse yield locus in terms of net mean stresses are presented in Fig. 7.22.

6.4.2 Results on high-porosity packings

Typical time evolutions of volumetric strains and water content changes in different step loading paths at controlled matric suction and 22°C are indicated in Fig. 4.30. Time evolutions of volumetric strain, water content change, water and air pressure changes and net lateral stress for a loading step at controlled matric suction and 22°C obtained with the lateral stress oedometer cell are indicated in Fig. 4.31. Isochrones and time evolutions at selected nodes of the same numerically simulated loading process are indicated in Fig. 4.32 and Fig. 4.31. Evolutions of specific volume v, state variable Gs.w, coefficient of earth pressure at rest K_0 and degree of saturation with net vertical stress or net mean stress at a constant suction of 0.20 MPa are shown in Fig. 6.59, where clear pre and post-yield zones are detected on specific volume, state variable Gs.w, degree of saturation and on coefficient K_0. Compressibility parameters for the different diagrams are also indicated in the previous figure ($\kappa_{oed} \approx 0.010$ and $\lambda_{oed}(s) \approx 0.110$ in terms of net vertical stresses, and $\kappa \approx 0.013$ and $\lambda(s) \approx 0.093$ in terms on net mean stresses). The results confirm that post-yield parameters increase with increasing void ratio. The value of the parameter associated to water content changes in the post-yield zone is slightly lower ($\lambda_w(s) \approx 0.062 < \lambda(s)$), presenting the same value under pre-yield conditions ($\kappa_w \approx 0.013$), and confirming the same aspects detected in Fig. 6.50. In addition, the parameter associated to water content changes in the post-yield zone increases with increasing porosity. Parameter $\alpha(s)$ as defined by Wheeler (1996) registers a value of $0.043 < \lambda(0)\text{-}\kappa$, assuming $\lambda(0) \approx 0.125$ (refer to Fig. 6.67), which shows a higher value compared to the high-density fabric possibly related to some dependence on porosity.

As shown in Fig. 6.59, the lateral stress coefficient in the normally consolidated range K_{0nc} slightly increases upon loading in accordance to degree of saturation rise and with the general trend presented in Fig. 2.14. The value slightly increases in the unloading path due to overconsolidation effects, tending to decrease in the subsequent reloading stage and following a quasi-reversible behaviour. The evolution of the degree of saturation exhibits an increasing trend in the post-yield zone, while it is nearly constant in the pre-yield stages. The limit between the pre and post-yield domains determined from incremental work input per unit volume associated to water content changes is in agreement with the equivalent one associated to volumetric strains.

Loading and unloading results at different temperatures and different suctions are plotted in Fig. 6.60 ($u_a\text{-}u_w = 0.45$ MPa), Fig. 6.61 ($u_a\text{-}u_w = 0.20$ MPa), Fig. 6.62 ($u_a\text{-}u_w = 0.06$ MPa) and Fig. 6.63 ($u_a\text{-}u_w = 0.01$ MPa). Yield stresses and compressibility parameter evolutions with applied stresses are also indicated. No clear trend is detected for the different yield stresses, where similar results are observed at both temperatures. These yield stresses are highly dependent on the previous loading, main wetting and drying paths, which induce upon main drying a macrostructural softening due to the activation of the suction increase yield locus at low stress levels or a macrostructural hardening due to the activation of the loading-collapse yield locus at medium and high stress levels (refer to Fig. 6.37). Upon main drying, the activation of the suction increase yield locus induces further macrostructural strain hardening. Yield points for both temperatures in relation to the loading-collapse LC yield locus of the original high-porosity packing are presented in Fig. 6.58, where a dominating strain hardening induced on loading, main wetting and drying is detected (yield points to the right of the original packing). Systematically, somewhat higher values of the compressibility parameter in the post-yield

range are detected at higher temperatures, which is more obvious at lower suctions (refer to Fig. 6.67). Pre-yield compressibility parameters show somewhat higher values at higher temperatures (refer to Fig. 6.67).

Fig. 6.64 shows v : ln (σ_v-u_a) plots of the different loading-unloading paths followed by the different high-porosity packings at different temperatures, where previous compression under constant water content and main wetting and drying paths are also indicated. Somewhat higher compressibility parameters in the post-yield range are obtained at lower suctions for both temperatures, which are also dependent on the previous loading, main wetting and drying paths. An exception is presented in Fig. 6.63 corresponding to s = 0.01 MPa, due to the important strain hardening effect induced by the previous loading and collapse stage (this compressibility is represented in Fig. 6.57 corresponding to the high-density fabric). Pre and post-yield compressibility parameter values at different matric suctions and temperatures are presented in Fig. 6.67. Fig. 6.65 shows v : ln [(σ_v-u_a)+(u_a-u_w)] plots of the different loading paths under nearly saturated states, where the constant suction paths tend to a unique relationship under normally consolidated states (virgin compression line, also represented in Fig. 6.64) in terms of specific volume and the equivalent effective stress. Typical values of the equivalent compressibility parameter in the post-yield range in terms of intergranular stresses and under nearly saturated conditions are around $\lambda^*_{oed}(0) \approx 0.126$ at 22°C and $\lambda^*_{oed}(0) \approx 0.166$ at 80°C (refer to Fig. 6.67). As observed, this unique relationship valid only for nearly saturated states is transgressed by the loading path performed at s = 0.45 MPa, which evolves under degree of saturation values corresponding to the preponderance of meniscus water (the air-entry value of the packing is surpassed as indicated in Fig. 6.67). Equivalent suction induced loading-unloading v : ln [(σ_v-u_a)+(u_a-u_w)] plots have been represented in Fig. 6.66 for both temperatures (main drying and scanning wetting paths), where under nearly saturated and normally consolidated states the curves try to follow a unique theoretical virgin drying line that is equivalent to the virgin compression line represented in dashed line. This line also separates nearly saturated states from others under the preponderance of meniscus water, where further changes in suction do not induce important changes in soil skeleton (dominating normal intergranular stresses in aggregate contacts as proposed by Fleureau *et al*., 1993).

Loading-collapse LC yield curves for the original packing at different temperatures are presented in Fig. 6.68 and Fig. 6.69. Data have been non-linearly fitted according to Eq. (6.24) with certain restrictions on post-yield compressibility parameters, where for 22°C, $(\sigma_v - u_a)^*_o = 0.124$ MPa , (σ_v-u_a)^c = 0.050 MPa and $s_{min} = 0.010$ MPa, the following parameters are obtained: $\lambda_{oed}(0) \approx 0.126$, $\kappa \approx 0.010$, $r \approx 0.353$, $\beta \approx 2.991$ MPa^{-1} and $\gamma \approx 4.1\times10^{-3}$. The net vertical preconsolidation stress for saturated conditions is estimated from isochoric swelling pressure paths indicated in the previous figures and discussed in section 6.5. The reference stress (σ_v-u_a)^c is approximately estimated as the intersection of the virgin compression line corresponding to the saturated state with the normal compression line under constant water content (s ≈ 1.9 MPa) that are indicated in Fig. 6.38, assuming a small elastic compressibility under suction changes. For a saturated net vertical overconsolidation stress of $(\sigma_v - u_a)^*_o = 0.095$ MPa (refer to Fig. 6.75) and equal reference stresses, the following parameters are obtained at 80°C: $\lambda_{oed}(0) \approx 0.166$, $\kappa \approx 0.010$, $r \approx 0.264$, $\beta \approx 3.321$ MPa^{-1} and $\gamma \approx 3.0\times10^{-3}$, where main differences in terms of temperature effects are reflected in the post-yield compressibility parameter. In addition, differences related to the dependence on porosity are mainly reflected on post-yield compressibility parameter, parameter r (decreasing with increasing porosity), parameter β (increasing with increasing porosity) and parameter γ (decreasing with increasing porosity). Post-yield compressibility parameters under nearly saturated conditions have been fitted to Eq. (6.24) and are presented in Fig. 6.67, where some differences with LC curve fitting results concerning parameter r are detected: $r \approx 0.650$ at 22°C and $r \approx 0.550$ at 80°C. Pre-yield compressibility parameters at different suctions and temperatures are also indicated in Fig. 6.67, where a small dependence on suction is observed (refer to the fitted expressions in the same figure) with no appreciable porosity dependence (refer to the equivalent expressions in Fig. 6.57). Apparent yield points upon main wetting related to the transition between the expansion phenomenon and the

meta-stable collapse are indicated in Fig. 6.69, where an adequate agreement is detected when comparing to the LC yield curve obtained from fabrication stresses and swelling pressure considerations. Yield points at low suction values detected at the left of the LC of the original packing are associated to macrostructural strain softening effects induced upon main wetting. Saturated net stresses at yielding obtained from different procedures and at different temperatures are indicated in Fig. 6.70. The different procedures include extrapolated values from static compaction tests at high suction values and different temperatures reported in section 2.3.1, conventional saturated compression tests performed on 2-mm pellet packings at 22°C and suction controlled isochoric swelling pressure tests at different temperatures. The main effect of decreasing saturated preconsolidation stress with increasing porosity is readily observed. In addition, the effect of decreasing saturated preconsolidation pressures with increasing temperature is detected on the extrapolated values from static compaction tests as a consequence of the decrease in fabrication stresses at a given water content observed at higher temperatures (refer to Fig. 2.16). However, temperature effects on saturated preconsolidation pressures is not so clearly detected in the isochoric swelling pressure paths, where this effect appears to be more evident in high-porosity packings. The general trend of decreasing saturated preconsolidation stress with increasing temperatures has been clearly observed for sulphide clays by Eriksson (1989), for marine and lacustrine clays by Tidfors and Sällfors (1989), for natural saturated clays by Moritz (1995), for remoulded saturated clays by Akagi and Komiya (1995) and for saturated Boom clay by Sultan *et al.* (1998).

6.5 Suction Controlled Constant Volume Swelling and Shrinkage Pressure Tests

Suction controlled swelling and shrinkage pressure tests have been conducted on both packings, since swelling pressure is essentially controlled by the initial dry density, under isochoric conditions using the testing setup and oedometer cells described in section 3.2.2.3 and section 3.2.3.2, and the procedure outlined in section 4.2.1.1. As further detailed, different patterns of comportment are encountered during first suction reduction: a dominating swelling for the low-porosity packing, where a higher swelling pressure is detected, and a controlling macrostructural collapse compensated by the reversible expansion of the structure for the high-porosity fabric. In this last case, swelling stress reaches a maximum controlled by the macrostructural yield surface and then decreases upon subsequent wetting following this yield locus at constant volume. There are a number of laboratory techniques for swelling pressure measurements under triaxial and oedometer conditions, and test methods on this area are described in Justo *et al.* (1984), Sridharan *et al.* (1986), Habib and Karube (1993) and Feng *et al.* (1998).

Continuous records of net vertical stress, net horizontal stress, water content changes and loading system deformation were obtained throughout the experiments. Time evolutions for the different main wetting and drying stages are represented in Fig. 6.71 for both packings, starting from overconsolidation ratios in a mean stress sense of around 16 for the high-density fabric and around 30 for the high-porosity packing. The equalisation stages in wetting paths continued for 7 days, whereas the drying stages were maintained for 3 days, until some steady state in water content is registered. Nevertheless, some secondary stress relaxation effects are present and try to overlap themselves with the primary collapse and shrinkage phenomena. As observed, the highest swelling pressure increment is developed in the first wetting stages, tending to a nearly constant value in the case of the high-density packing and progressively decreasing in the case of the high-porosity fabric. The following drying phase without surpassing the air-entry value of the packing is developed with a monotonous decreasing trend of swelling pressure, which is cancelled at a suction of less than 0.45 MPa in the case of the high-porosity packing. The loading system deformation, which presents a compressibility of around 20 μm/kN upon loading, displays some irreversible features upon unloading. Effects of loading system deformability on swelling pressure are more important for the stiffer high-density sample, and certainly a somewhat lower swelling pressure is expected to develop if some swelling is allowed (around 0.30%). However, it is also expected that these effects are not excessively important, condition that is verified when comparing the slightly higher isochoric swelling pressure values with

equivalent suction controlled swell/collapse under load results presented in Fig. 6.13, where system compressibility has been corrected in the previous loading path under constant water content. Effects of apparatus deformability on different swelling pressure methods have been analysed by El-Sohby *et al.* (1989).

Time evolution of water content has been converted to time evolution of mean matric suction using the constant volume retention curve plots represented in Fig. 5.7 and under the assumption that local equilibrium between liquid and vapour phases is reached despite the transient wetting stage. Vertical and horizontal swelling and shrinkage pressure paths represented in log s : (σ_v-u_a) or (σ_h-u_a) stress plane for different high-density packings are indicated in Fig. 6.72. Maximum net vertical swelling pressure is detected at the end of the wetting path, though the horizontal one increased up to a maximum value of around s = 0.45 MPa that is maintained constant until the end of the imbibition path purportedly related to some yielding condition, where initial stress state anisotropy is progressively erased upon wetting. Nearly isotropic stress state evolutions upon subsequent drying are readily observed, which are reversible in terms of the net vertical stress and displays some irreversible trend in the net horizontal stress that can be associated to some incipient yielding upon wetting. Normally consolidated state is achieved under nearly saturated conditions due to the progressive softening of the sample during imbibition. Isochoric wetting paths in relation to the original loading-collapse yield curve of the high-density packing are presented in Fig. 6.58 (net horizontal and vertical stress paths) and in Fig. 7.22 (net mean stress path). A constant volume swelling pressure path carried out at ambient temperature under controlled relative humidity in the high suction range (intra-aggregate water content zone) and starting from approximately the same void ratio (SCK.CEN test results reported in Volckaert *et al.*, 1996a) have also been indicated in Fig. 6.58, where soil macrostructure reacts rigidly against suction changes (soil stiffness modulus against loading is higher than the corresponding one for suction changes). In addition, no important dependence on initial suction is detected for conditions starting from the preponderance of meniscus and intra-aggregate water in agreement with experimental results reported by Sridharan *et al.* (1986) and the arguments outlined in Gens and Alonso (1992). Isochoric swelling pressure values in relation to swell under load results and loading after free swell results were discussed in section 6.2.1.1.

Vertical and horizontal swelling and shrinkage pressure paths represented in the same stress plane for different high-porosity packings are indicated in Fig. 6.73. As observed, both vertical and horizontal swelling stresses reach a maximum at around s = 0.45 MPa because of yielding at constant volume and then decrease upon subsequent wetting. In addition, the anisotropic loading condition imposed during one-dimensional compression is progressively erased upon wetting, and the following drying path presents a nearly isotropic stress state evolution. The overconsolidation ratio is progressively lowered upon wetting due to the gradual softening of the sample, reaching normally consolidated states on arriving to the maximum swelling pressure zone. Lower swelling pressures are obtained in this packing as expected for the high sensitivity of swelling pressure on initial void ratio. Similar wetting stages have been imposed to an artificially prepared packing formed of 2-mm high-density pellets (dry density of around 2 Mg/m^3) compacted to an overall dry unit weight of 13.7 kN/m^3 and starting from hygroscopic humidity at an estimated total suction of around 100 MPa, performed in the context of a blind prediction test for the CATSIUS CLAY project (1998). Both high-porosity results starting from different initial suctions are presented in Fig. 6.74, where similar trends of behaviour, as well as equivalent swelling pressures upon arriving to nearly saturated conditions have been observed. In addition, both packings follow the same stress state evolution in the drying path, where shrinkage pressures are cancelled at a value of around s ≈ 0.4 MPa. Isochoric wetting paths in relation to the original loading-collapse yield locus are presented in Fig. 6.68 in terms of net vertical stresses and in Fig. 7.22 in terms of net mean stresses. As observed, swelling pressure is quite insensitive to the starting suction, as indicated by Gens and Alonso (1992) when describing the convergence of swelling pressure paths after reaching the loading-collapse yield curve. Constant volume stress paths are compared with suction controlled swell / collapse under load results in section 6.3.1. Fig. 6.75 presents the net vertical swelling pressure evolution for the high-porosity packing at different

temperatures, where a somewhat lower value under saturated conditions is detected at a higher temperature.

A striking aspect is detected in Fig. 6.66 when representing the shrinkage pressure path of the high-porosity packing in terms of the vertical intergranular stress, where the theoretical nearly saturated boundary is transgressed upon drying without surpassing the air-entry value of the packing. This situation is clearer described in terms of a conventional s : p stress plane, where the shrinkage pressure path does not reach the suction increase SI yield locus because of the decaying net stress upon increasing suction induced by the null volume change condition (refer to Eq. (6.28)). This situation is different to that originated when the drying path approaches the SI yield locus with a certain net stress level, which is the case of the different oedometer test results under constant net vertical stresses or the isochoric drying path of the high-density packing (refer to Fig. 6.56).

Swelling pressure paths for both packings represented in different state variable planes (s, p and $q = (\sigma_v - \sigma_h)$) are plotted in Fig. 6.76. Fig. 6.78 presents an equivalent plot for both high-porosity fabrics (aggregated and 2-mm pellet fabrics). When suction is reduced δs and any yield surface is crossed by this main wetting stress path, the stable soil structure experiences a swelling tendency and a net pressure increment δp is developed to maintain a constant volume condition. If the mechanism of volume change were only controlled by reversible soil macrostructural behaviour mainly caused by changes in inter-aggregation forces, the stress path would proceed along $\delta\varepsilon_v^e = 0$ according to:

$$\delta\varepsilon_v^e = \frac{\delta p}{K_p} + \frac{\delta s}{K_s}; \quad \delta p = -\frac{\kappa_s}{\kappa}\frac{p}{(s + p_{atm})}\delta s \tag{6.25}$$

where the macrostructural volumetric elastic strain $\delta\varepsilon_v^e$ is expressed as a function of mean stress and matric suction changes according to Eq. (6.8) under the preponderance of meniscus water. Bulk moduli due to net stress and suction changes are also indicated in Eq. (6.8). Values of κ_s/κ are around 0.49±0.27 for the stable high-density packing and a somewhat higher value for the first stable path of the high-porosity fabric of 0.76±0.30, according to processed values obtained from the previous figure. It is expected that microstructural mechanisms associated to aggregate expansion upon wetting are not of consideration since at these water content levels ($w \geq 15\%$) soil intra-aggregate microstructure is already water-saturated and further drainage is only imbibing macroporosity (refer to section 5.1.1). Indeed, the absorbed water volume normalised by soil total volume during this wetting path of $\Delta V_w/V = \Delta w\, \gamma_d/\gamma_w$ (around 24.4% for the high-porosity packing and around 14.8% for the high-density fabric), approximately coincides with the macroporosity indicated in section 5.1.1: around $0.67 n_o \approx 32.2\%$ for the high-porosity fabric with initial porosity $n_o \approx 48.2\%$ and around $0.43 n_o \approx 15.9\%$ for the high-density fabric with initial porosity $n_o \approx 37.1\%$.

If the saturation path brings the stress state to a macrostructural LC yield locus, which is the case of the high-porosity packing, the swelling pressure may reach a peak at some intermediate state during the wetting process. The collapse tendency experienced by the meta-stable structure is compensated by a decrease in net mean stress in order to maintain null volume change condition during plastification and the wetting path will follow the yield locus at constant volume, reaching a swelling pressure that will not differ much from the yield stress under saturated conditions (Gens and Alonso, 1992). However, some volumetric strain hardening is expected to occur under null volume conditions due to some reduction in macrostructural pore space at expense of the macrostructural reversible rearrangement ($\delta\varepsilon_v^p = -\delta\varepsilon_v^e$). According to experimental results for the high-porosity fabric ($1+e_o \approx 1.932$) presented in Fig. 6.76, and assuming a pre-yield compressibility of $\kappa \approx 0.019$ under net mean stress changes and $\kappa_s \approx 0.010$ under suction changes and a post-yield compressibility of $\lambda(0) \approx 0.110$, the following stress ratios, volumetric plastic strains and saturated preconsolidation stress changes are obtained and expected for the different wetting stages:

$$\frac{\delta s}{\delta p} \approx 9.20\,; \quad \delta\varepsilon_v^p \approx 0.33\%\,; \quad \frac{\delta p_o^*}{p_o^*} = \frac{1+e_o}{\lambda(0)-\kappa}\delta\varepsilon_v^p \approx 0.07 \quad \text{for} \quad s = 0.40\text{MPa} \rightarrow 0.20\text{MPa}$$
$$\frac{\delta s}{\delta p} \approx 3.23\,; \quad \delta\varepsilon_v^p \approx 0.52\%\,; \quad \frac{\delta p_o^*}{p_o^*} \approx 0.11 \quad \text{for} \quad s = 0.20\text{MPa} \rightarrow 0.06\text{MPa} \tag{6.26}$$
$$\frac{\delta s}{\delta p} \approx 0.75\,; \quad \delta\varepsilon_v^p \approx 0.61\%\,; \quad \frac{\delta p_o^*}{p_o^*} \approx 0.13 \quad \text{for} \quad s = 0.06\text{MPa} \rightarrow 0.01\text{MPa}$$

where the hardening law is according to the proposal of Alonso *et al.* (1990). Approximate aspects of stress ratio evolution as a consequence of yielding at constant volume can be analysed following the consistency condition and admitting low deviatoric stress changes that is the case presented in Fig. 6.76, as well as no appreciable strain hardening (a constant value of $p_o^* \approx 0.12$ MPa). This way, the stress path follows the loading collapse yield locus as defined by Eq. (6.24) with $p^c = 0.050$ MPa and $\gamma = 0$, according to:

$$\frac{\delta s}{\delta p} \approx -\frac{\partial f/\partial p}{\dfrac{\partial f}{\partial p_o}\dfrac{\partial p_o}{\partial s}} \approx \frac{\partial s}{\partial p_o}\,; \quad \frac{\partial s}{\partial p_o} = -\frac{(\lambda(s)-\kappa)^2}{p_o\,(\lambda(0)-\kappa)\ln(p_o^*/p^c)\,d\lambda(s)/ds}$$
$$\text{with} \quad \frac{d\lambda(s)}{ds} = -\beta\lambda(0)(1-r)e^{-\beta s} \tag{6.27}$$

where in the first expression no significant suction dependence is assumed for the apparent cohesion $\partial p_s/\partial s = 0$, being p_s the intercept with the p axis of the elliptical yield surface $f(p,q,s,p_o^*) = 0$ as proposed by Alonso *et al.* (1990). Average stress ratio values for the overall suction step indicated in Eq. (6.26) and according to data presented in Fig. 6.67 ($r \approx 0.65$ and $\beta \approx 2.991$ MPa^{-1}) is around $\delta s/\delta p \approx 5.3$, which adequately corresponds to the previous values.

Under a further suction increase path the specimens present a quasi-elastic behaviour if the suction increase yield locus is not surpassed. This way, soil structure will remain under a nearly saturated condition and soil compressibility against stress and suction changes will tend towards similar values. In addition, the stress state evolutions are quasi-isotropic, remaining their paths in the p axis (refer to Fig. 6.76 and Fig. 6.78). The equation for reversible volumetric behaviour under $\delta\varepsilon_v^e = 0$ conditions becomes (refer to Eq. (6.8) for further aspects of the bulk modulus K_{p+s} due to intergranular stress changes):

$$\delta\varepsilon_v^e = \frac{\delta(p+\chi(Se)s)}{K_{p+s}}\,; \quad \delta p = -\chi(Se)\delta s \tag{6.28}$$

It is important to clarify that these reversible features are mainly associated to macrostructural aspects, since suction changes at these low levels are mainly affecting inter-aggregate scale with dominating free water. Weighting factor $\chi(Se)$, expressed in terms of the effective bulk water saturation ratio as defined by Eq. (6.1), takes into account this preponderance of free water in macropores, with typical values of around: 0.50±0.26 for the high-density fabric, 0.47±0.23 for the high-porosity aggregated packing and 0.60±0.28 for the high-porosity 2-mm pellet fabric, as determined from values indicated in Fig. 6.76 and Fig. 6.78.

Typical log s : $\hat{p}$ and q : $\hat{p}$ swelling and shrinkage pressure paths are presented in Fig. 6.77 for both packings in terms of intergranular stresses using $\chi = Sr$ (dashed lines) and the effective free water

saturation ratio with a reference cut-off water content of w_{ref} = 15% (χ = Se in solid lines). Stress paths using parameter χ = Sr display a monotonic decrease of intergranular stress during imbibition process for both packings and displaying a clear reversible trend upon drying and within the nearly saturated zone in the case of the high-density fabric. The paths with parameter χ = Se start from nearly the initial net mean stress that presents a clearer physical meaning, evolving progressively towards higher intergranular stresses, due to the contribution of increasing degrees of saturation and net mean stresses. Finally, the stress paths are reverted due to the decrease in matric suction with no significant degree of saturation change and to the decrease in net mean stress of the high-porosity fabric, tending towards the net mean stress values under nearly saturated conditions, with a stress ratio of around $\delta s/\delta \hat{p} \approx 1.23 \pm 0.23$ in the case of the high-density packing and around $\delta s/\delta \hat{p} \approx 0.49 \pm 0.10$ for the high-porosity fabric. The following shrinkage path of the high-density packing shows a remarkable elastic behaviour within the nearly saturated zone, with a stress ratio of around $\delta s/\delta \hat{p} \approx 1.72 \pm 0.41$. The drying path of the high-porosity fabric presents a somewhat higher stress ratio of $\delta s/\delta \hat{p} \approx 2.33 \pm 0.38$, highlighting the irreversibility of the shrinkage path.

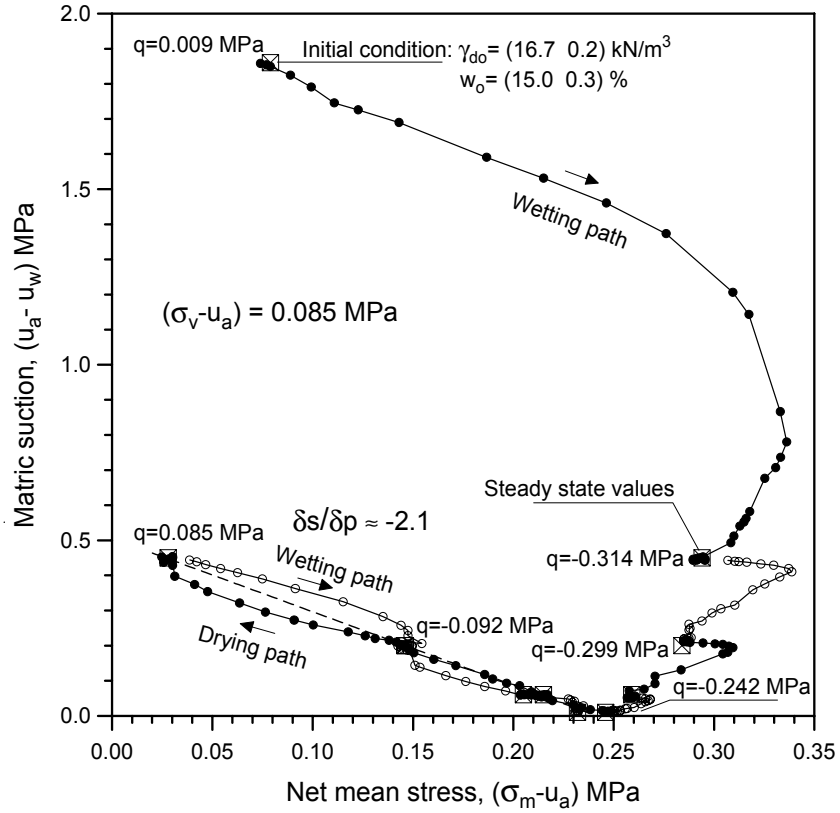

Figure 6.1 Stress paths in s : p plane for the high-density packing in a wetting-drying-wetting cycle under oedometer conditions and constant net vertical stress (T=22°C).

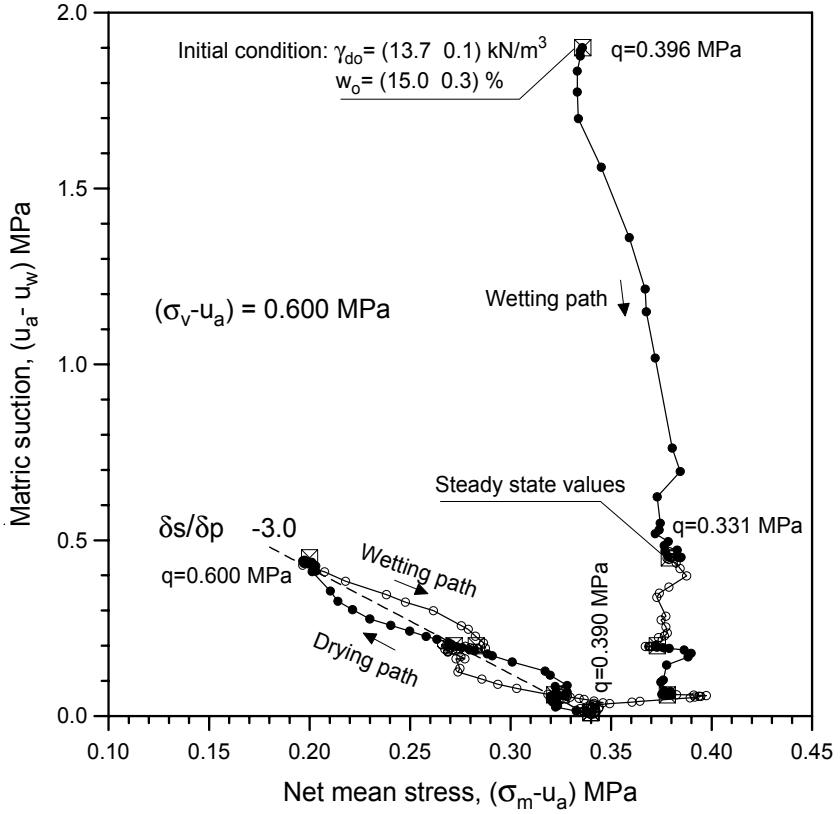

Figure 6.2 Stress paths in s : p plane for the high-porosity packing in a wetting-drying-wetting cycle under oedometer conditions and constant net vertical stress (T=22°C).

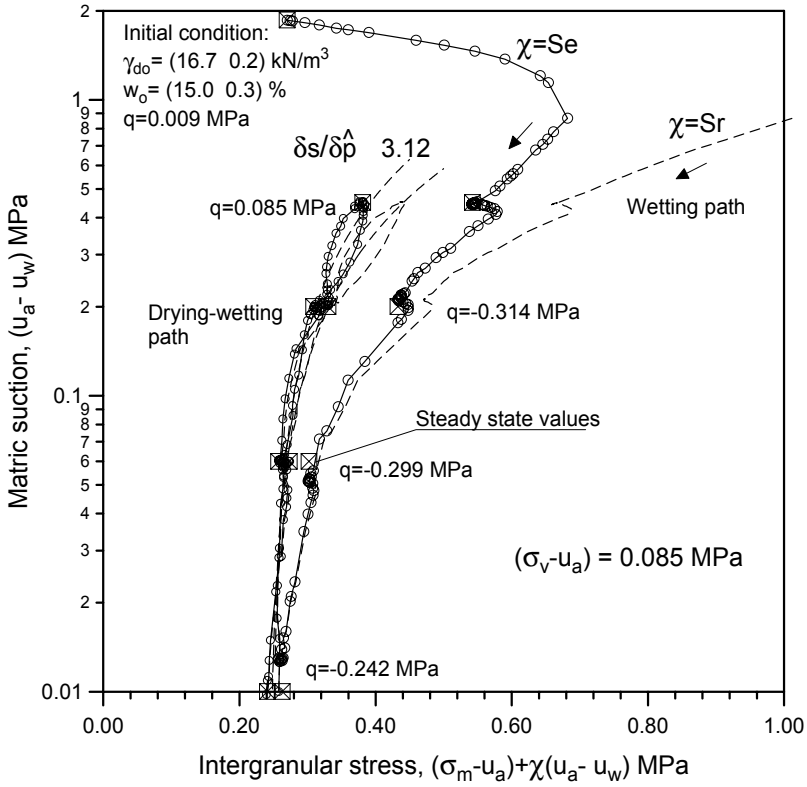

Figure 6.3 Stress paths in $\log s : \hat{p}$ plane for the high-density packing in a wetting-drying-wetting cycle under oedometer conditions and constant net vertical stress (T=22°C).

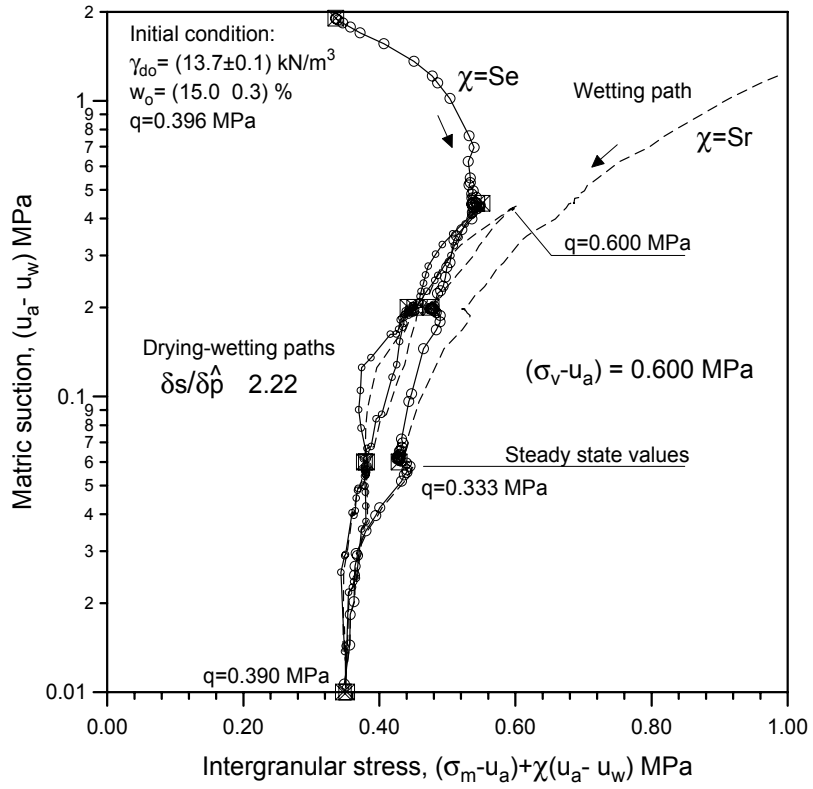

Figure 6.4 Stress paths in $\log s : \hat{p}$ plane for the high-porosity packing in a wetting-drying-wetting cycle under oedometer conditions and constant net vertical stress (T=22°C).

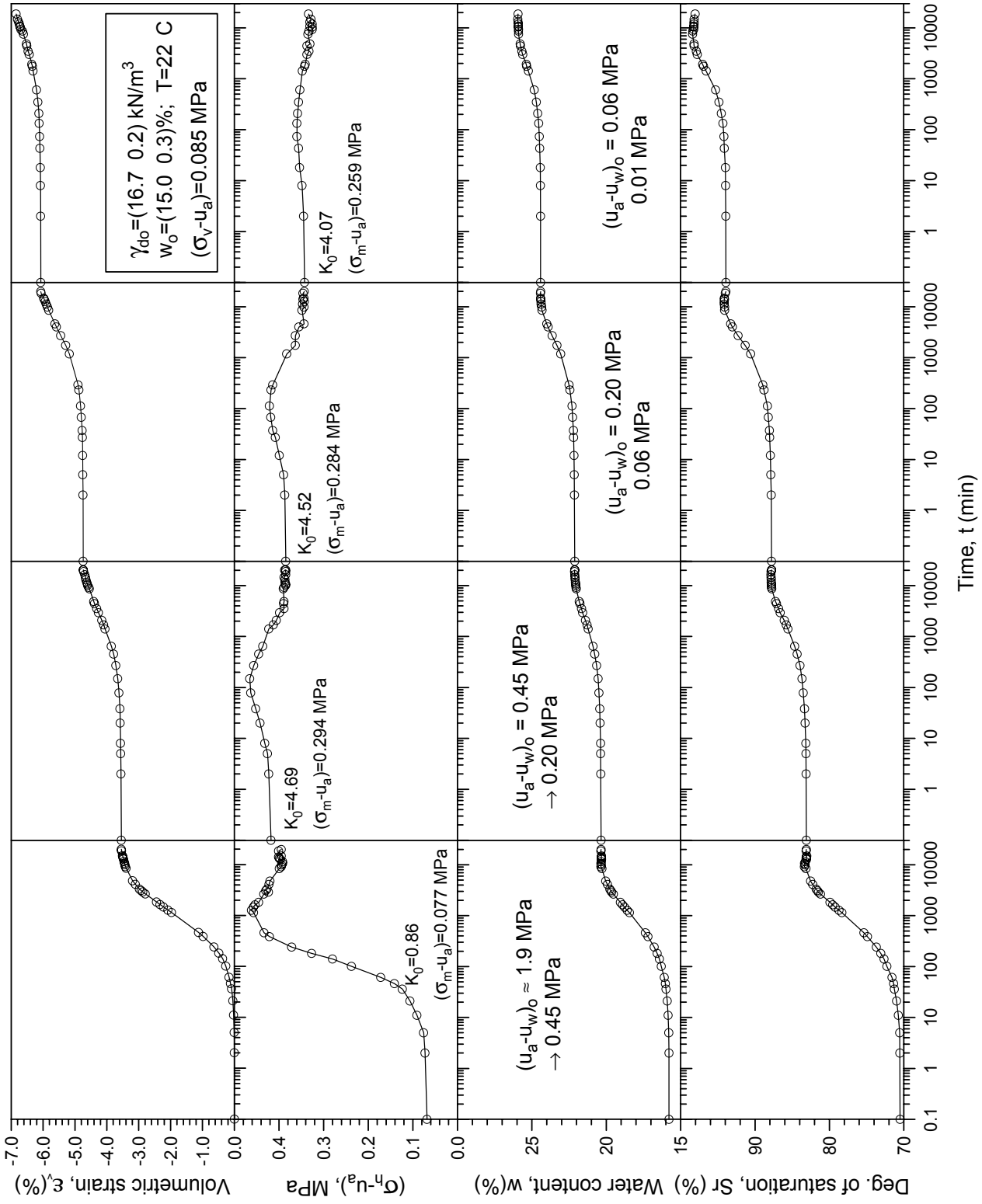

Figure 6.5 Time evolution of volumetric strain, net lateral stress, water content and degree of saturation at 22°C for the high-density packing in a main wetting process.

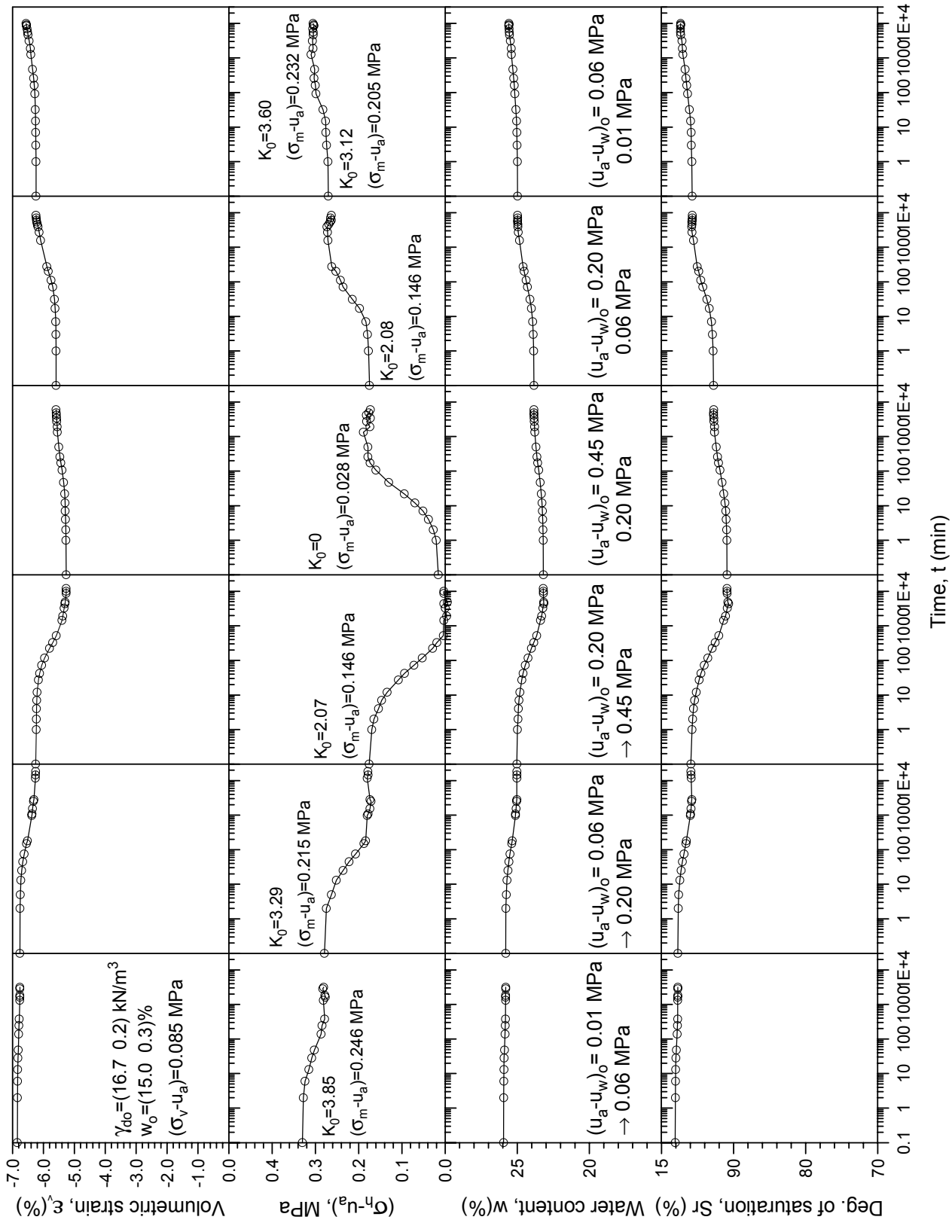

Figure 6.6 Time evolution of volumetric strain, net lateral stress, water content and degree of saturation at 22°C for the high-density packing in a main drying and wetting cycle.

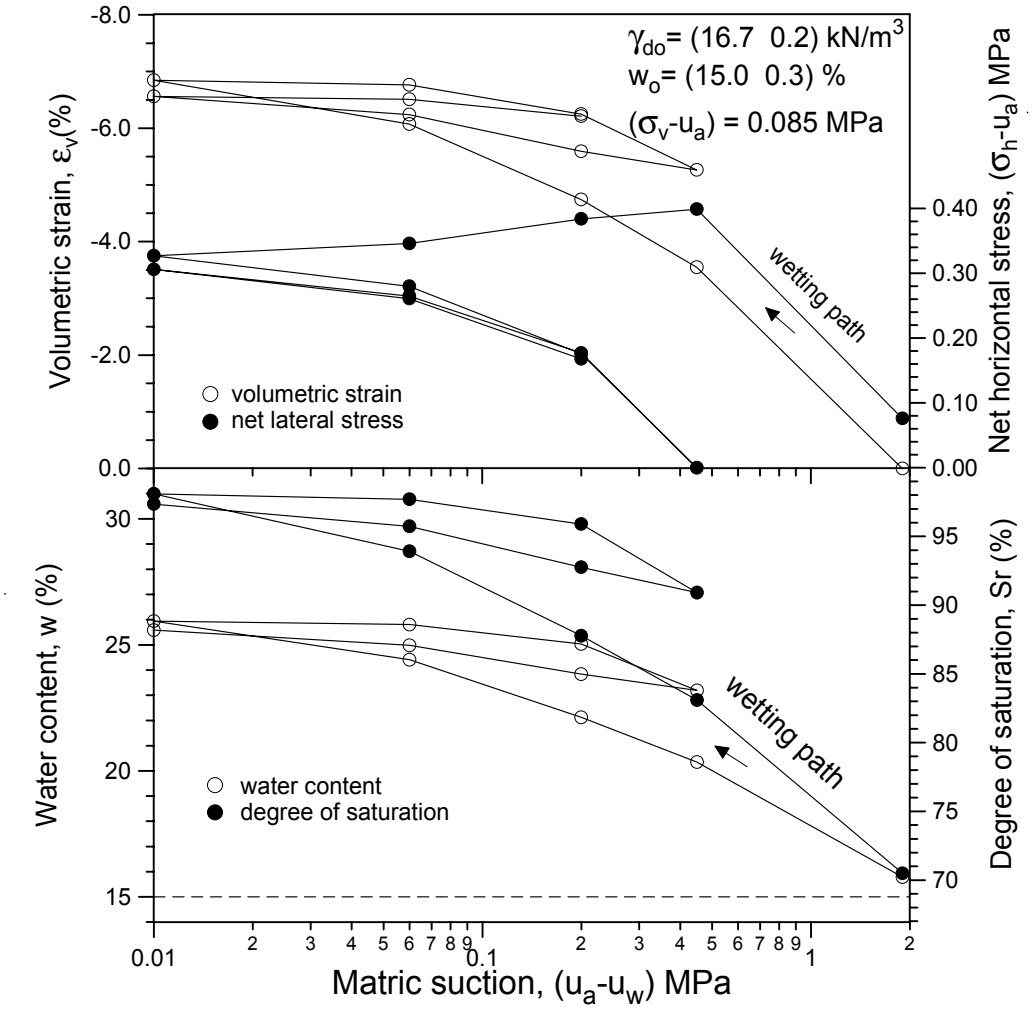

Figure 6.7 Variation of volumetric strain, net horizontal stress, water content and degree of saturation for the high-density fabric in wetting-drying cycles under constant net vertical stress (T=22°C).

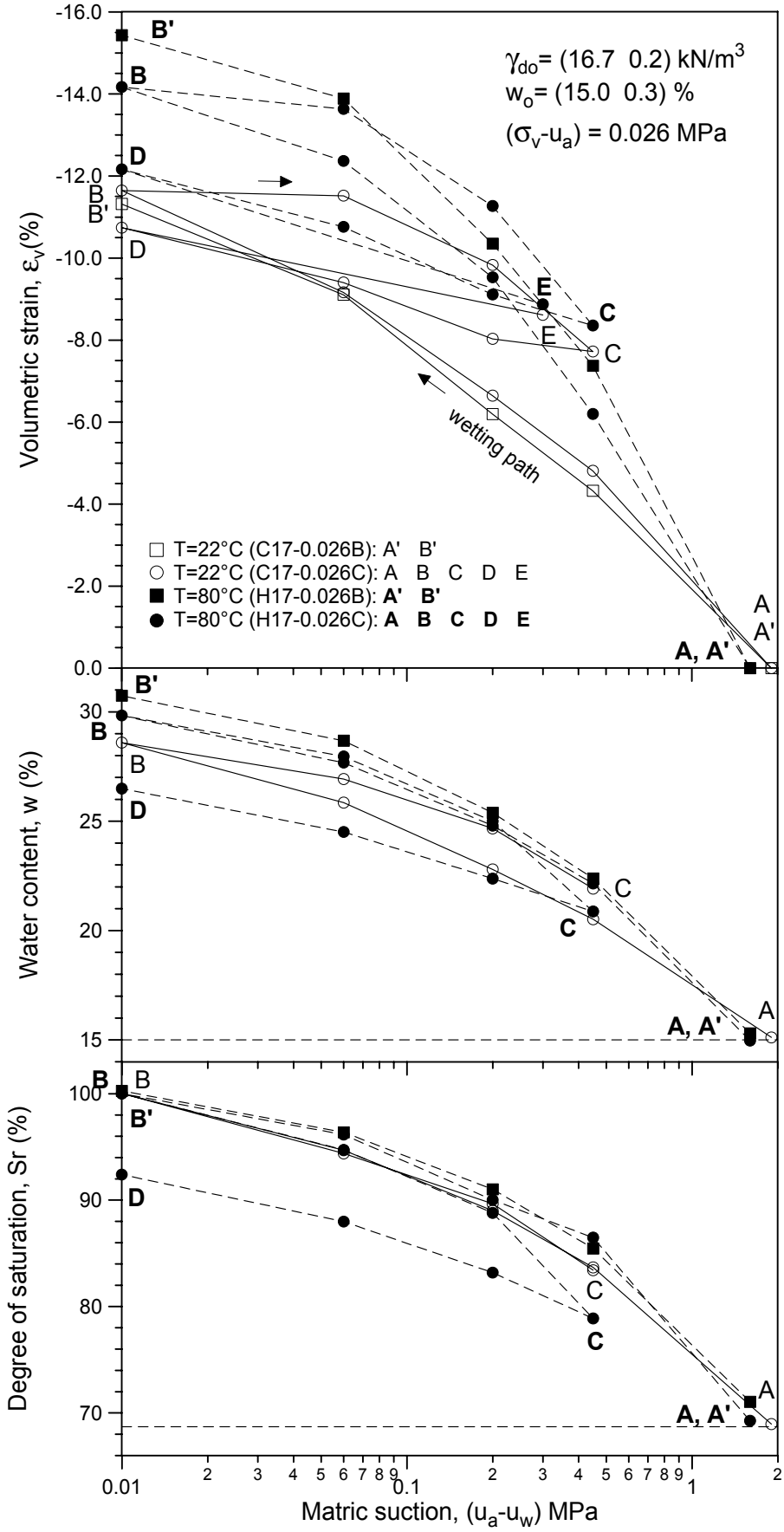

Figure 6.8 Variation of volumetric strain, water content and degree of saturation for the high-density fabric in wetting-drying cycles at two different temperatures and under constant (σ_v-u_a) = 0.026 MPa.

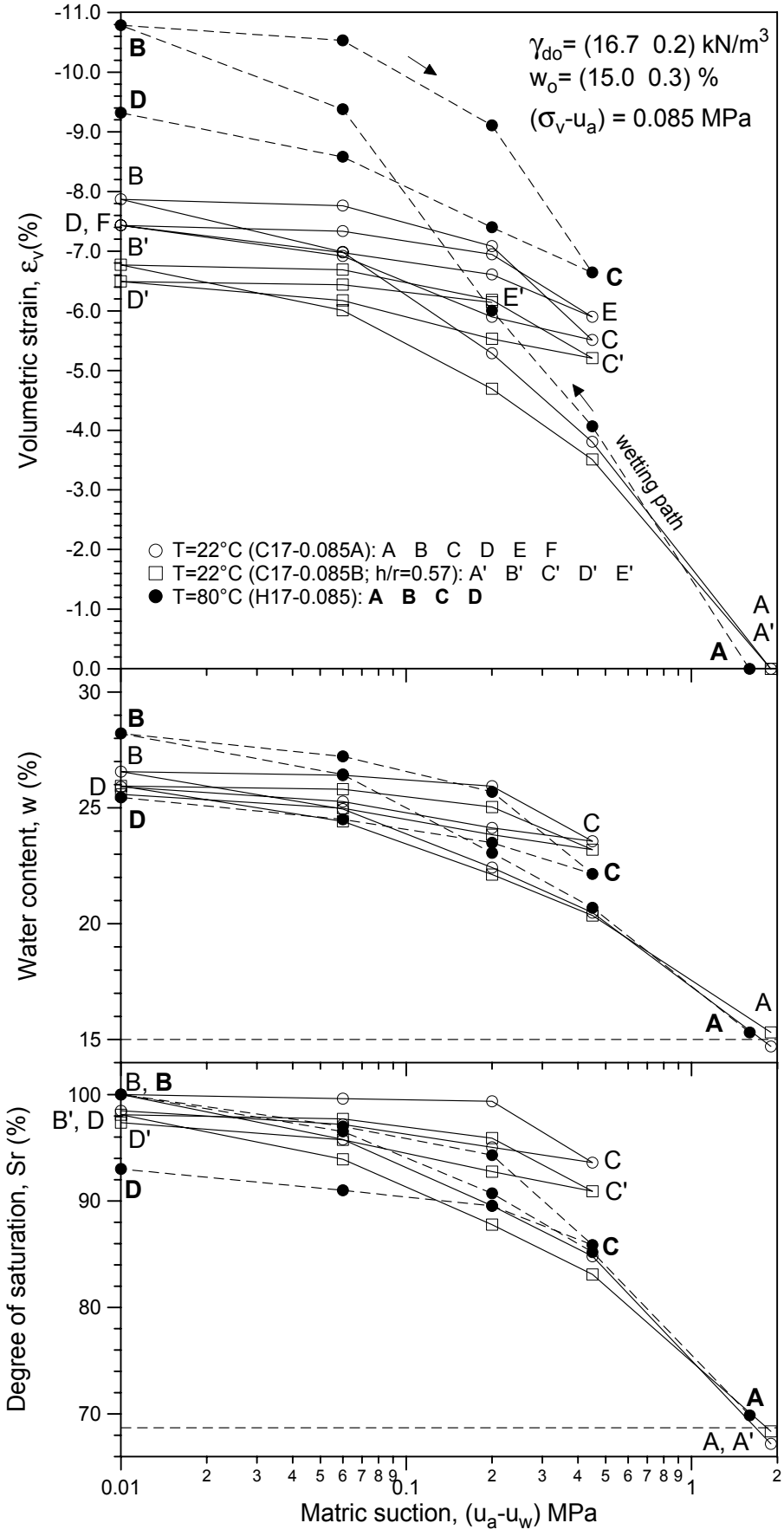

Figure 6.9 Variation of volumetric strain, water content and degree of saturation for the high-density fabric in wetting-drying cycles at two different temperatures and under constant (σ_v-u_a) = 0.085 MPa.

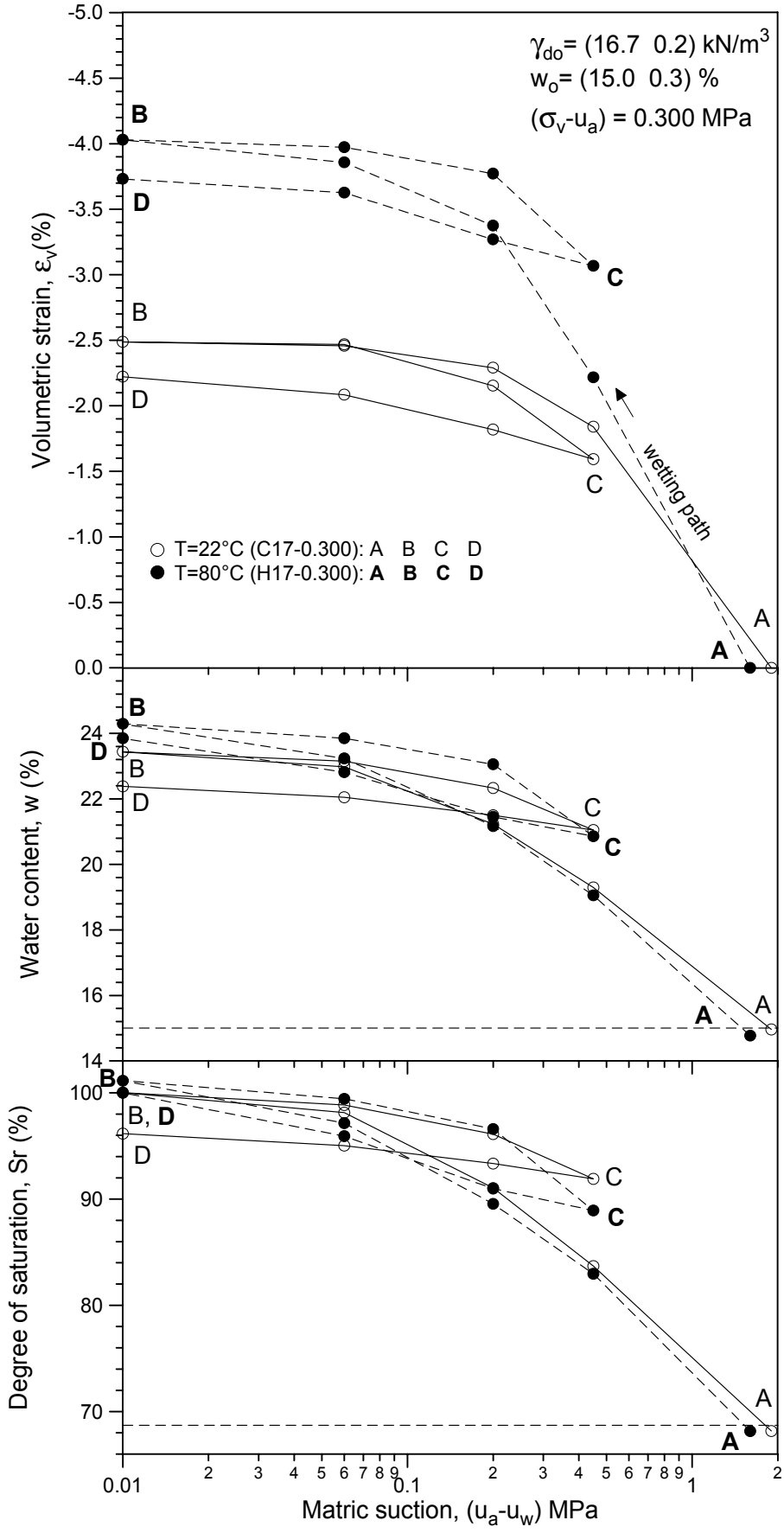

Figure 6.10 Variation of volumetric strain, water content and degree of saturation for the high-density fabric in wetting-drying cycles at two different temperatures and under constant (σ_v-u_a) = 0.300 MPa.

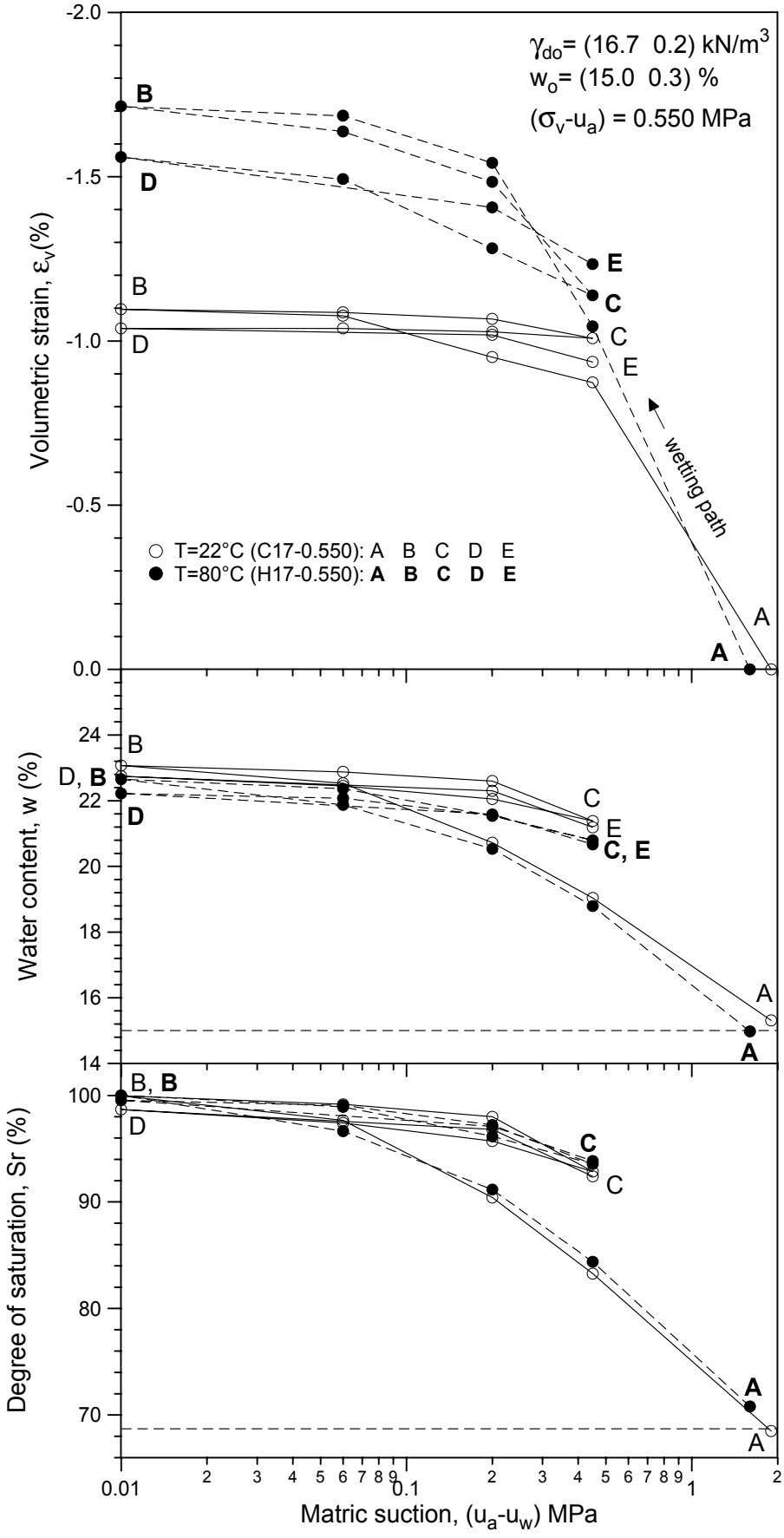

Figure 6.11 Variation of volumetric strain, water content and degree of saturation for the high-density fabric in wetting-drying cycles at two different temperatures and under constant (σ_v-u_a) = 0.550 MPa.

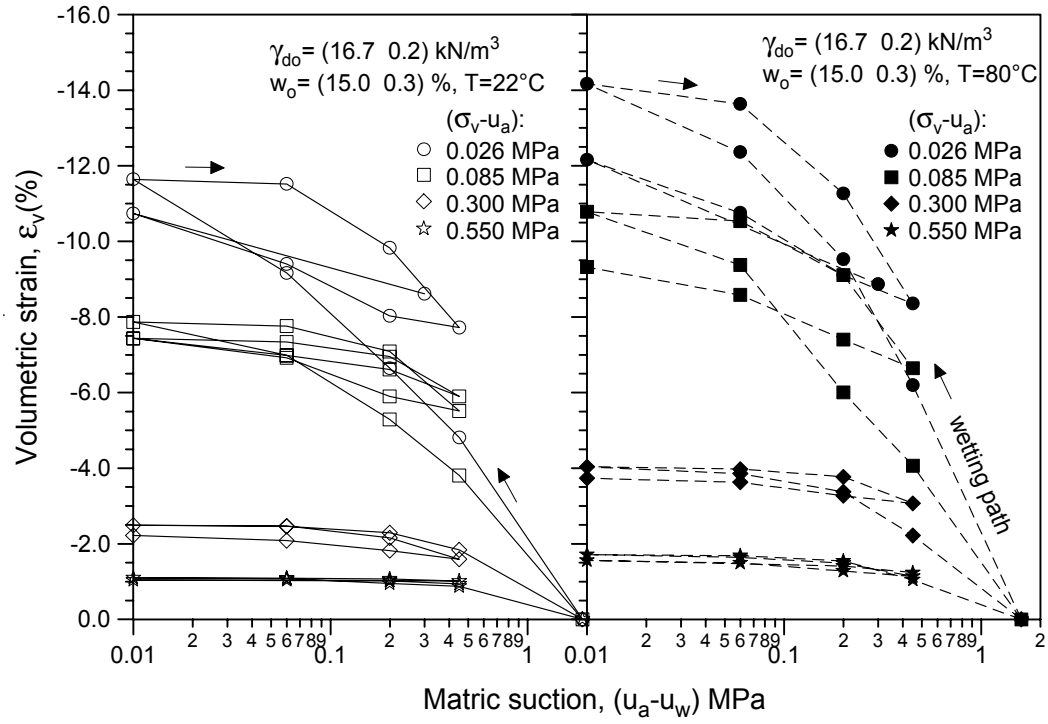

Figure 6.12 Comparison of volumetric strains for the high-density fabric in wetting-drying cycles at different net vertical stresses and temperatures.

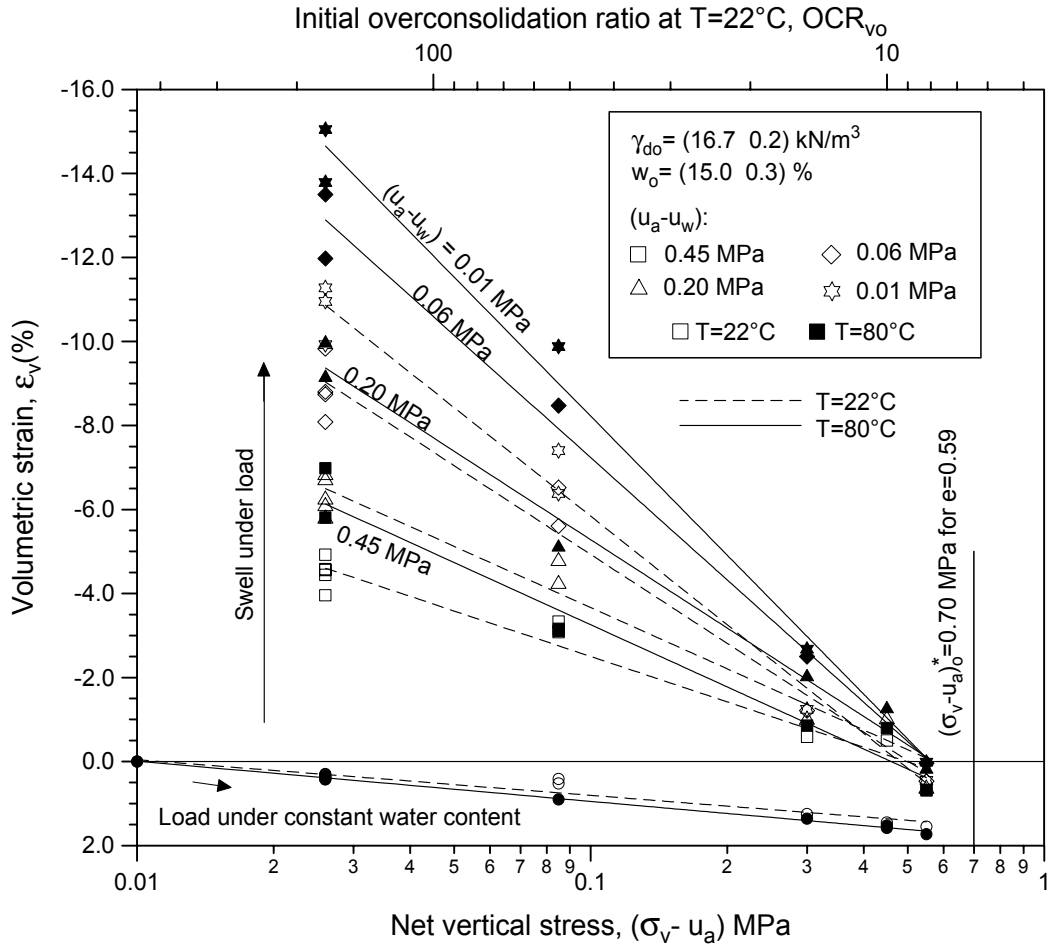

Figure 6.13 Undrained loading and swelling curves for the high-density fabric at different temperatures and matric suction steps for varying applied net vertical stresses (main wetting paths).

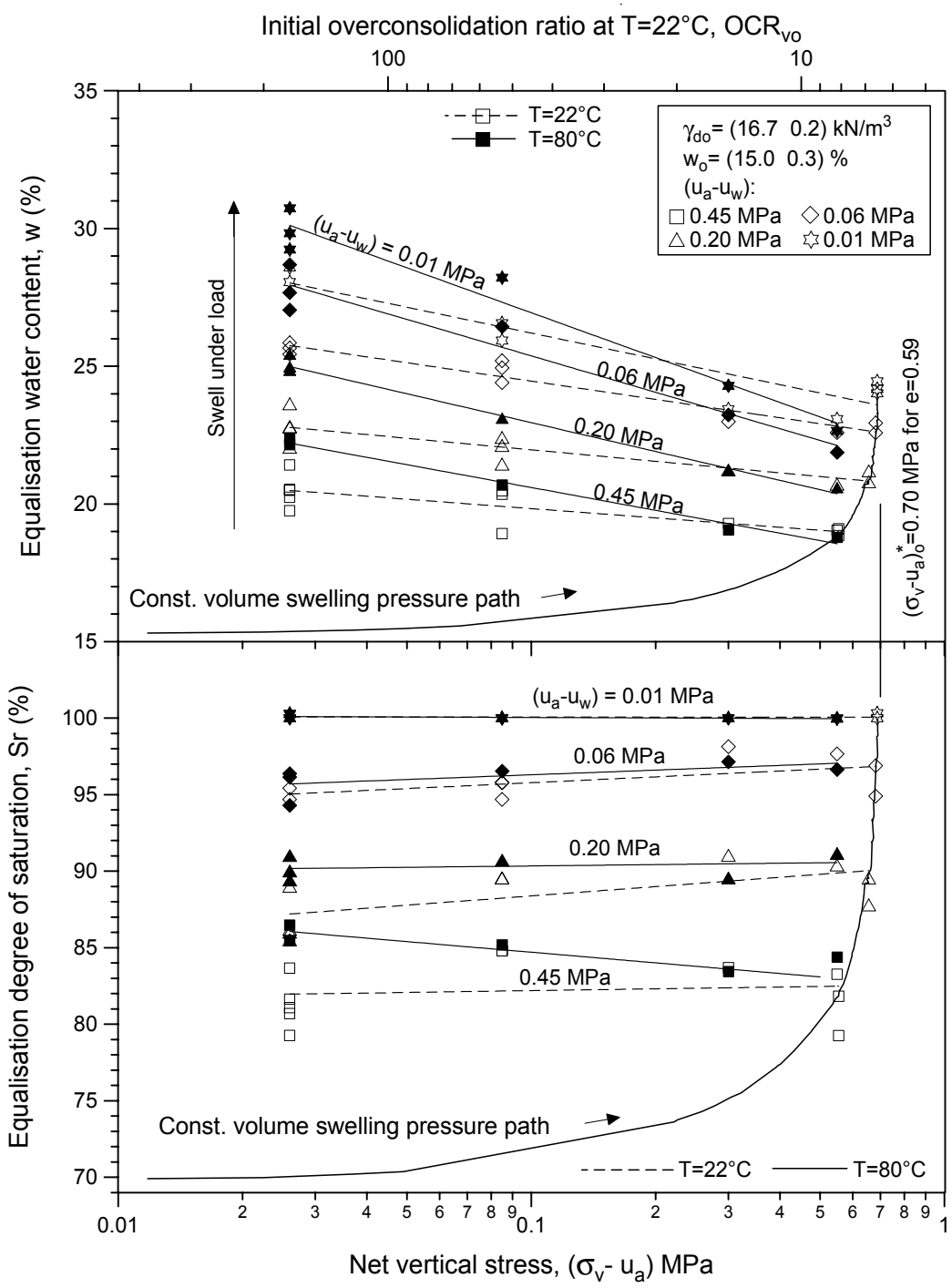

Figure 6.14 Water content and degree of saturation values for the high-density fabric at different temperatures and matric suction steps for varying applied net vertical stresses (main wetting paths).

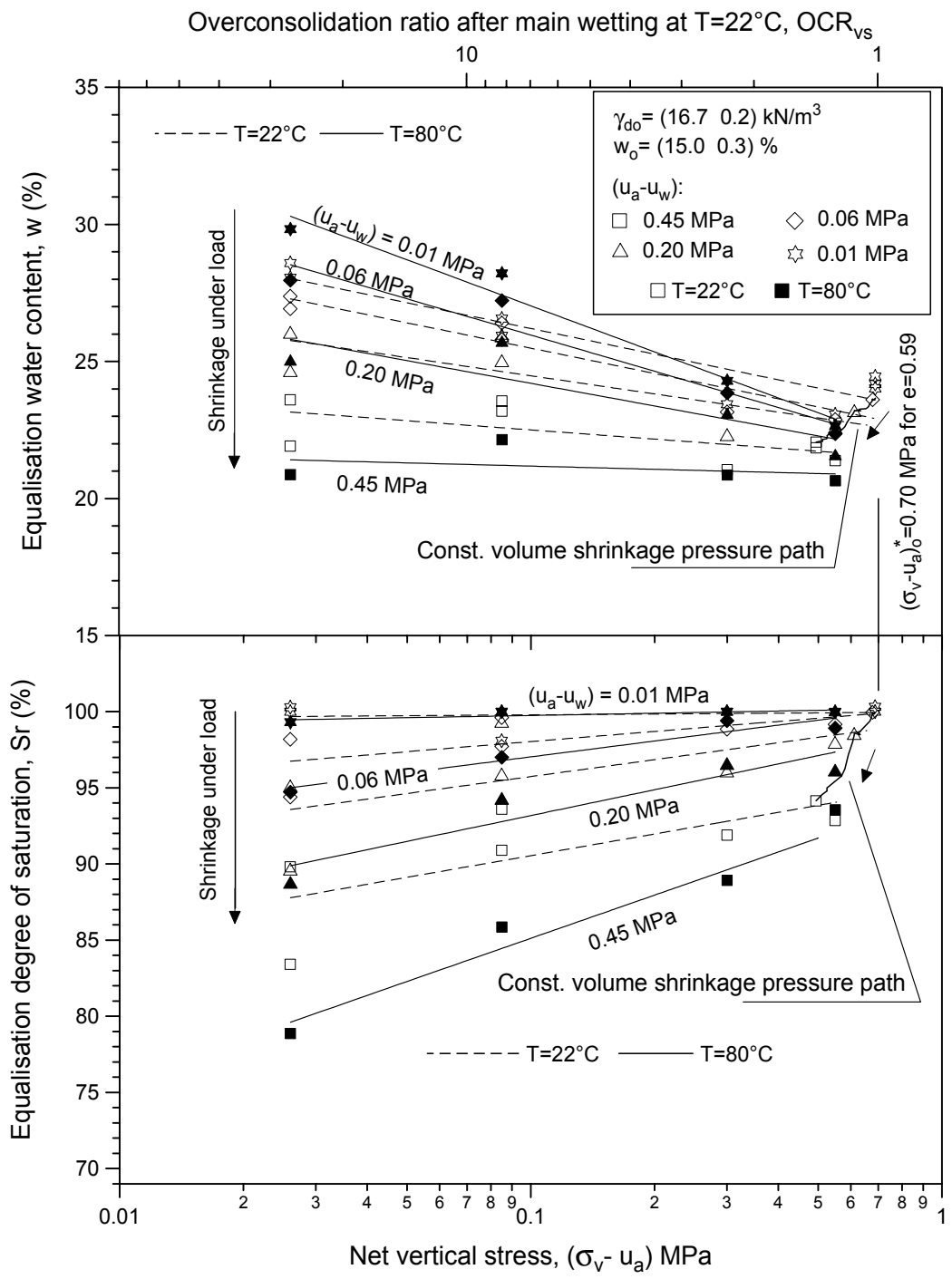

Figure 6.15 Water content and degree of saturation values for the high-density fabric at different temperatures and matric suction steps for varying applied net vertical stresses (main drying paths).

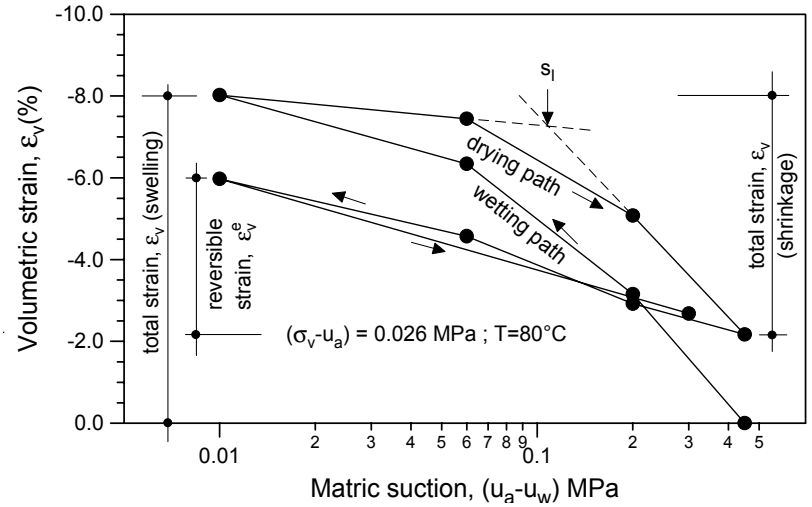

Figure 6.16 Swelling and shrinkage strains for the high-density fabric in wetting-drying cycles.

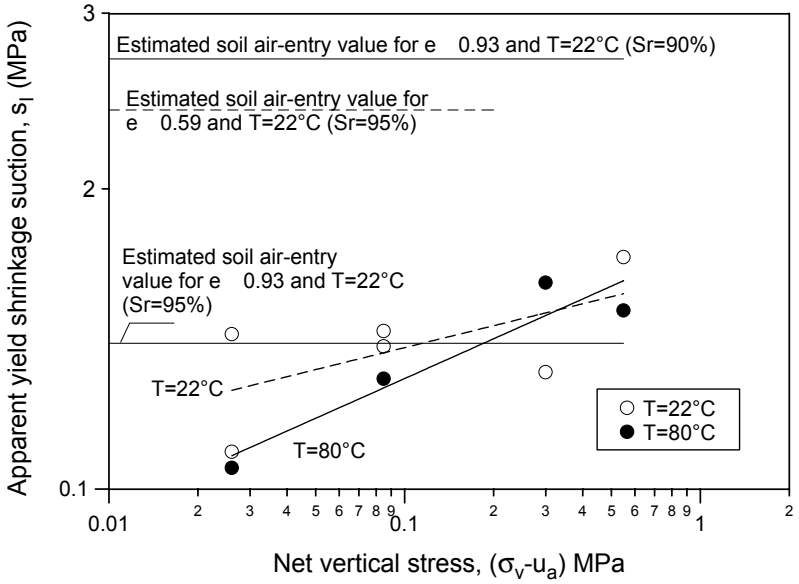

Figure 6.17 Apparent yield shrinkage suction for the high-density packing for different temperatures.

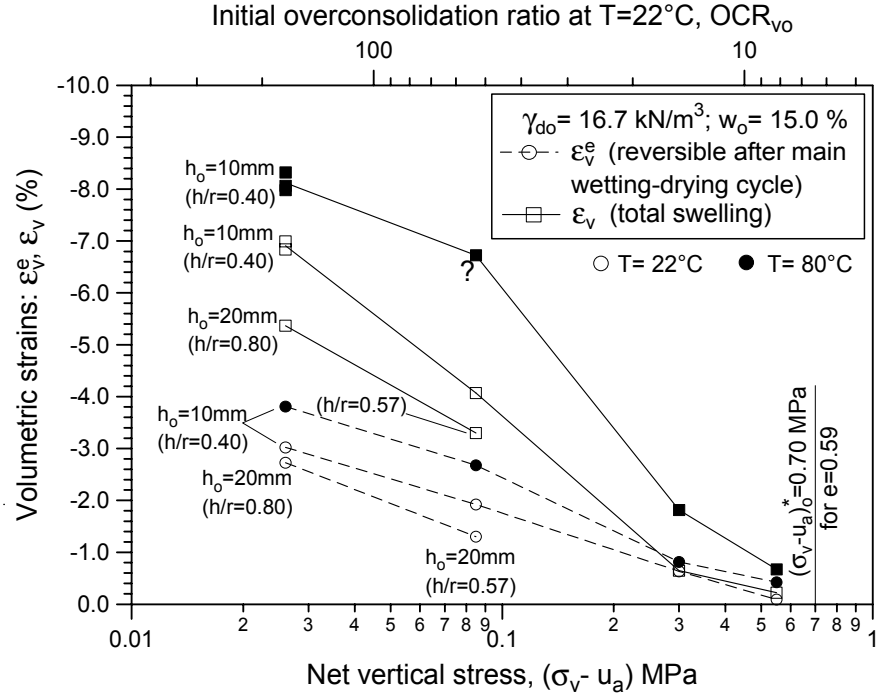

Figure 6.18 Total swelling upon main wetting and reversible strain during scanning wetting at different temperatures and stress conditions (high-density packing).

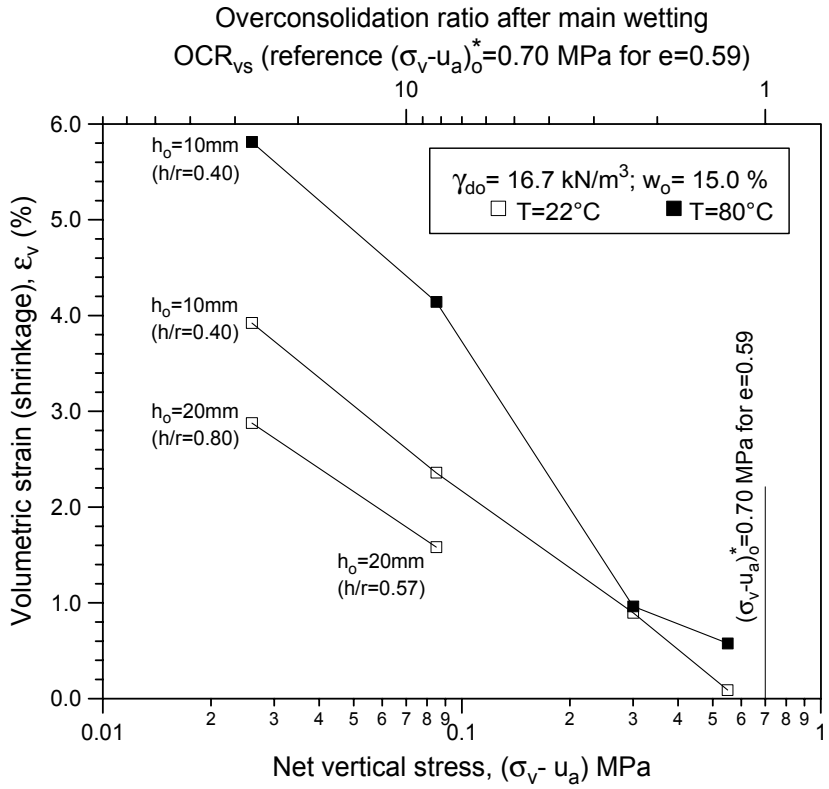

Figure 6.19 Total shrinkage upon main drying at different temperatures and stress conditions (high-density packing).

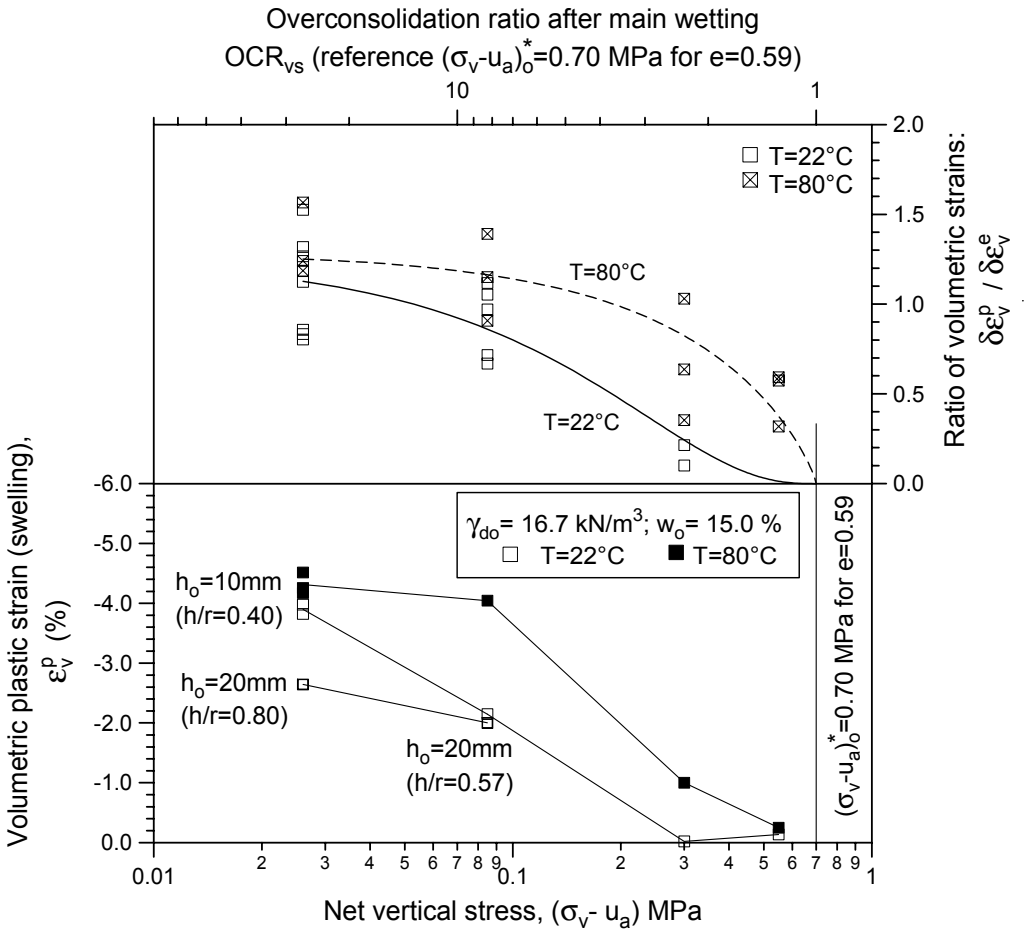

Figure 6.20 Irreversible swelling strains in wetting-drying-wetting cycles at different temperatures and stress conditions (high-density packing). Relationship between plastic and reversible strains.

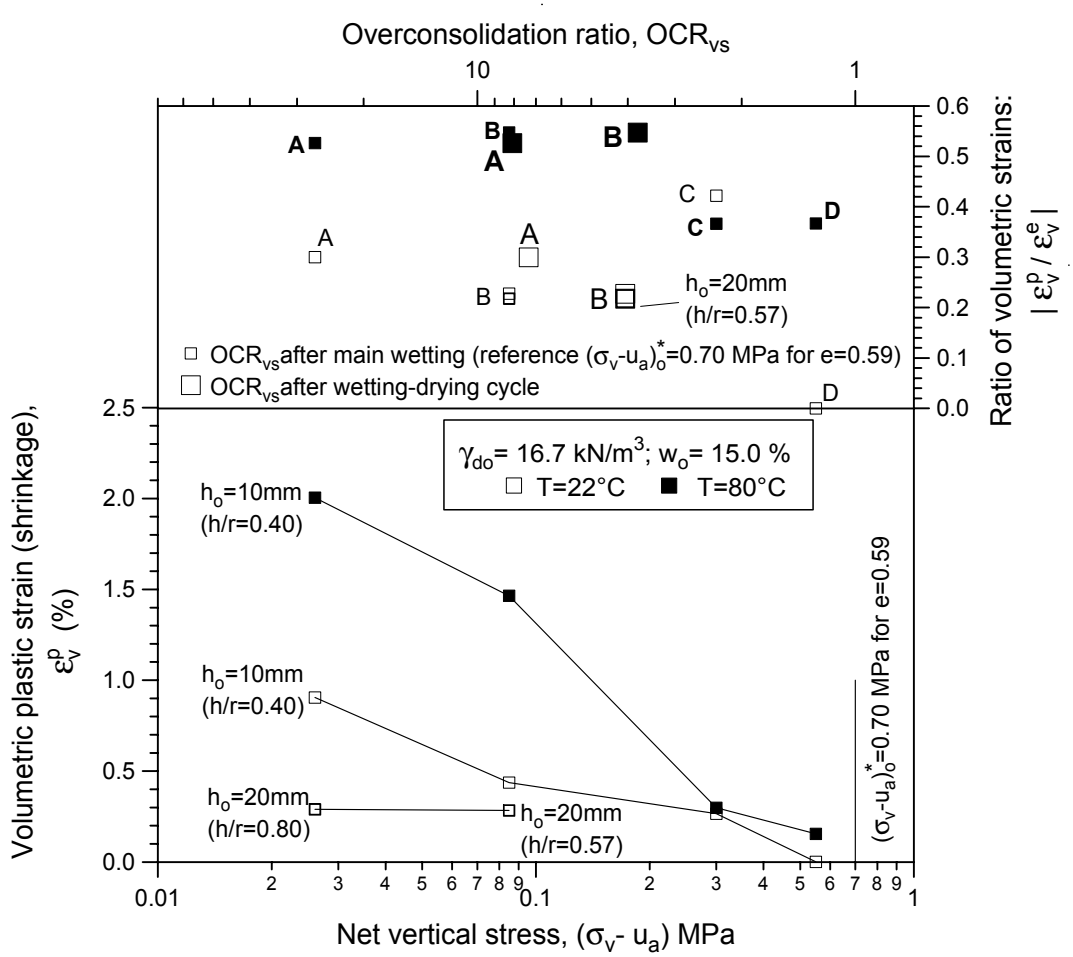

Figure 6.21 Irreversible shrinkage strains in drying-wetting cycles at different temperatures and stress conditions (high-density packing). Relationship between plastic and reversible strains.

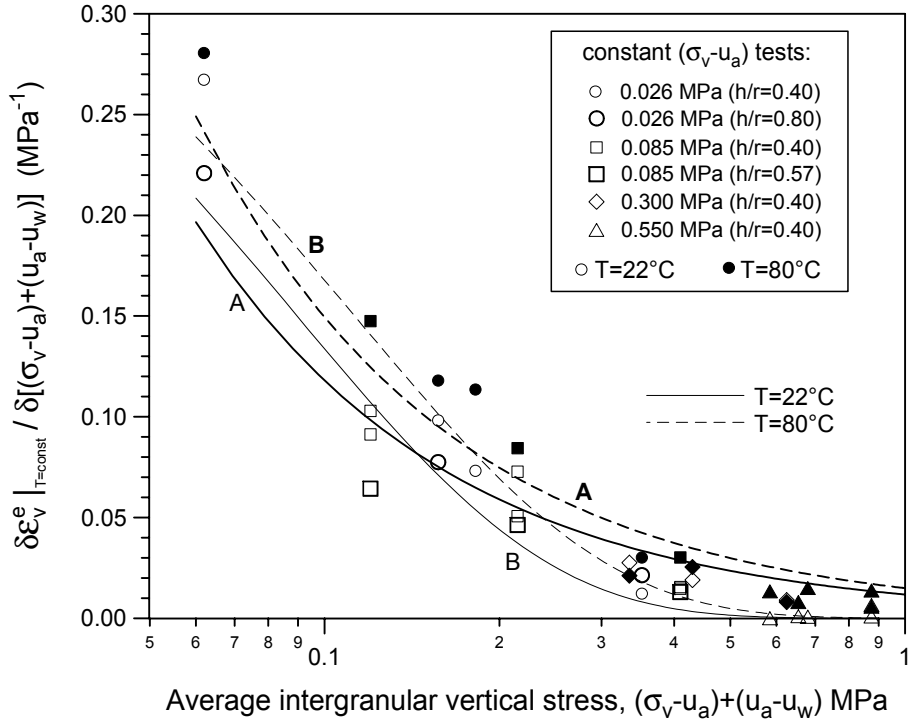

Figure 6.22 Isothermal changes in elastic strain associated with changes in intergranular vertical stress obtained from constant (σ_v-u_a) data (high-density fabric).

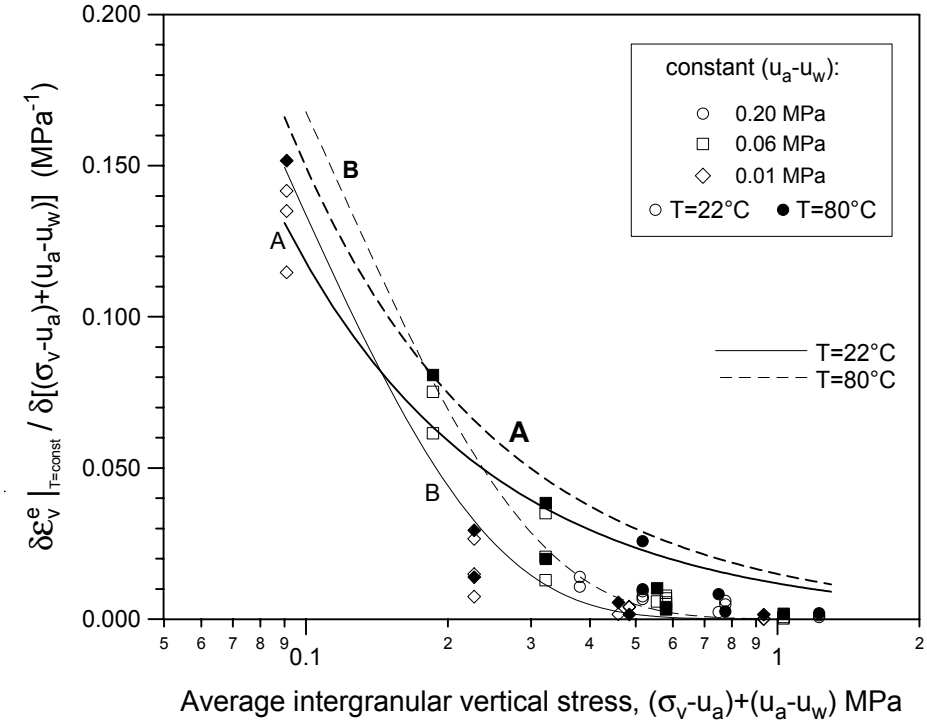

Figure 6.23 Isothermal changes in elastic strain associated with changes in intergranular vertical stress obtained from constant (u_a-u_w) data (high-density fabric).

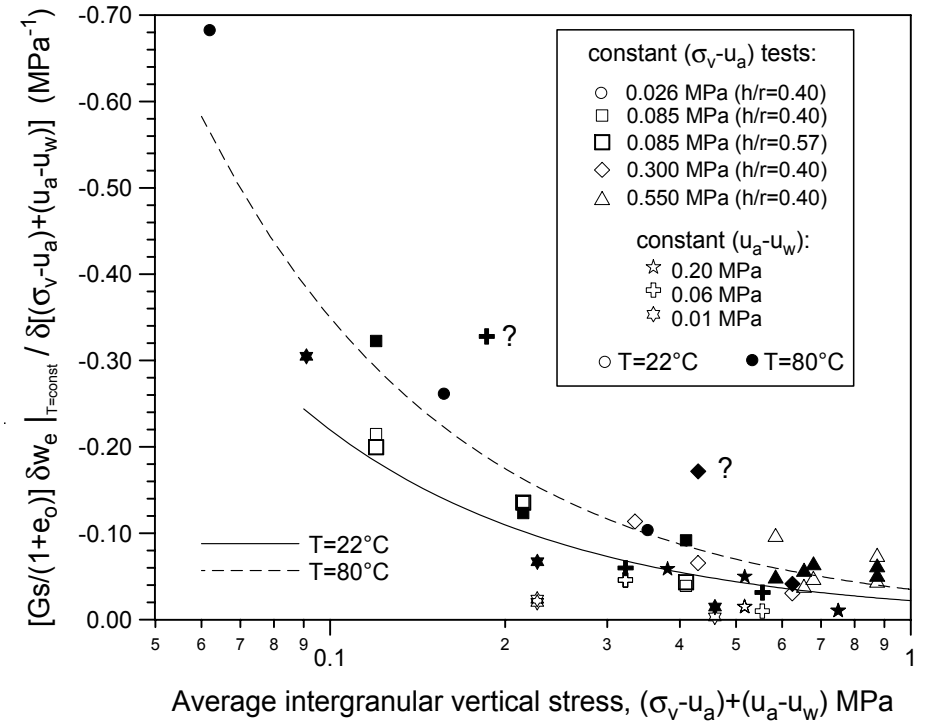

Figure 6.24 Isothermal reversible changes in work conjugate variable of matric suction with changes in intergranular vertical stress obtained from constant (σ_v-u_a) and (u_a-u_w) data (high-density fabric).

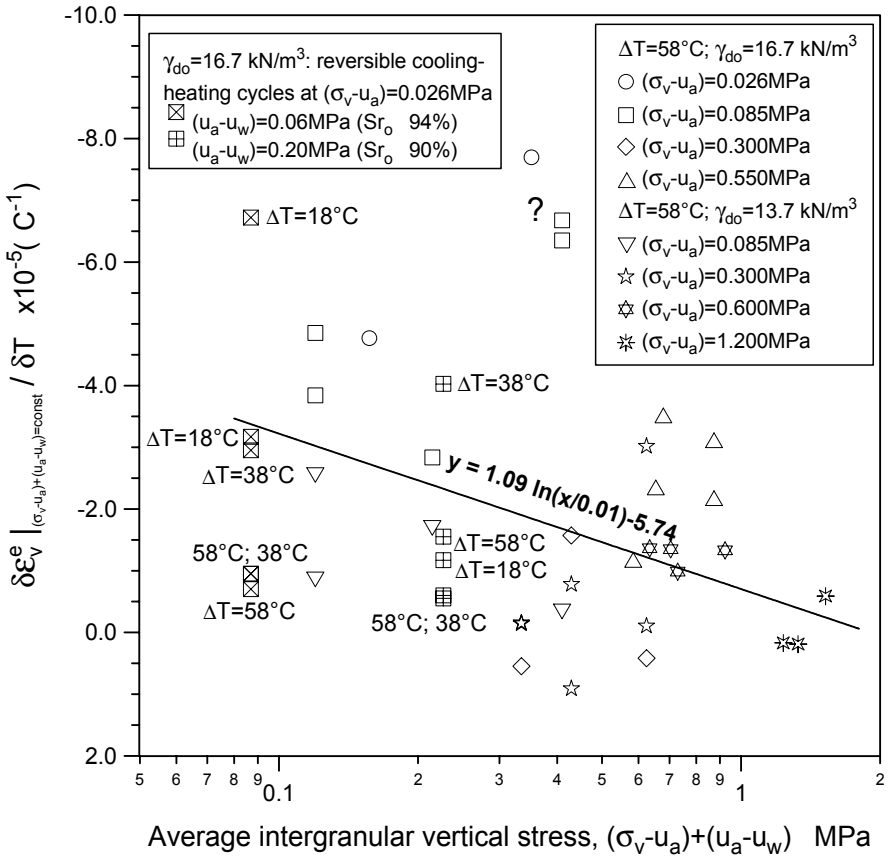

Figure 6.25 Drained reversible thermal coefficients for high-density and high-porosity packings under constant vertical stress.

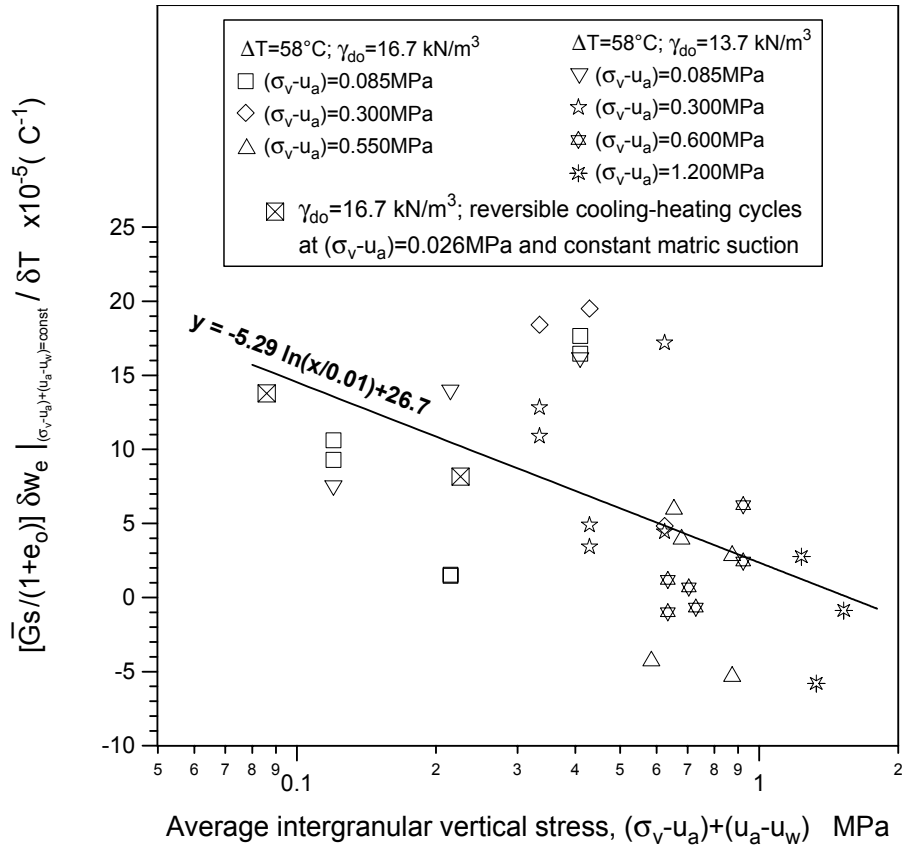

Figure 6.26 Drained reversible aspects of matric suction work conjugate variable with changes in temperature (high-density and high-porosity packings).

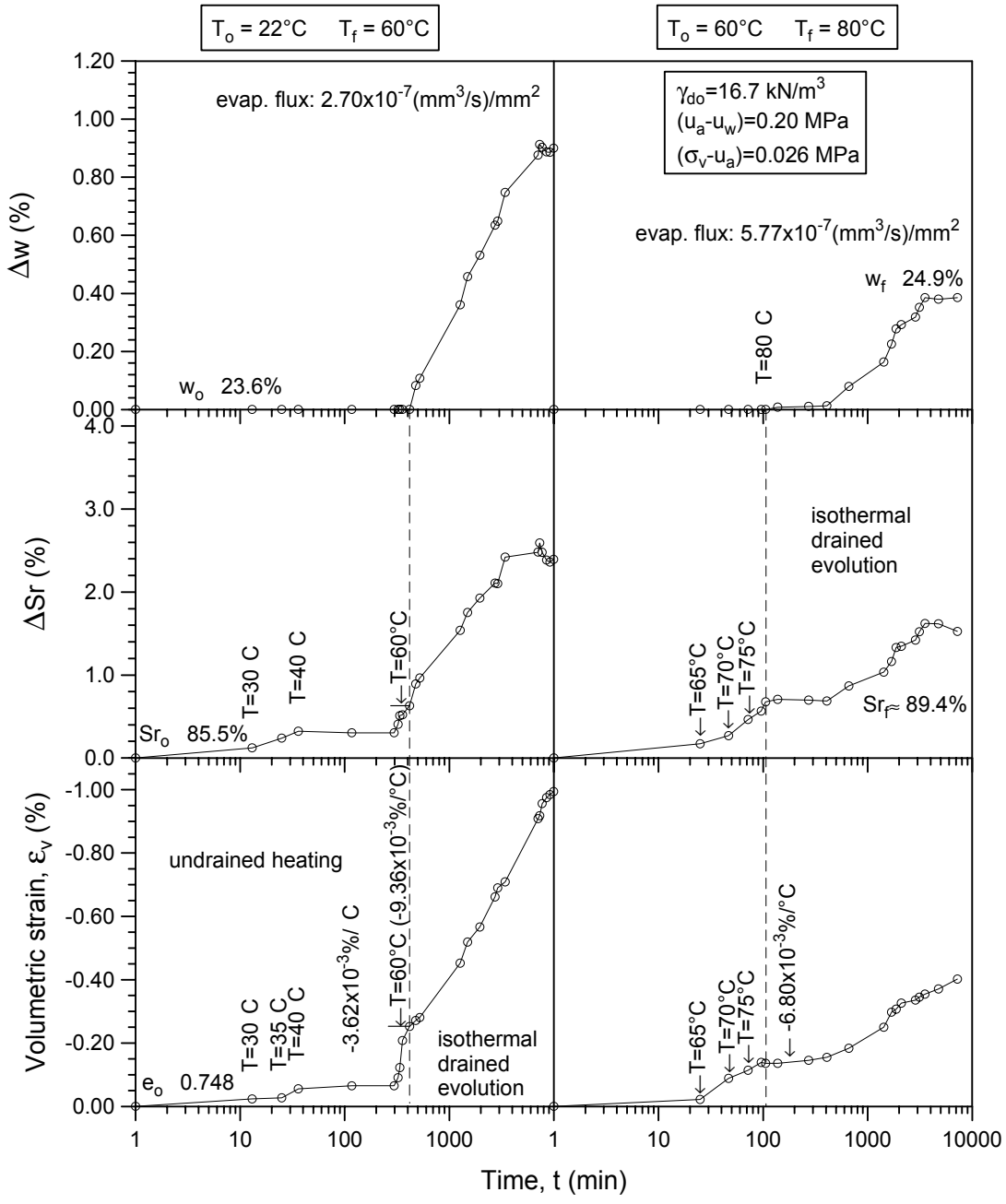

Figure 6.27 Time evolution of volumetric strain, water content and degree of saturation during a drained heating path at constant net vertical stress and (u_a-u_w) = 0.20 MPa (high-density fabric).

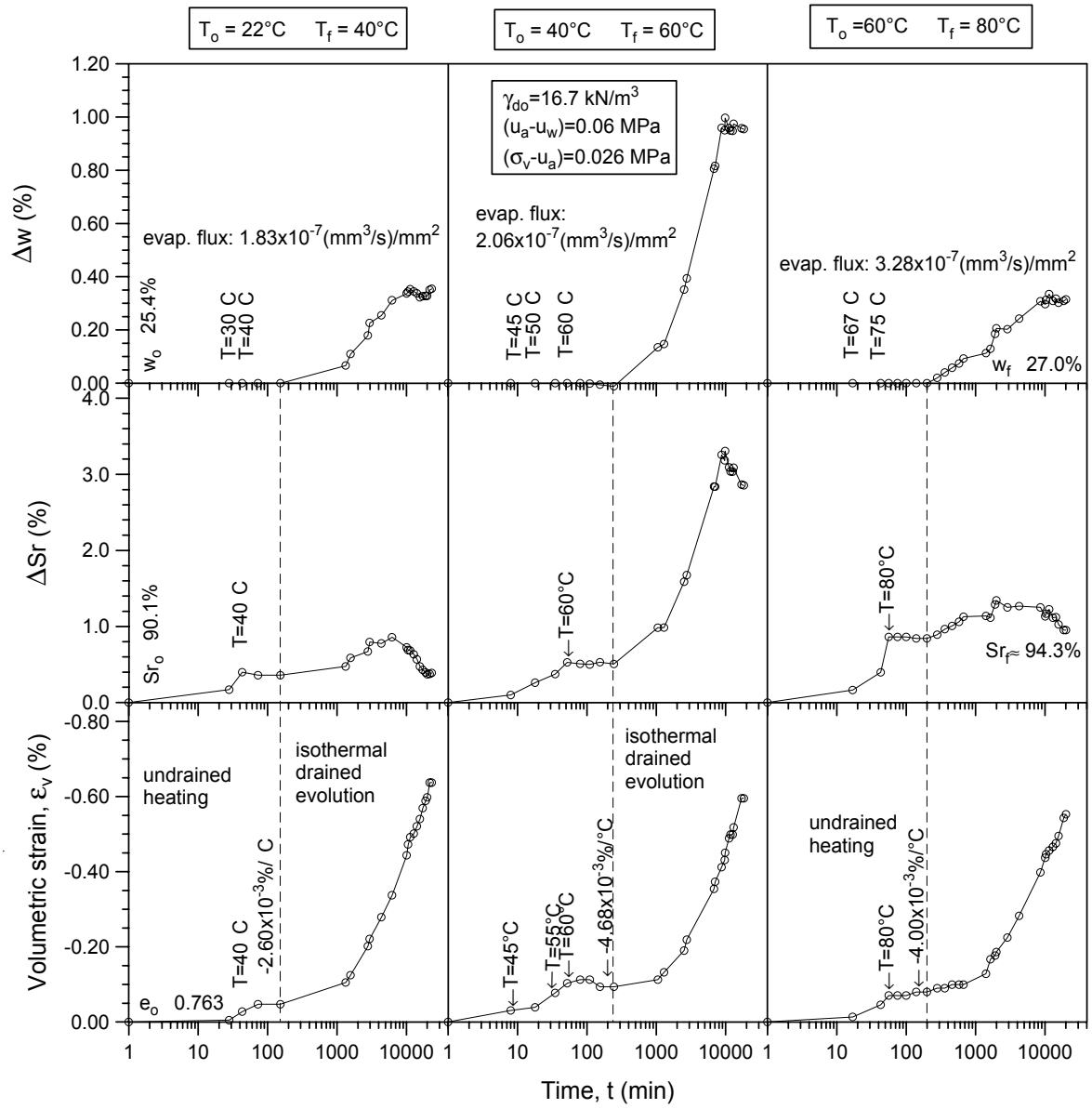

Figure 6.28 Time evolution of volumetric strain, water content and degree of saturation during a drained heating path at constant net vertical stress and (u_a-u_w) = 0.06 MPa (high-density fabric).

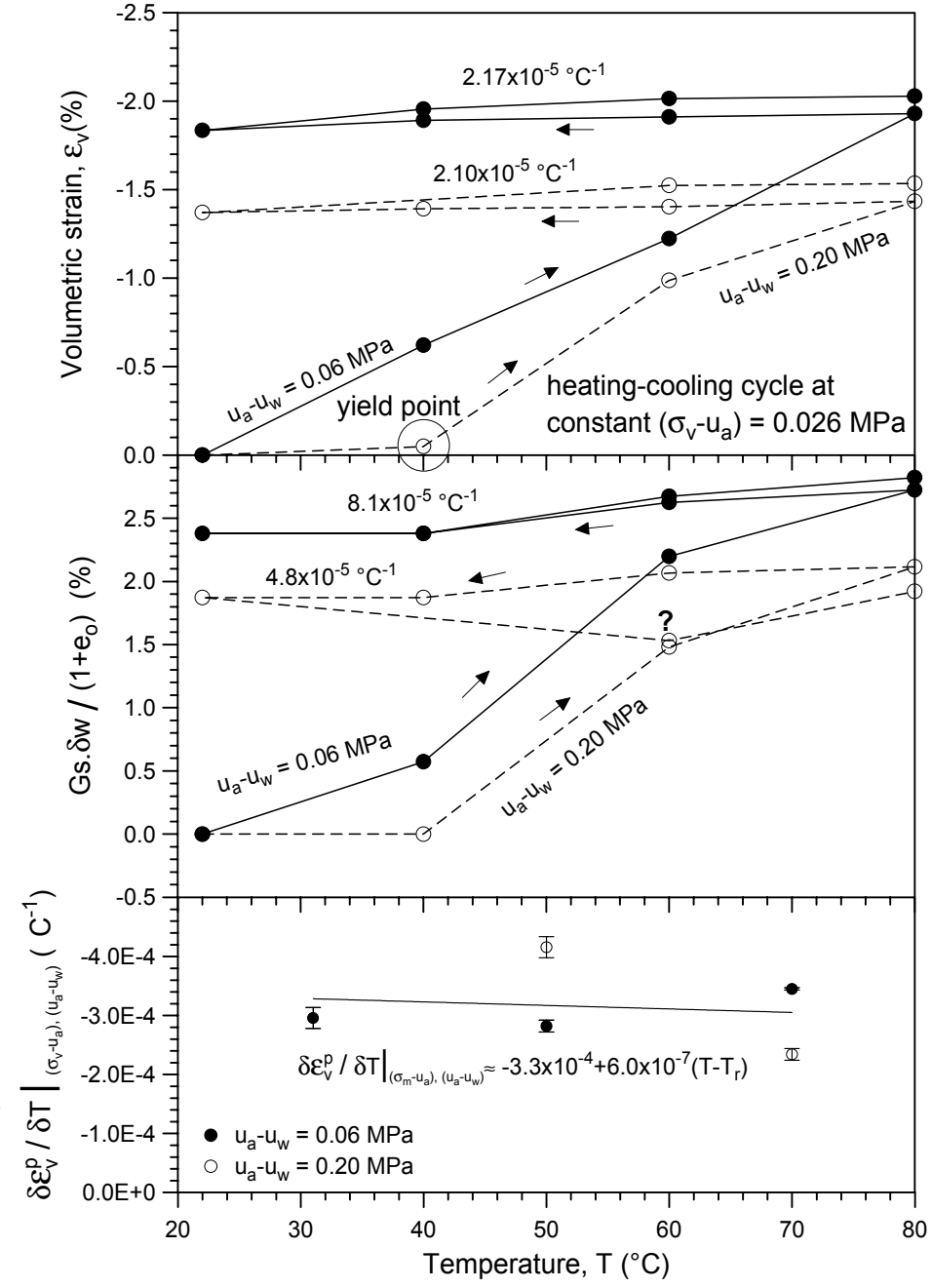

Figure 6.29 Drained heating-cooling cycles at constant matric suctions and under (σ_v-u_a) = 0.026 MPa (high-density fabric).

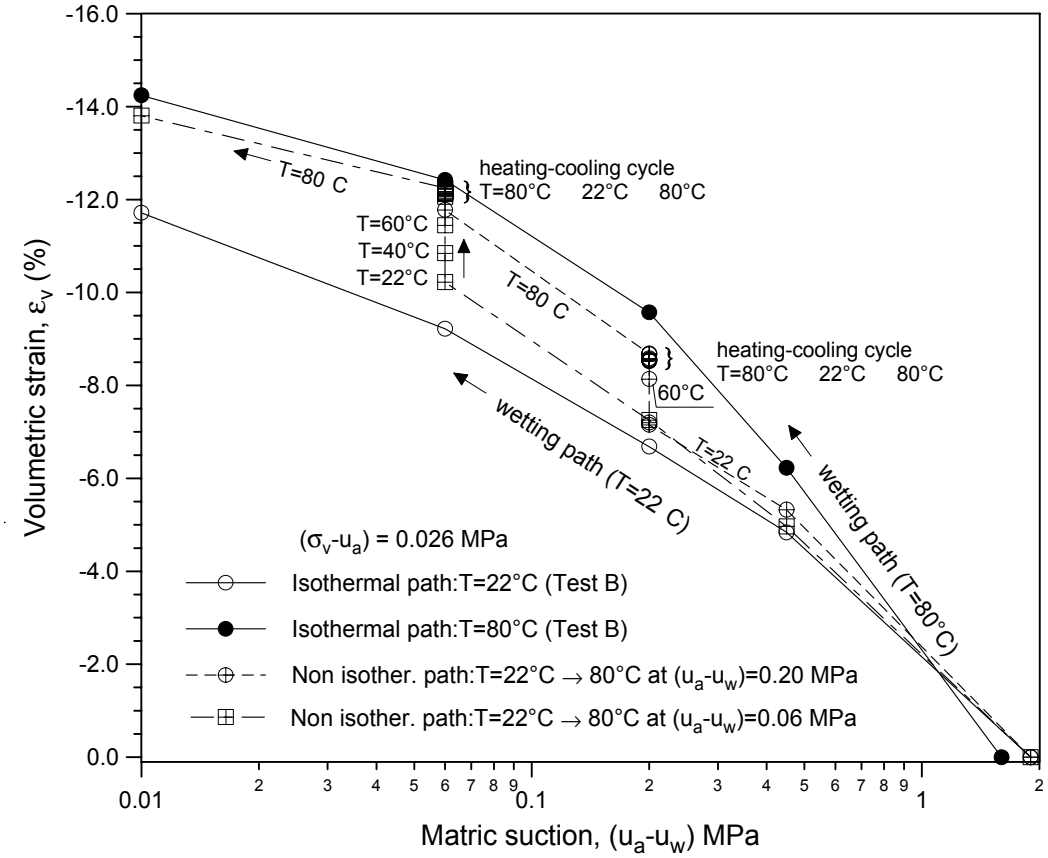

Figure 6.30 Non-isothermal paths compared to isothermal main wetting paths in terms of volumetric strains (high-density packing at (σ_v-u_a) = 0.026 MPa).

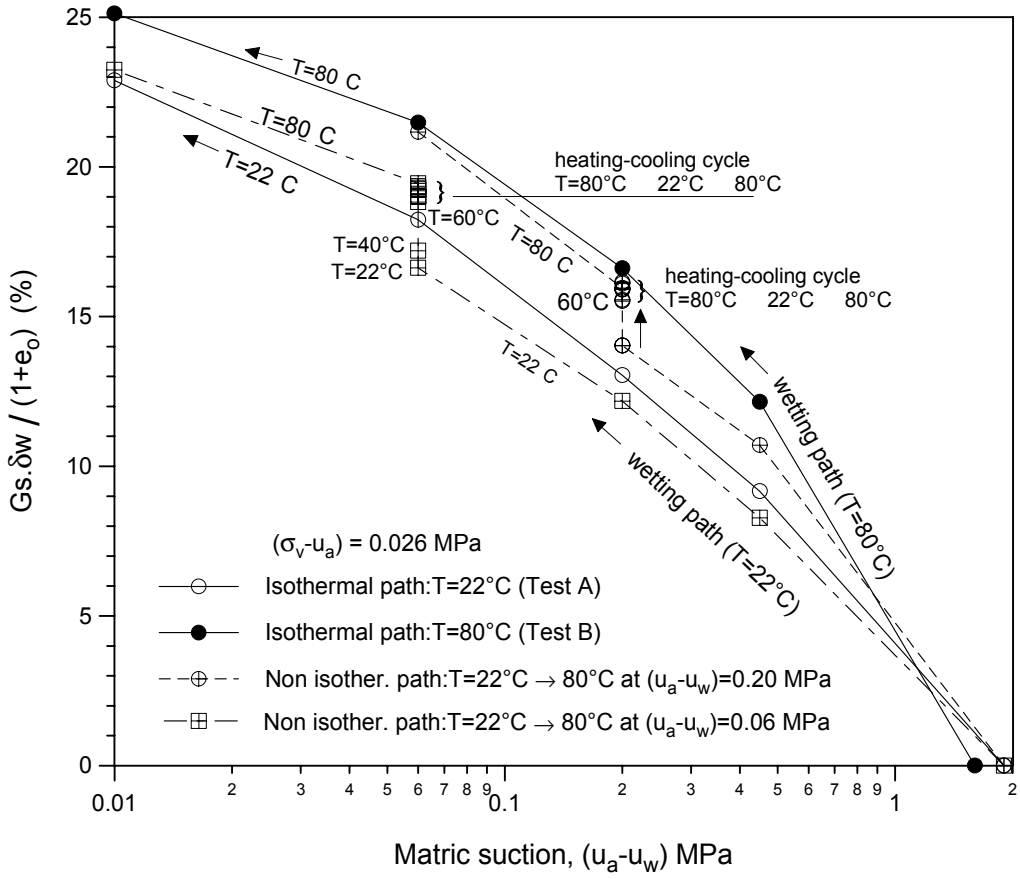

Figure 6.31 Non-isothermal paths compared to isothermal main wetting paths in terms of matric suction work conjugate variable (high-density packing at (σ_v-u_a) = 0.026 MPa).

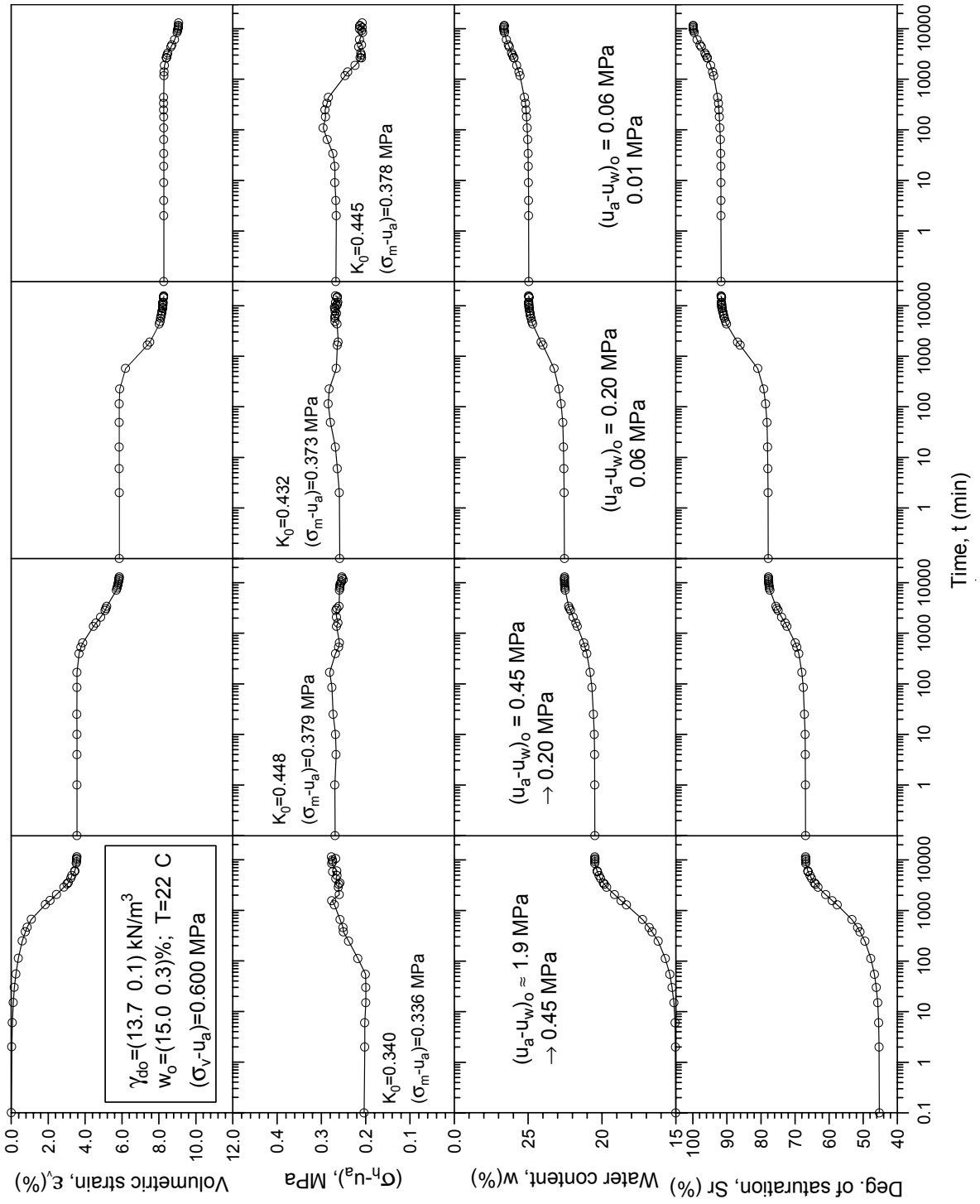

Figure 6.32 Time evolution of volumetric strain, net lateral stress, water content and degree of saturation at 22°C for the high-porosity packing in a main wetting process.

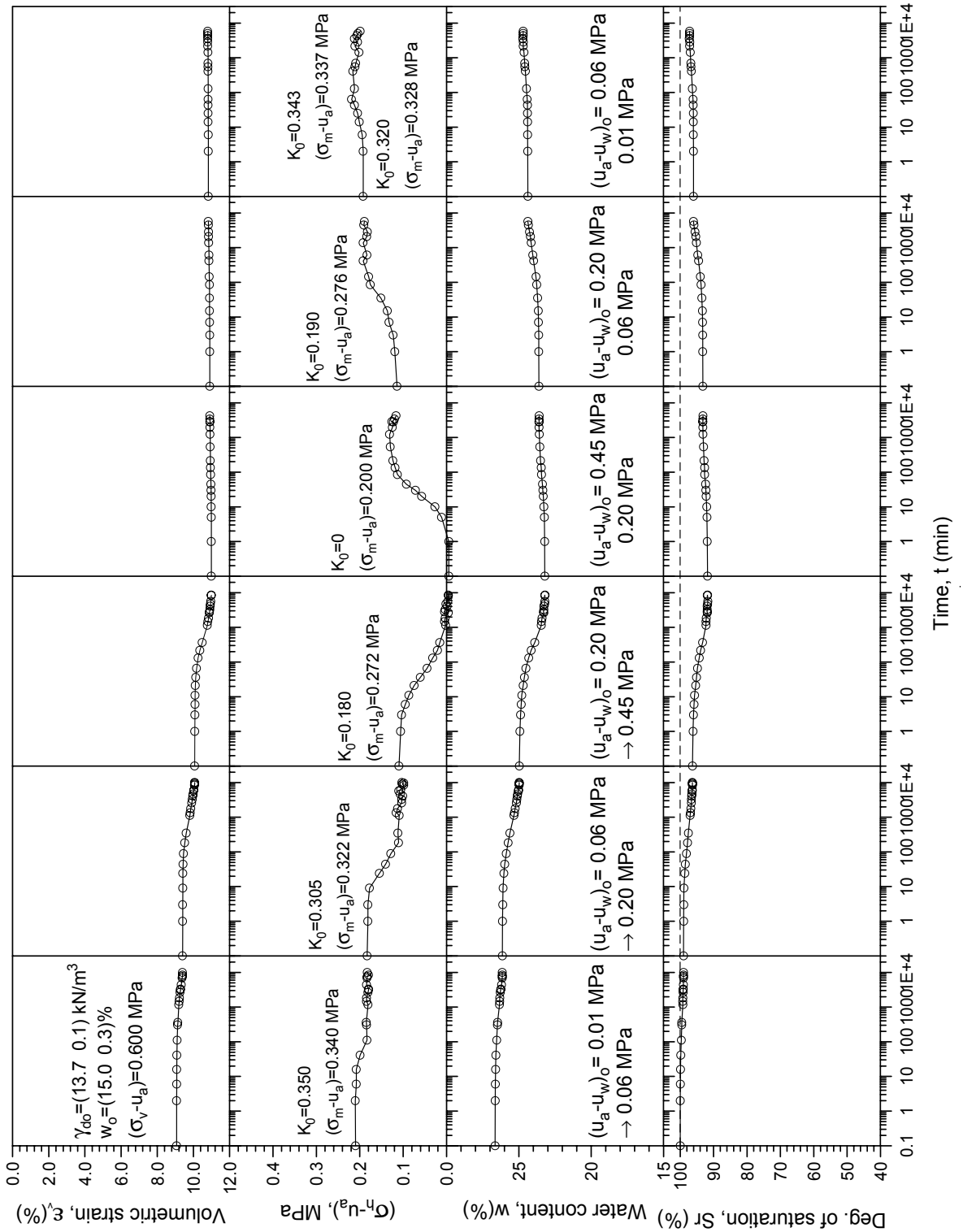

Figure 6.33 Time evolution of volumetric strain, net lateral stress, water content and degree of saturation at 22°C for the high-porosity packing in a main drying and wetting cycle.

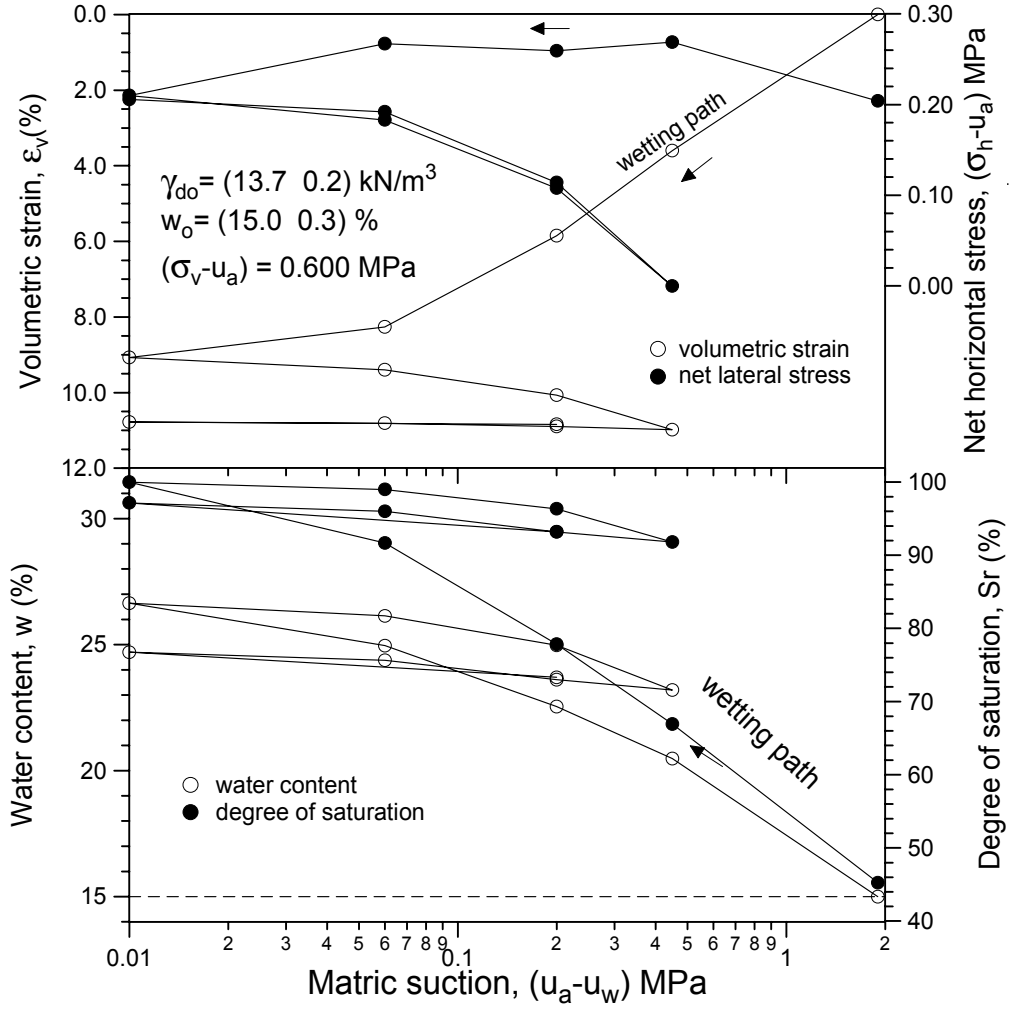

Figure 6.34 Variation of volumetric strain, net horizontal stress, water content and degree of saturation for the high-porosity fabric in wetting-drying cycles under constant net vertical stress (T=22°C).

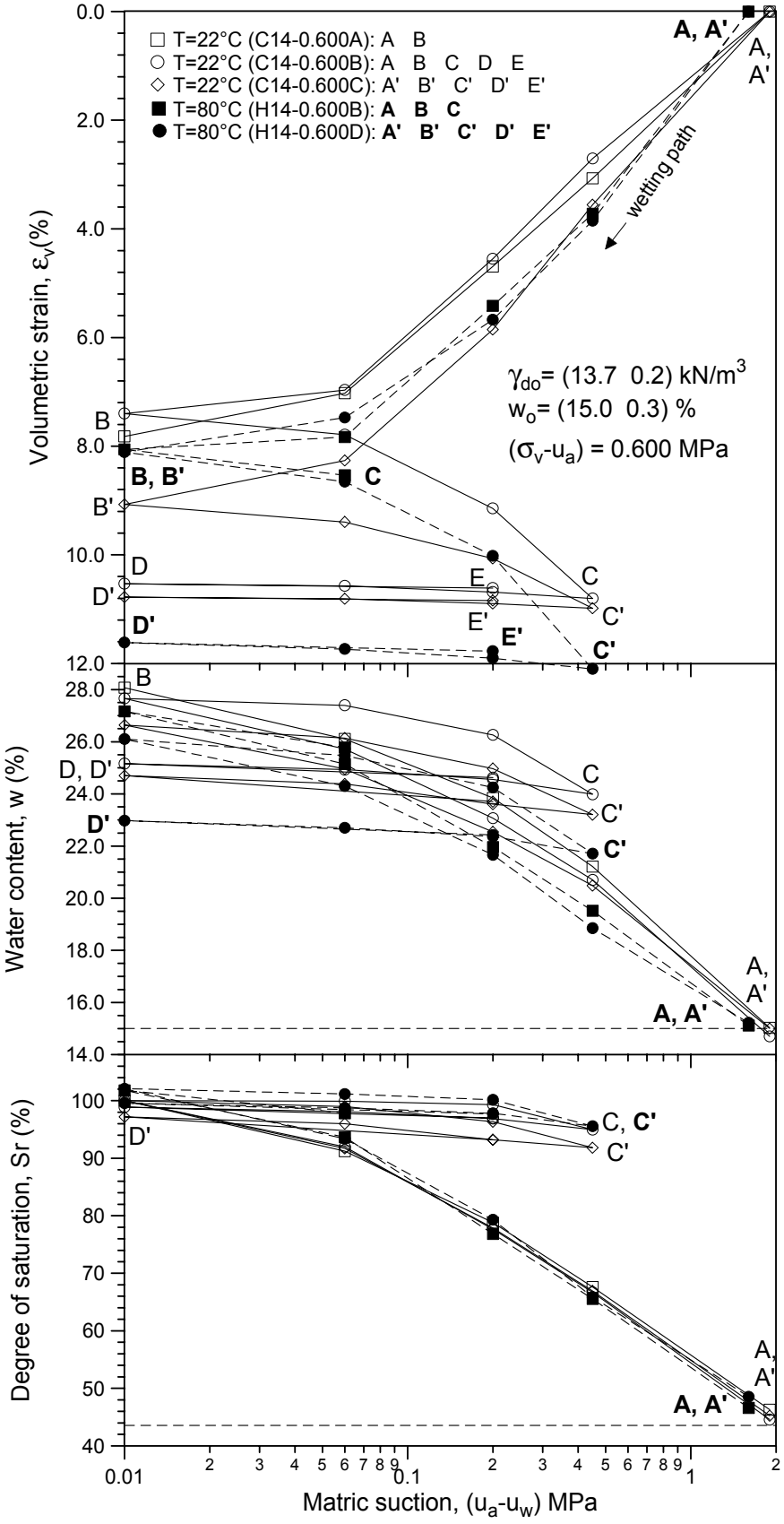

Figure 6.35 Variation of volumetric strain, water content and degree of saturation for the high-porosity fabric in wetting-drying cycles at two different temperatures and under constant (σ_v-u_a) = 0.600 MPa.

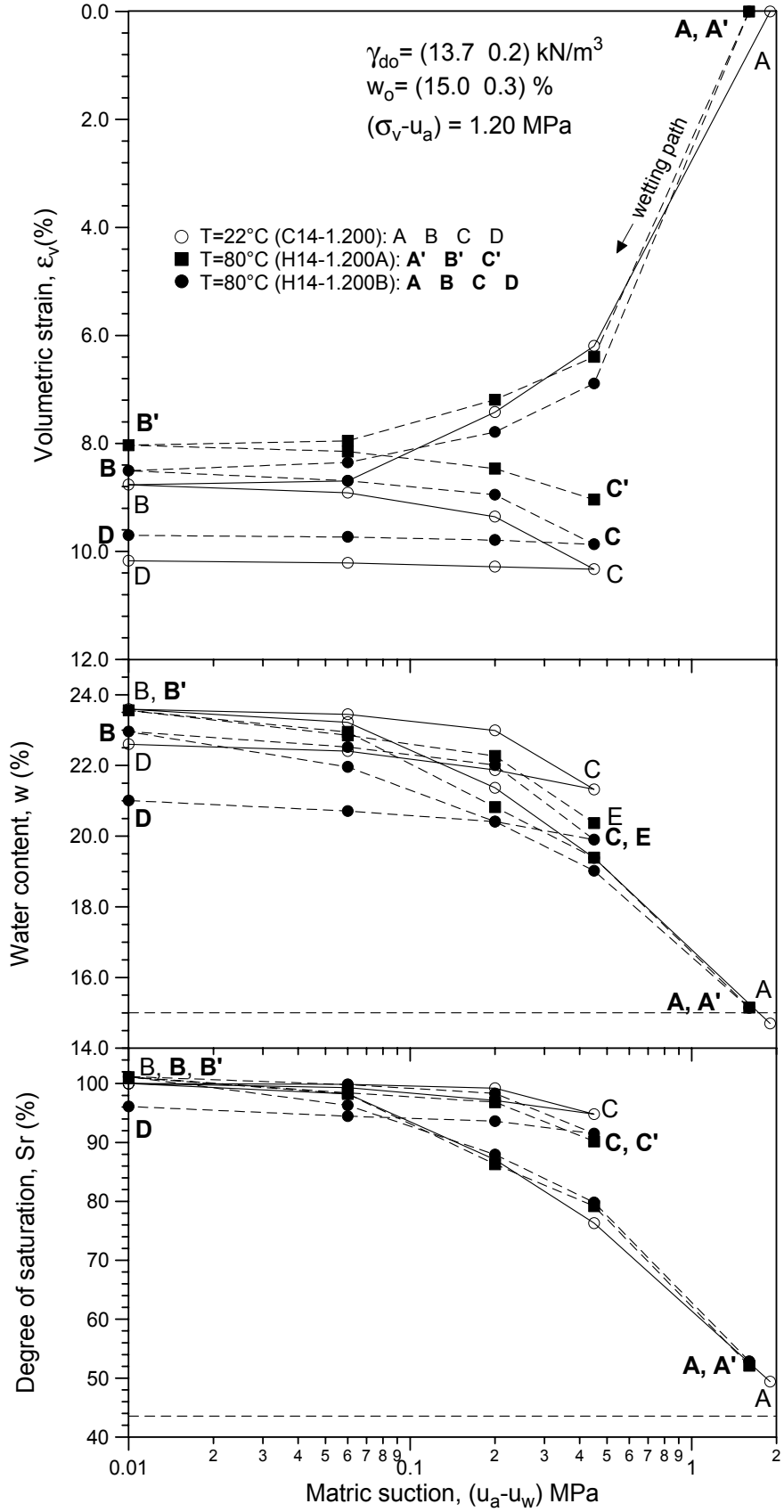

Figure 6.36 Variation of volumetric strain, water content and degree of saturation for the high-porosity fabric in wetting-drying cycles at two different temperatures and under constant (σ_v-u_a) = 1.200 MPa.

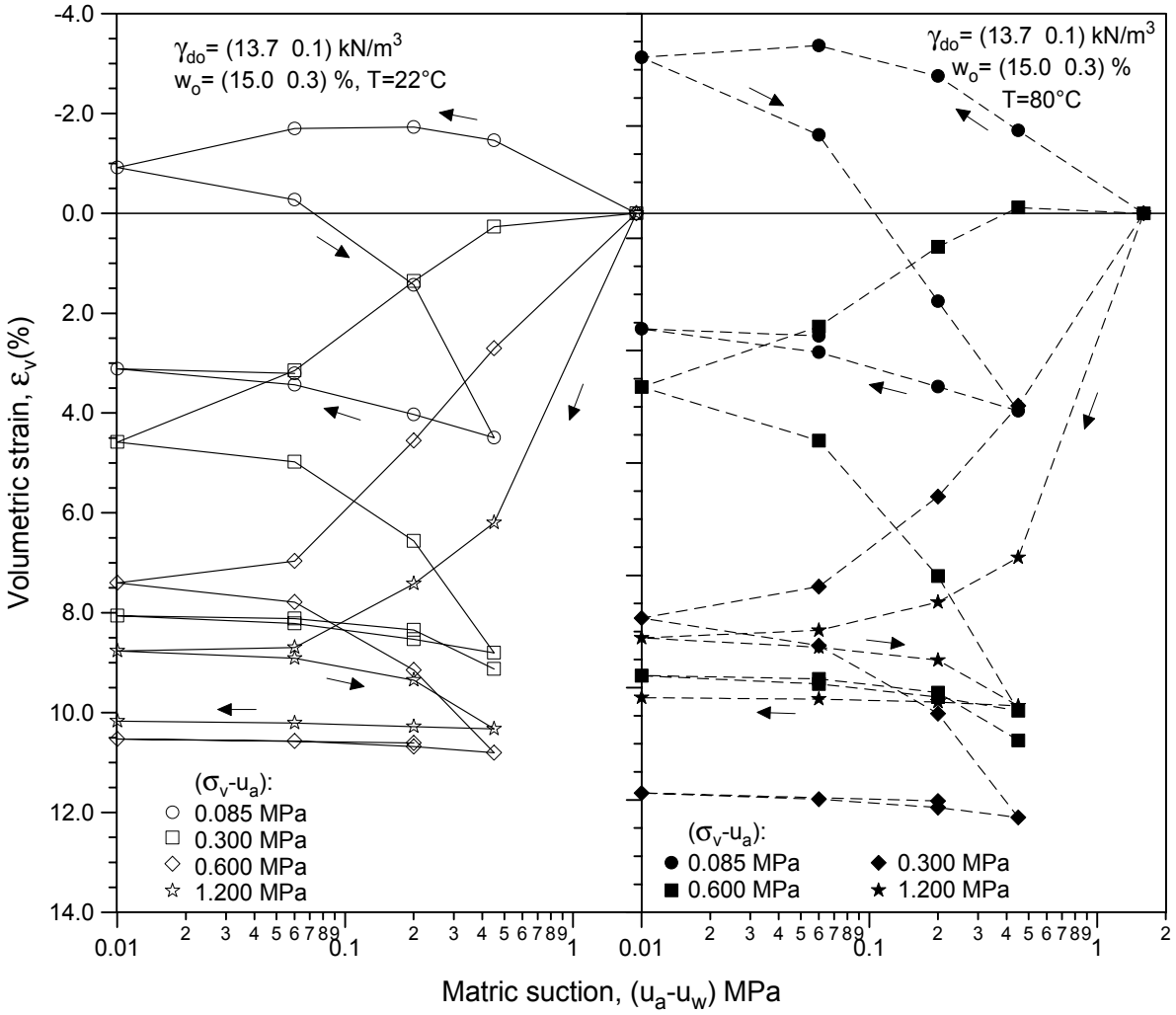

Figure 6.37 Comparison of volumetric strains for the high-porosity fabric in wetting-drying cycles at different net vertical stresses and temperatures.

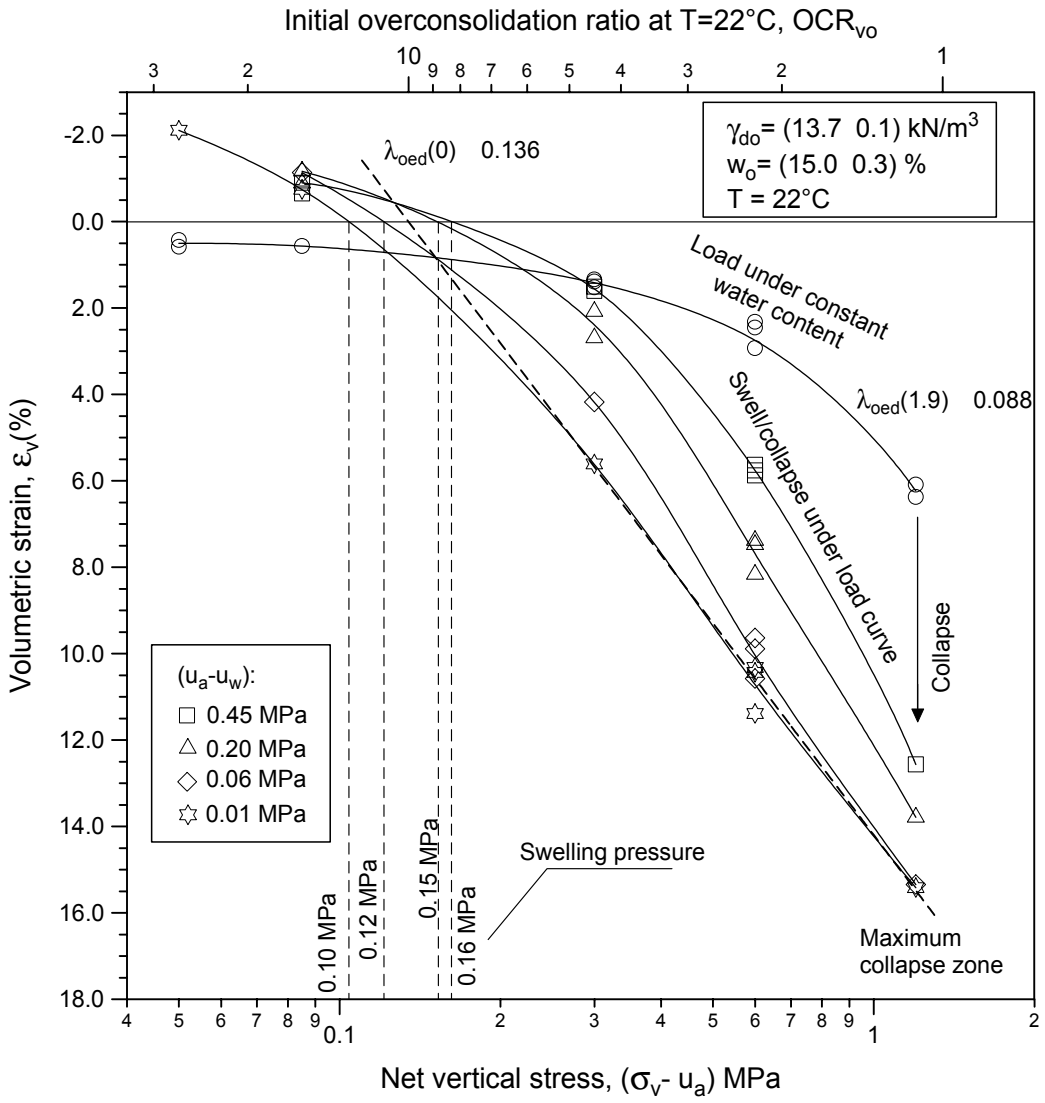

Figure 6.38 Undrained loading and swell/collapse under load curves for the high-porosity fabric for different matric suction steps and T=22°C (main wetting paths).

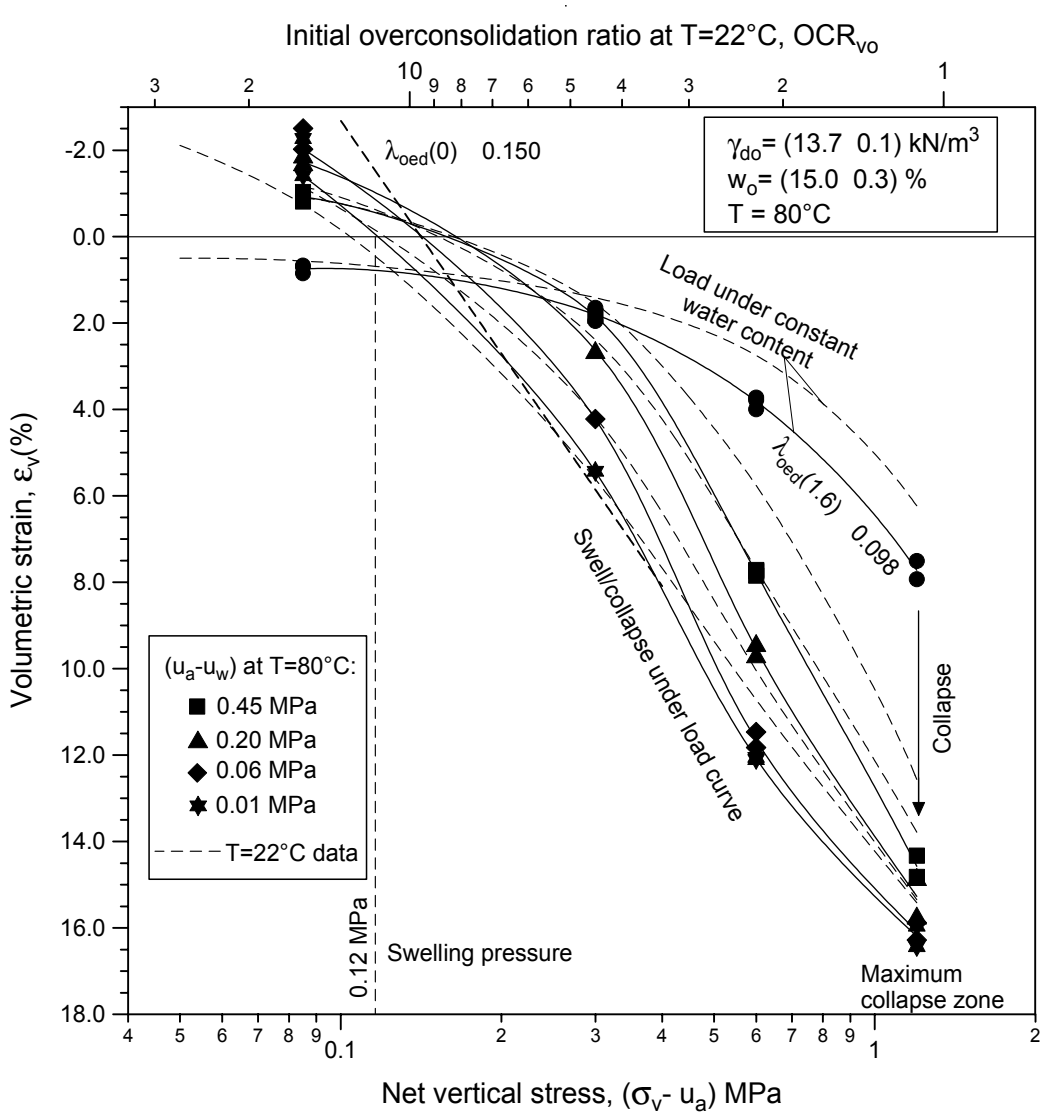

Figure 6.39 Undrained loading and swell/collapse under load curves for the high-porosity fabric for different matric suction steps and temperatures (main wetting paths).

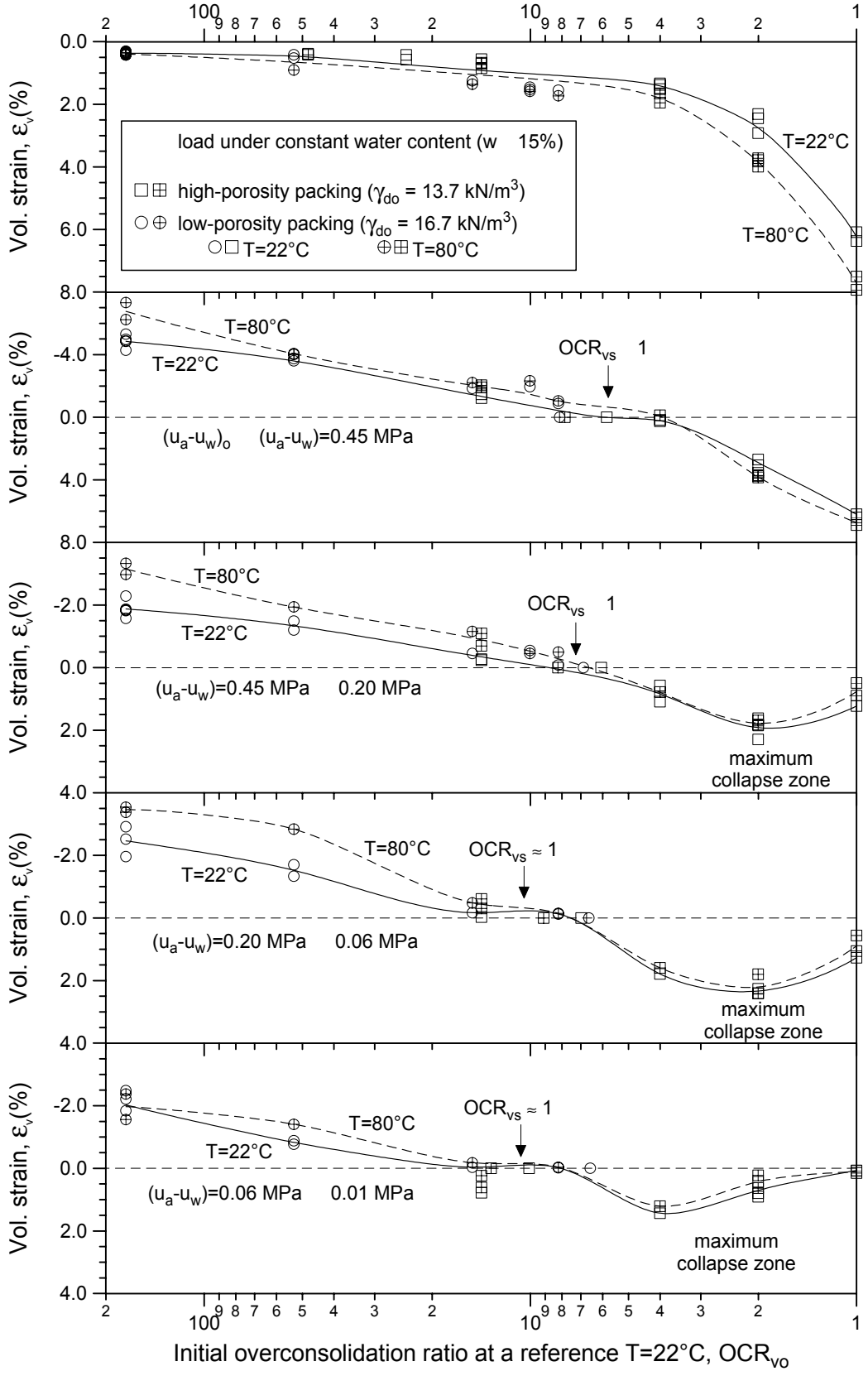

Figure 6.40 Undrained loading and swell/collapse under load curves for different matric suction steps and temperatures as a function of OCR_{vo} (high-density and high-porosity packings).

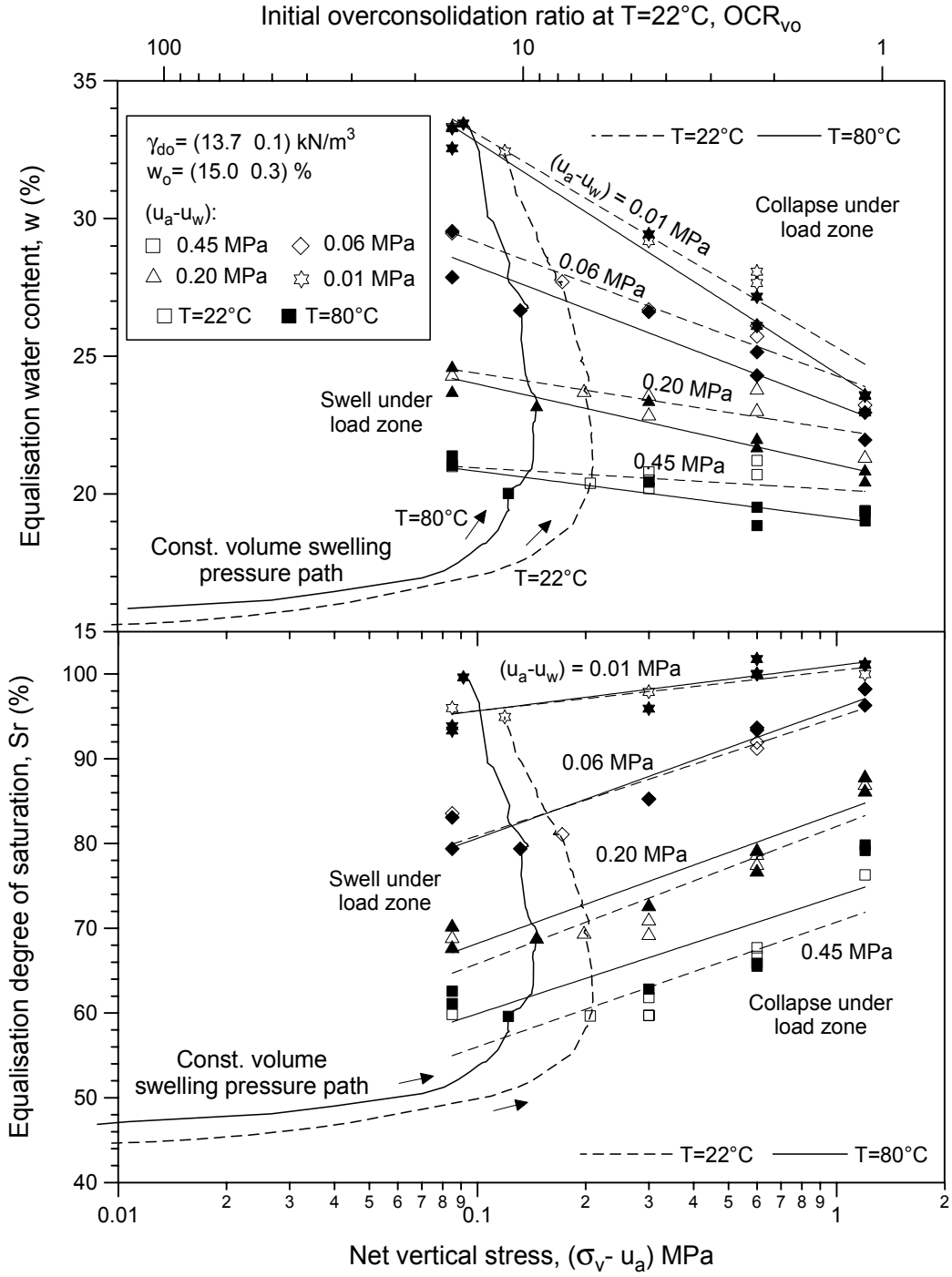

Figure 6.41 Water content and degree of saturation values for the high-porosity fabric at different temperatures and matric suction steps for varying applied net vertical stresses (main wetting paths).

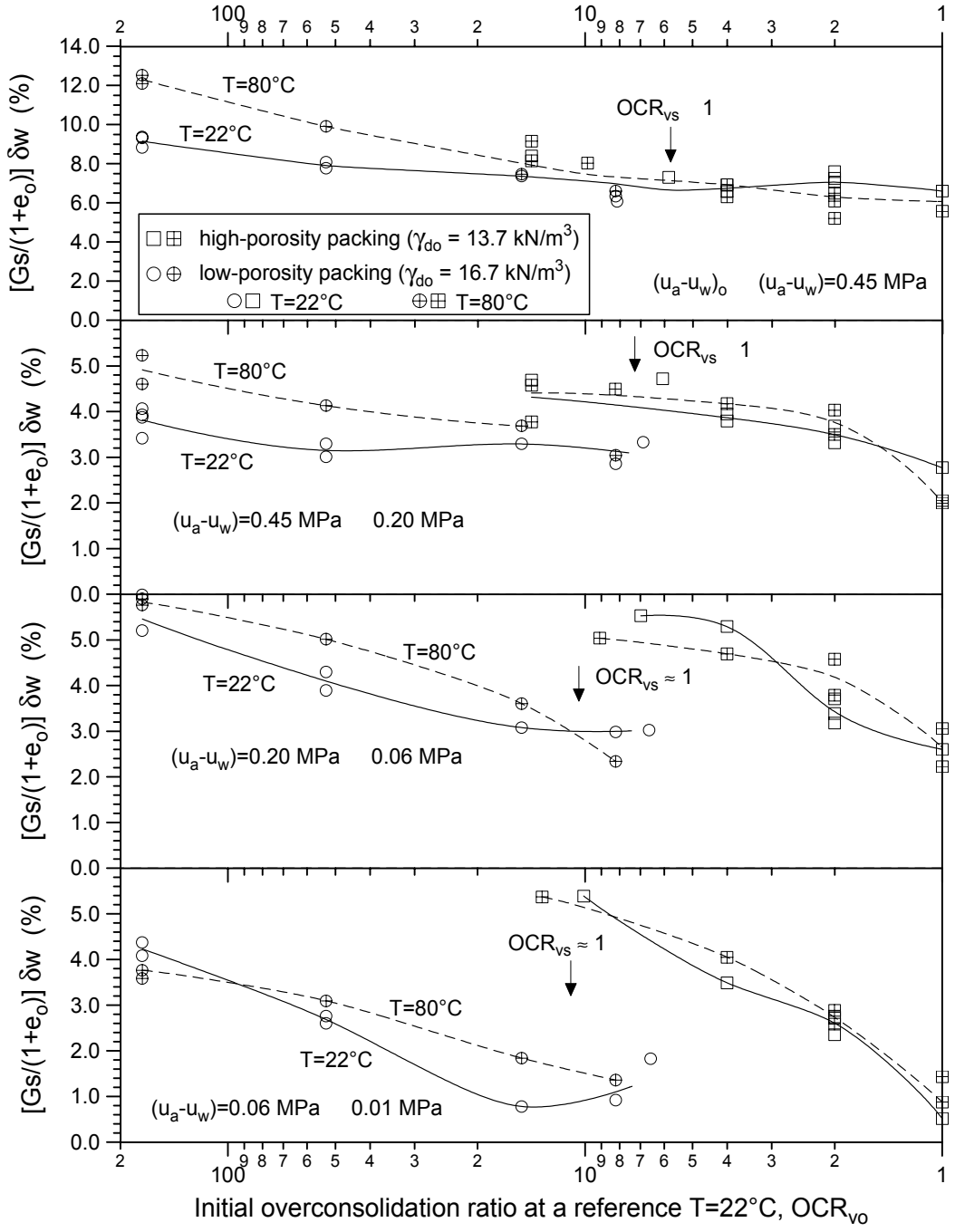

Figure 6.42 Matric suction work conjugate variable changes for different matric suction steps and temperatures as a function of OCR_{vo} (high-density and high-porosity packings).

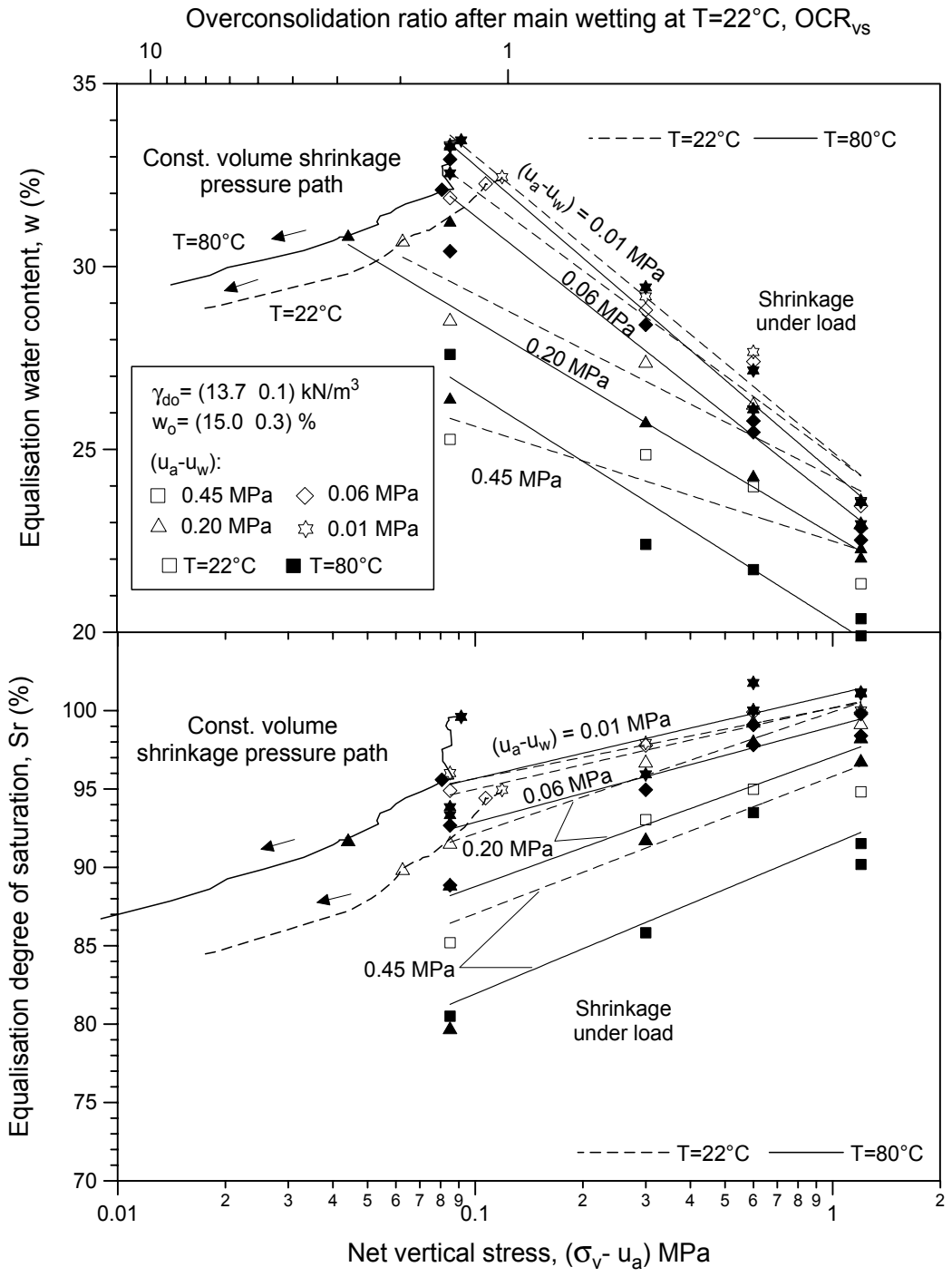

Figure 6.43 Water content and degree of saturation values for the high-porosity fabric at different temperatures and matric suction steps for varying applied net vertical stresses (main drying paths).

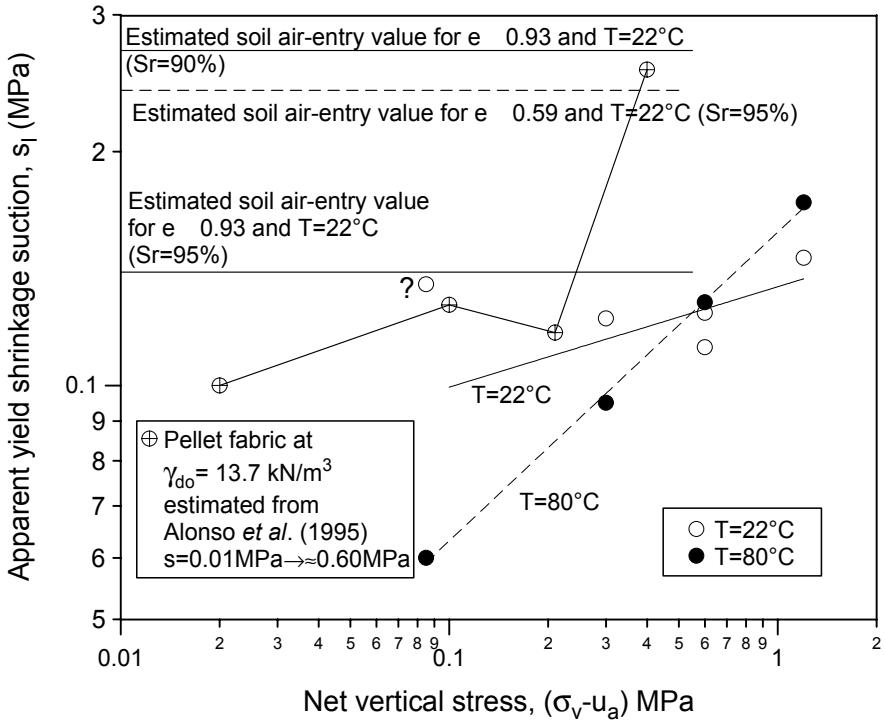

Figure 6.44 Apparent yield shrinkage suction for the high-porosity packing for different temperatures and vertical stress conditions (aggregated and pellet fabrics).

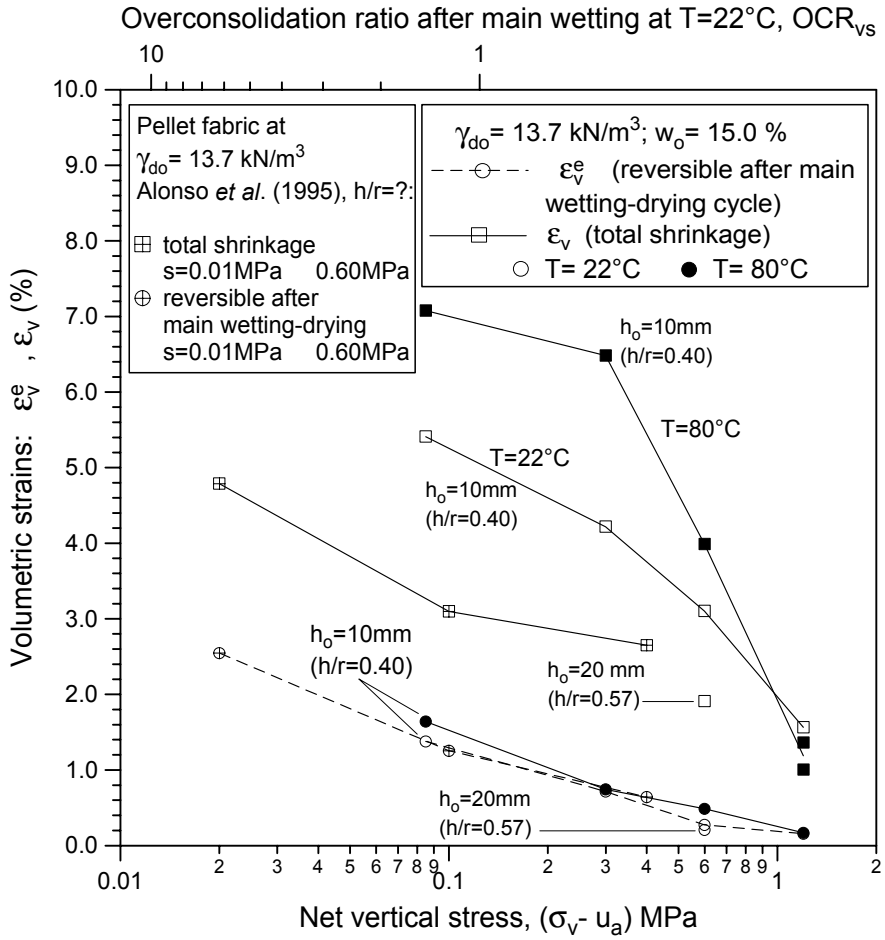

Figure 6.45 Total shrinkage upon main drying and reversible strain during scanning wetting at different temperatures and stress conditions (high-porosity packing).

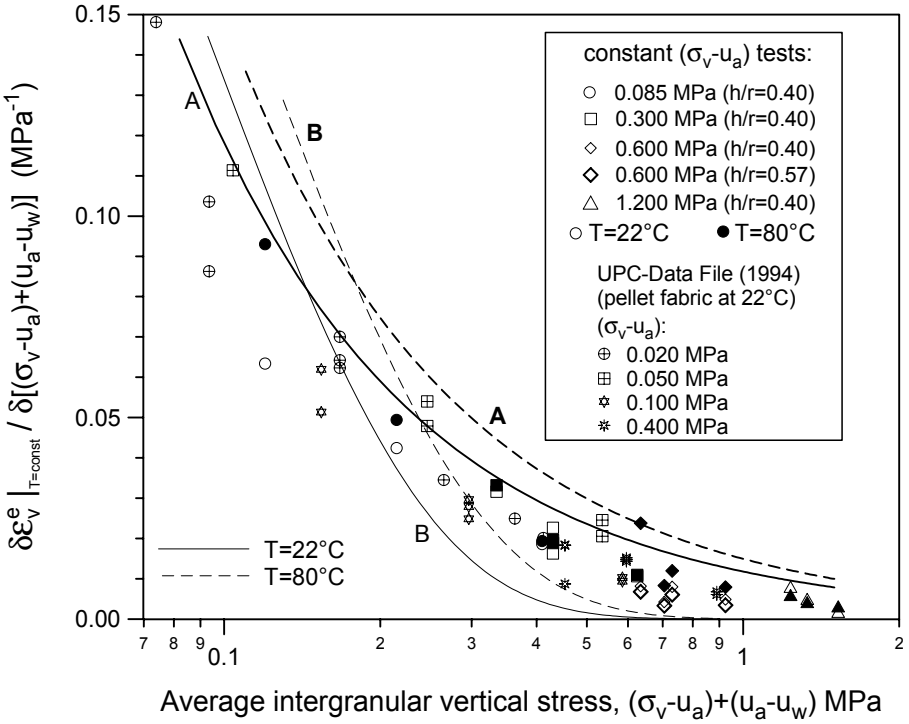

Figure 6.46 Isothermal changes in elastic strain associated with changes in intergranular vertical stress obtained from constant (σ_v-u_a) data (high-porosity aggregate and pellet fabrics).

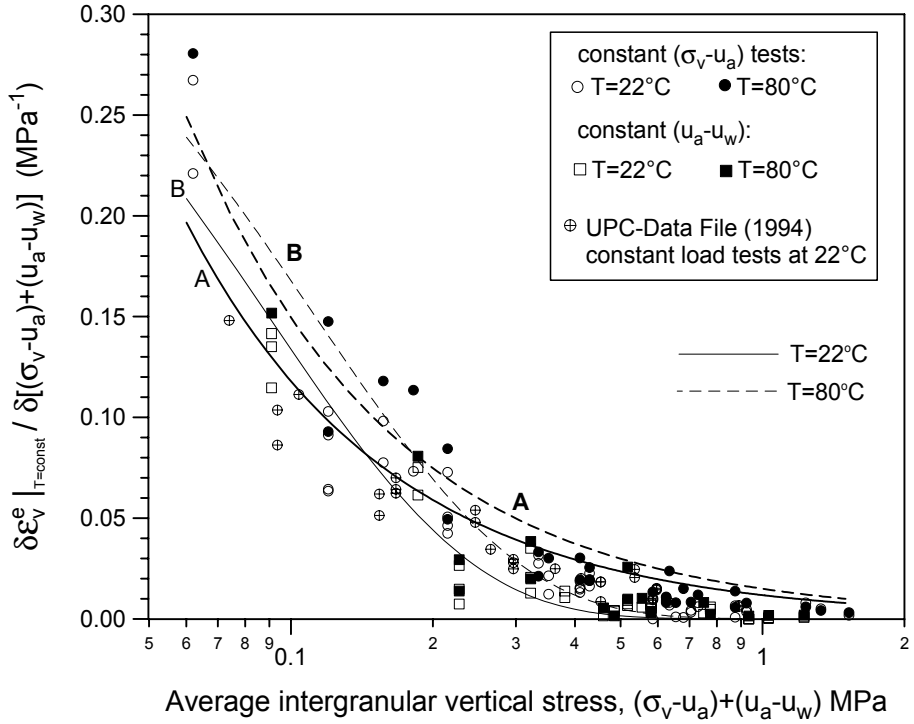

Figure 6.47 Isothermal changes in elastic strain associated with changes in intergranular vertical stress obtained from constant (σ_v-u_a) and (u_a-u_w) data (high-density and high-porosity fabrics).

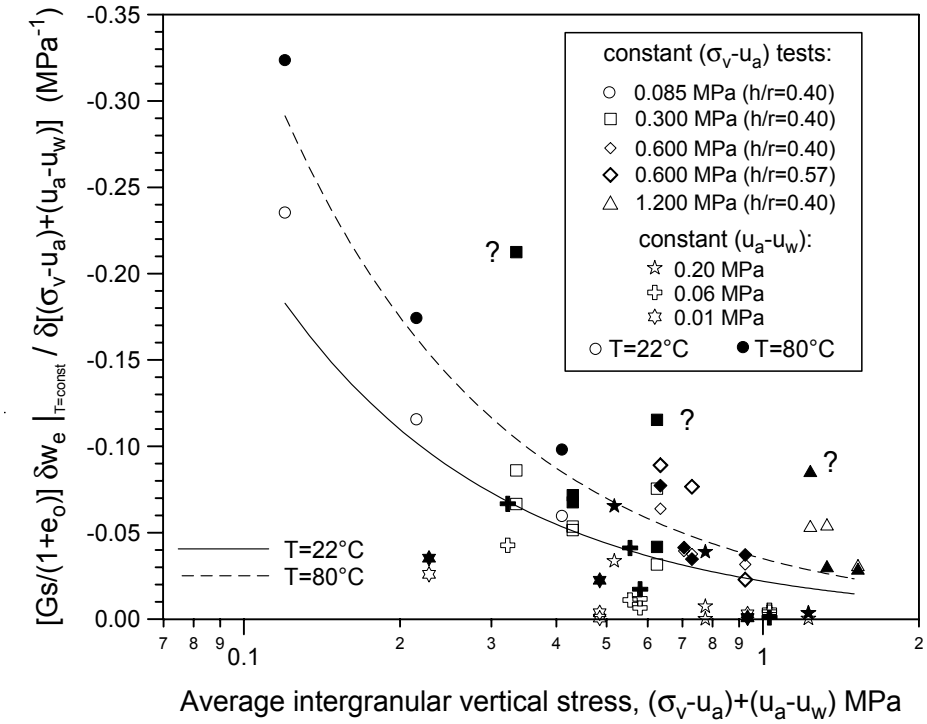

Figure 6.48 Isothermal reversible changes in work conjugate variable of matric suction with changes in intergranular vertical stress obtained from constant (σ_v-u_a) and (u_a-u_w) data (high-porosity fabric).

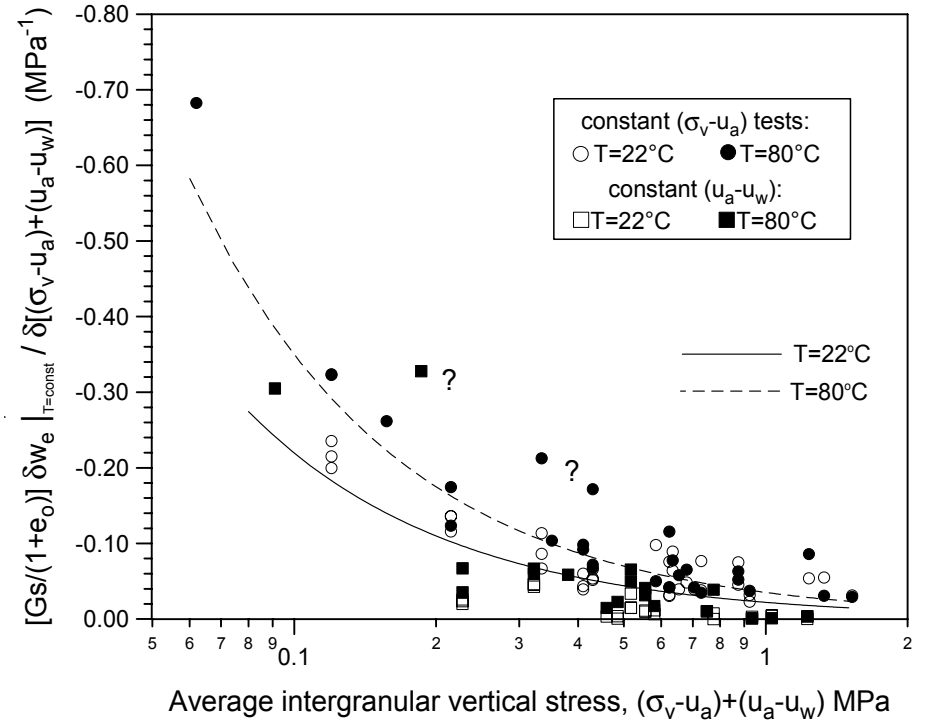

Figure 6.49 Isothermal reversible changes in work conjugate variable of matric suction with changes in intergranular vertical stress (high-density and high-porosity fabrics).

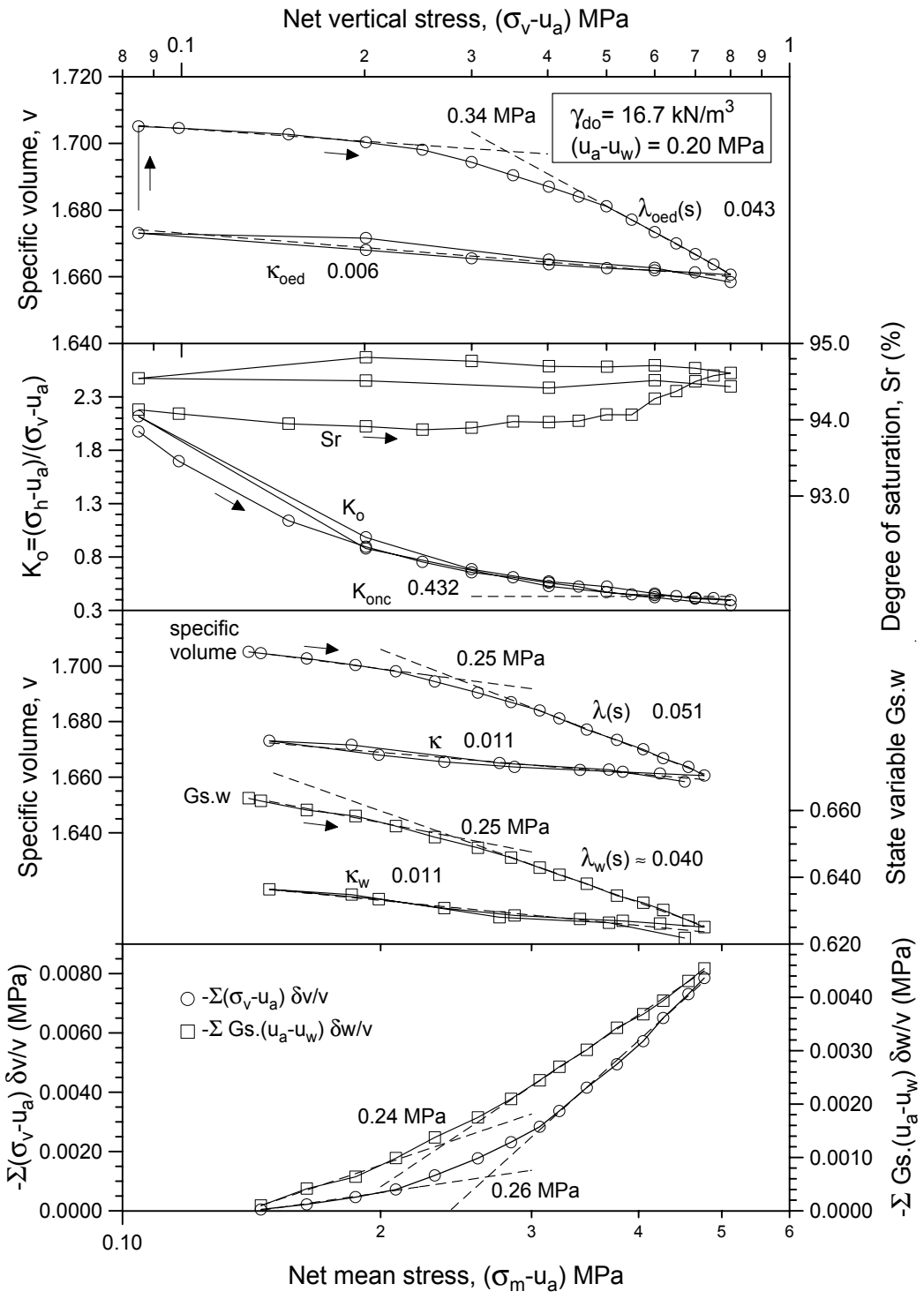

Figure 6.50 Loading-unloading paths on the high-density fabric at constant (u_a-u_w) = 0.20 MPa and T=22°C. Evolution of specific volume, degree of saturation, K_0 and state variable Gs.w.

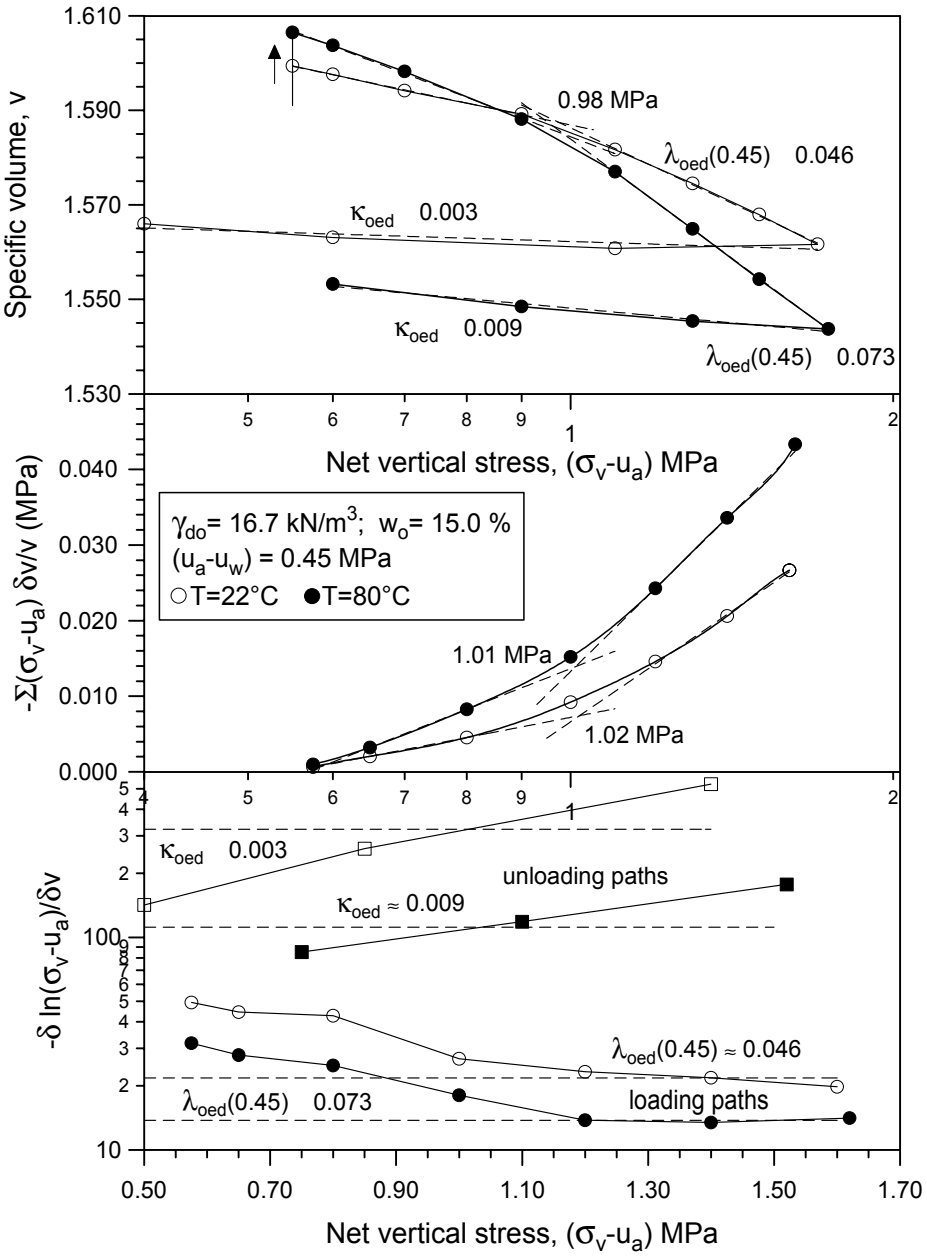

Figure 6.51 Loading-unloading paths on the high-density fabric at different temperatures and at constant (u_a-u_w) = 0.45 MPa.

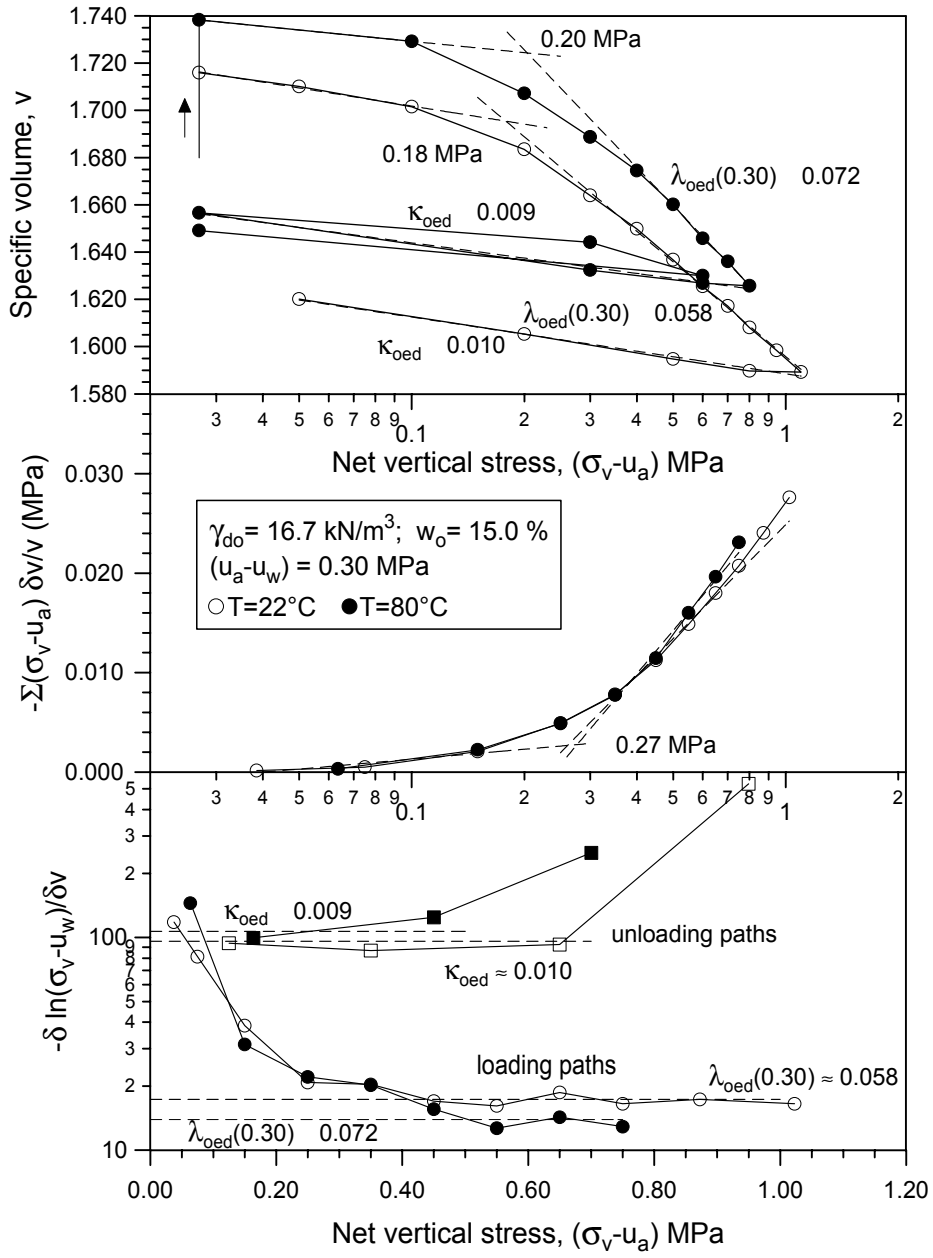

Figure 6.52 Loading-unloading paths on the high-density fabric at different temperatures and at constant (u_a-u_w) = 0.30 MPa.

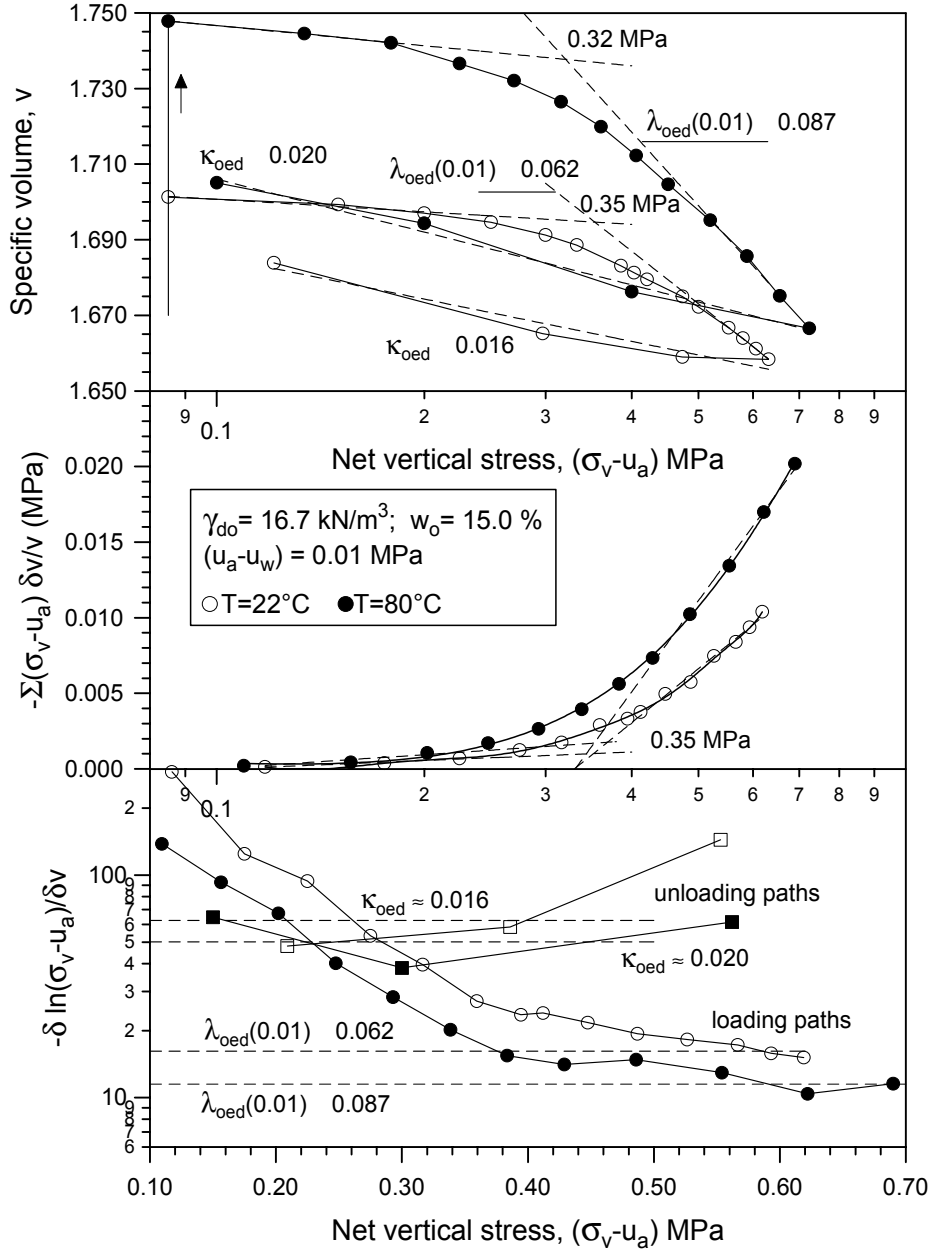

Figure 6.53 Loading-unloading paths on the high-density fabric at different temperatures and at constant (u_a-u_w) = 0.01 MPa.

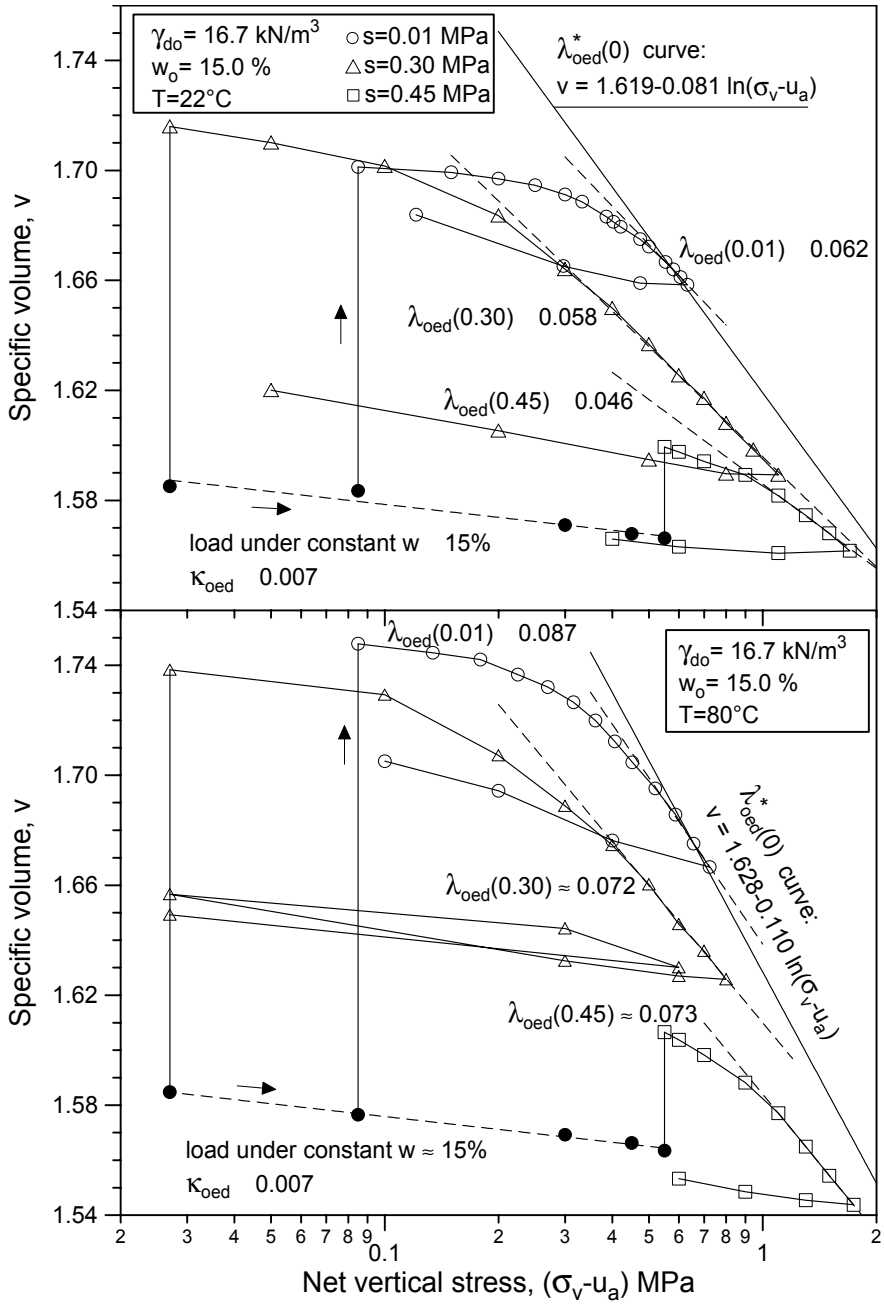

Figure 6.54 Specific volume : $\ln(\sigma_v\text{-}u_a)$ loading-unloading curves obtained at different matric suctions and temperatures (high-density fabric).

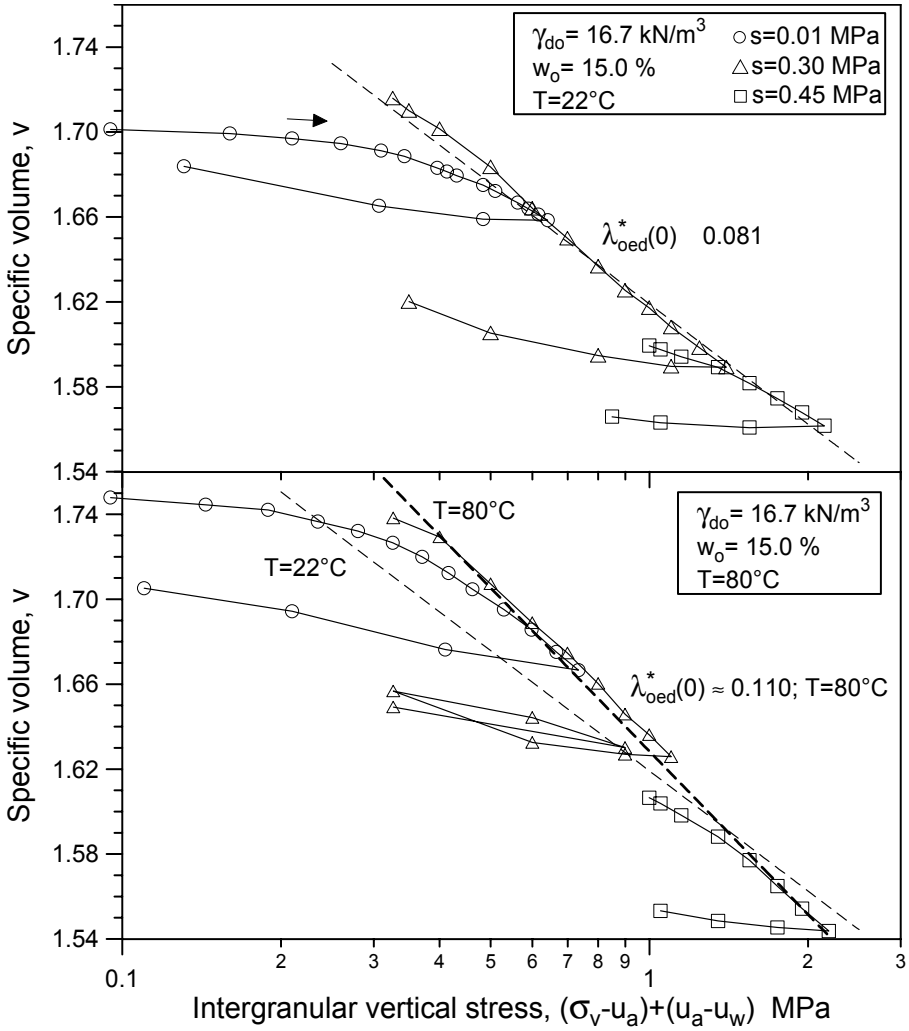

Figure 6.55 Specific volume : $\ln[(\sigma_v-u_a)+(u_a-u_w)]$ loading-unloading curves obtained at different matric suctions and temperatures (high-density fabric).

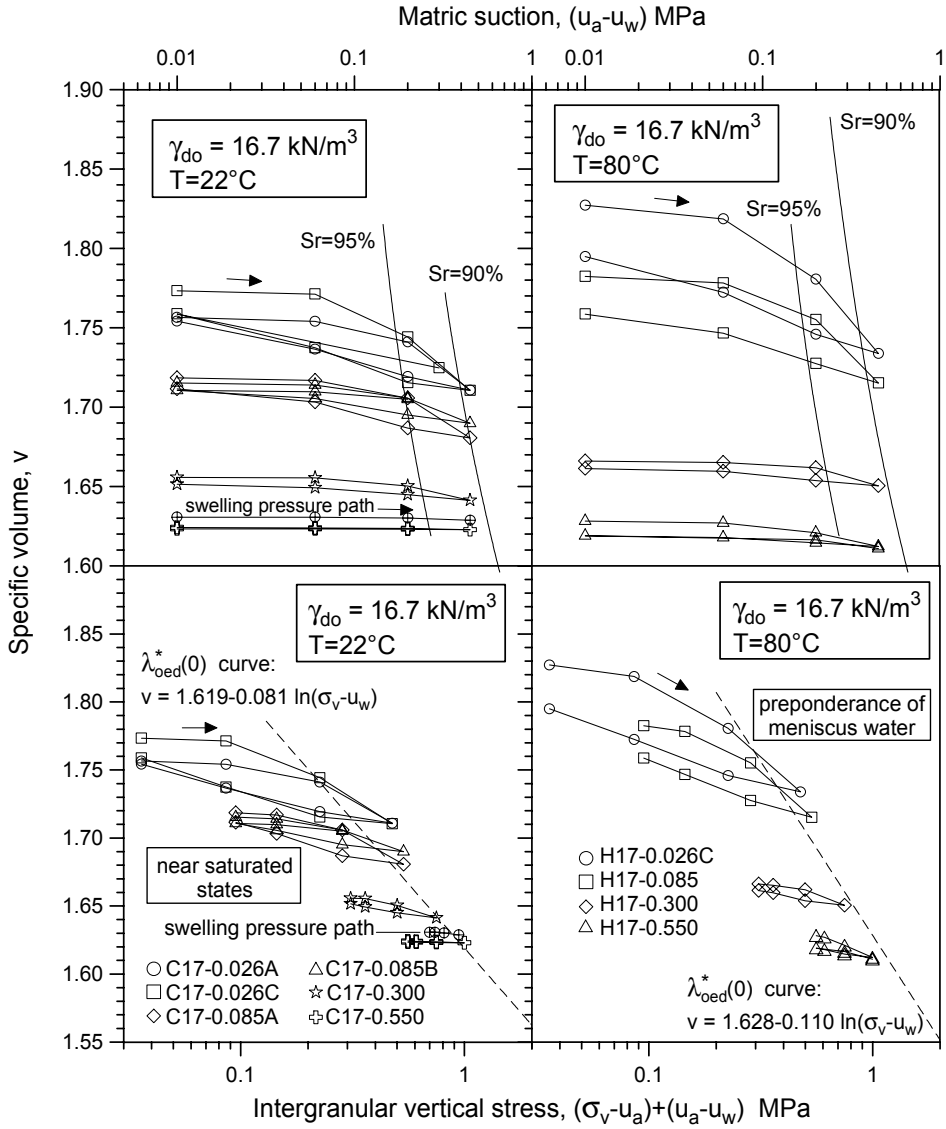

Figure 6.56 v : ln(σ_v-u_a) and v : ln[(σ_v-u_a)+(u_a-u_w)] plots in main drying-scanning wetting paths.

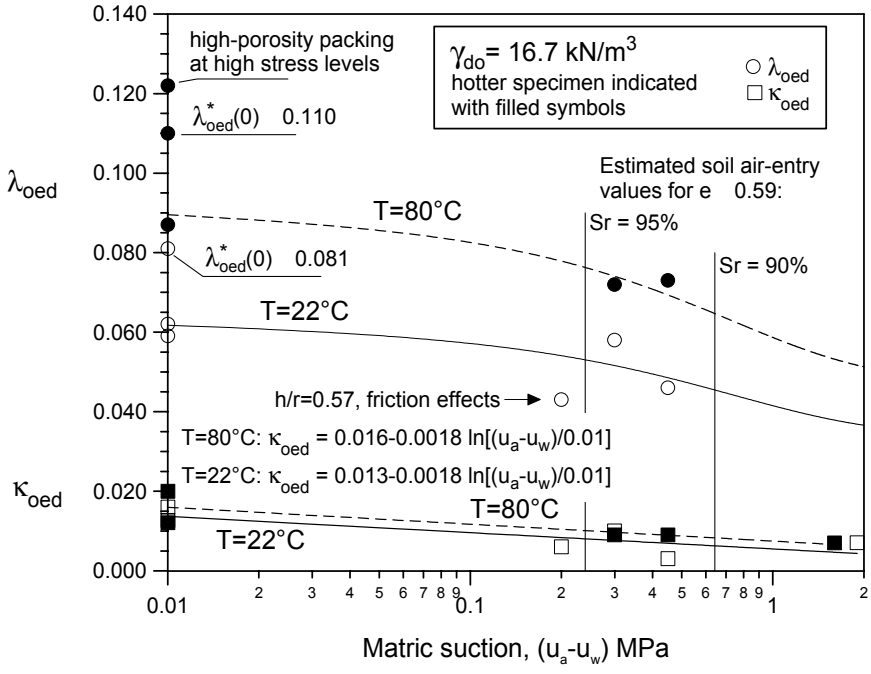

Figure 6.57 λ_{oed} and κ_{oed} values at different matric suctions and temperatures (high-density packing).

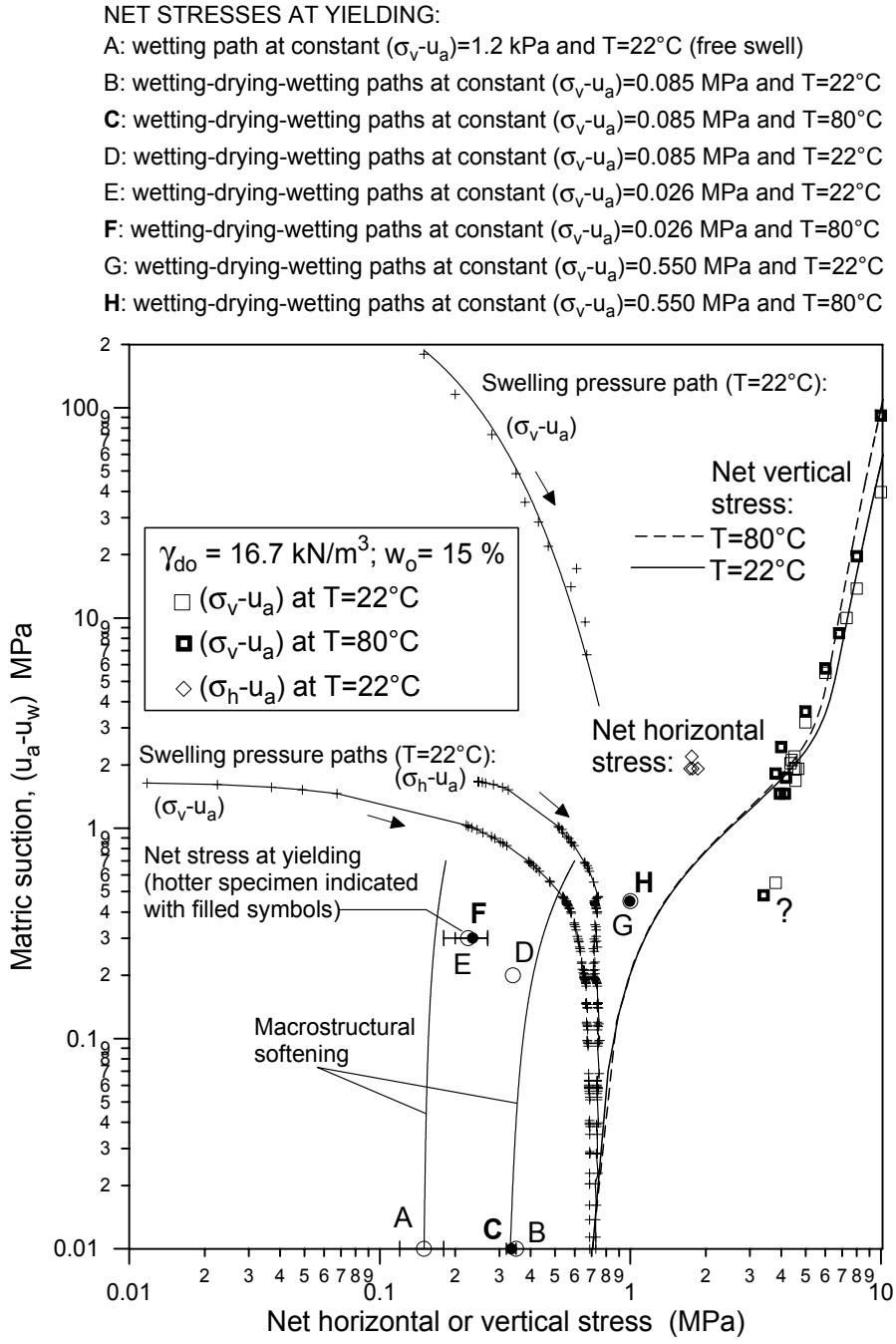

Figure 6.58 LC yield curve for the high-density fabric from static compaction and suction controlled tests. Macrostructural softening due to swelling.

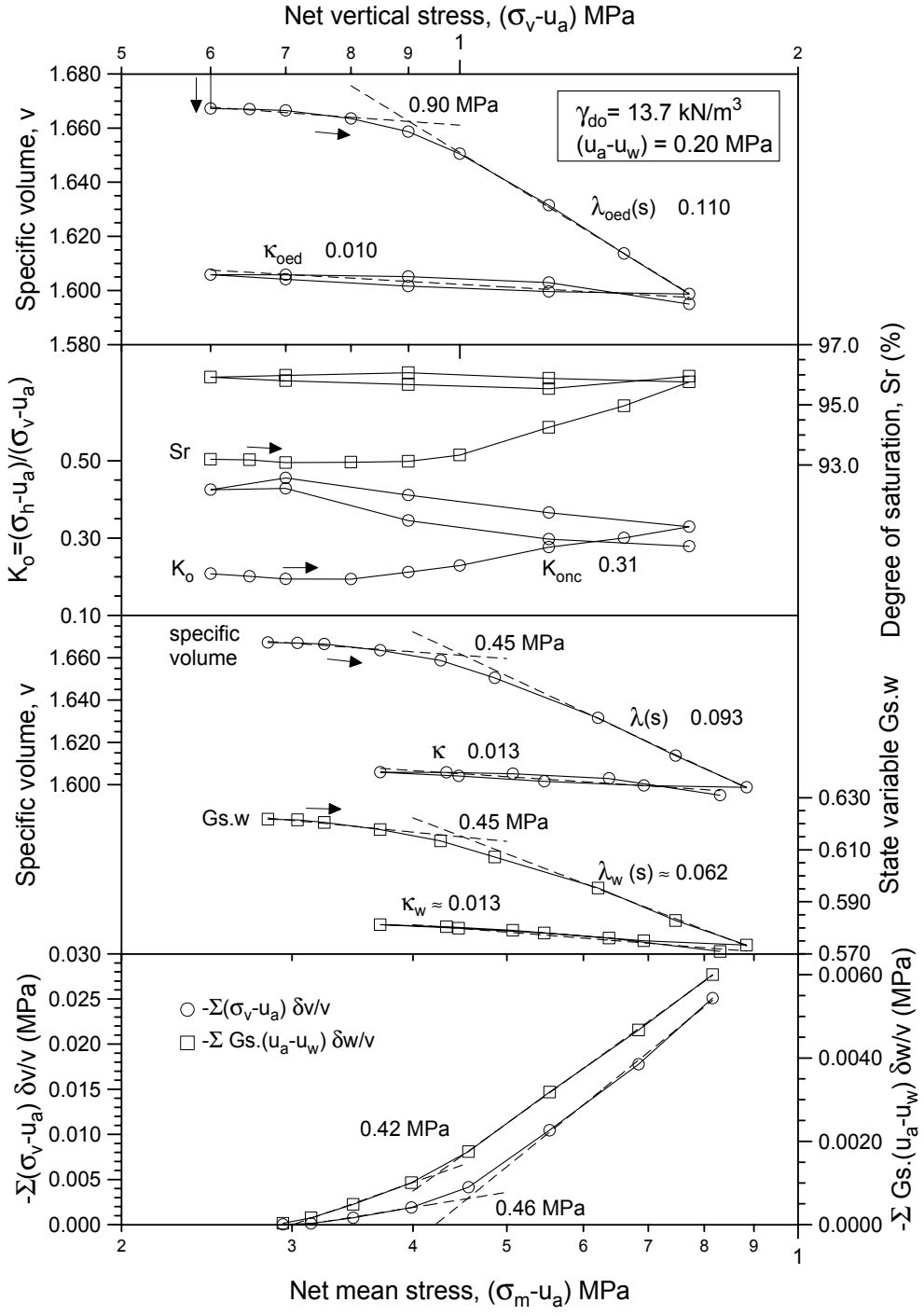

Figure 6.59 Loading-unloading paths on the high-porosity fabric at constant (u_a-u_w) = 0.20 MPa and T=22°C. Evolution of specific volume, degree of saturation, K_0 and state variable Gs.w.

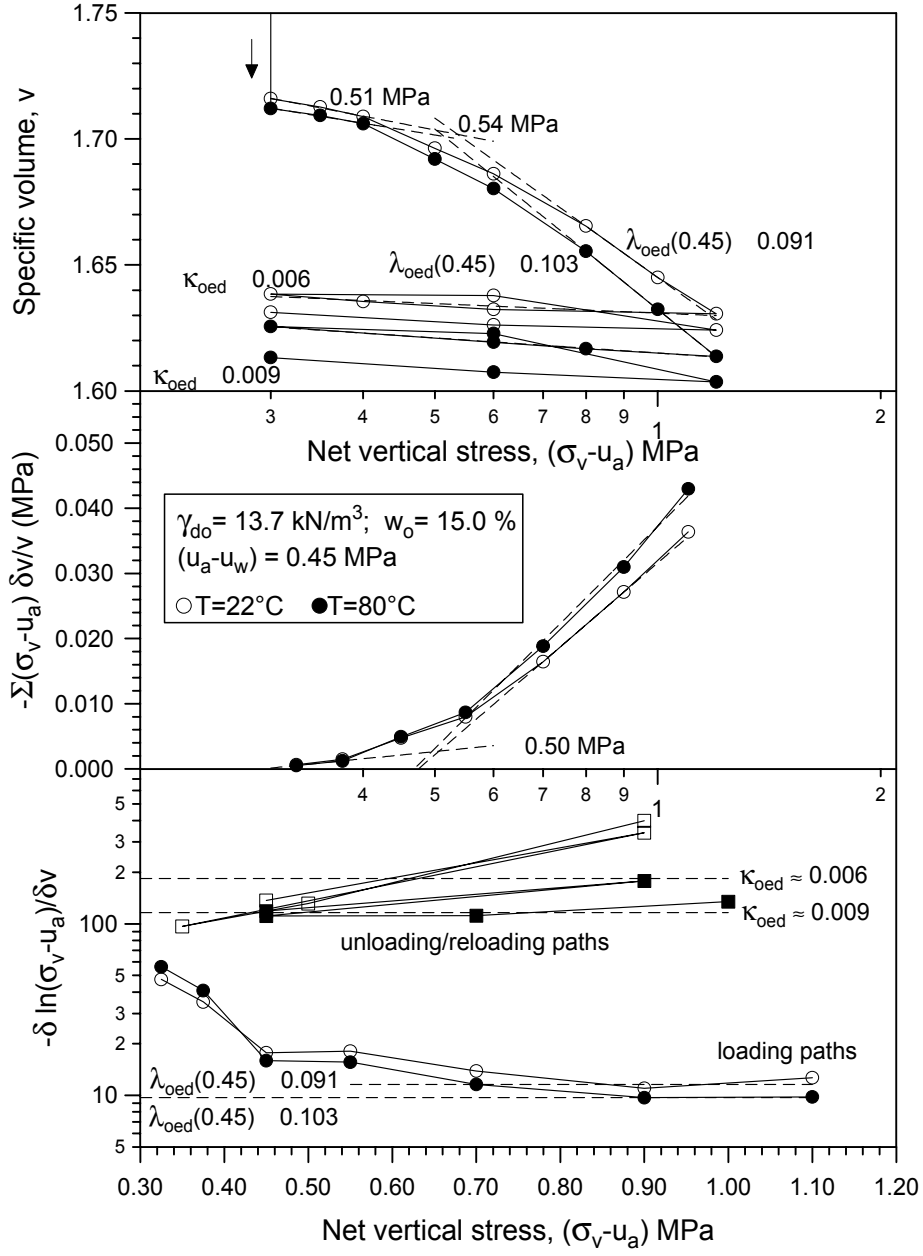

Figure 6.60 Loading-unloading paths on the high-porosity fabric at different temperatures and at constant (u_a-u_w) = 0.45 MPa.

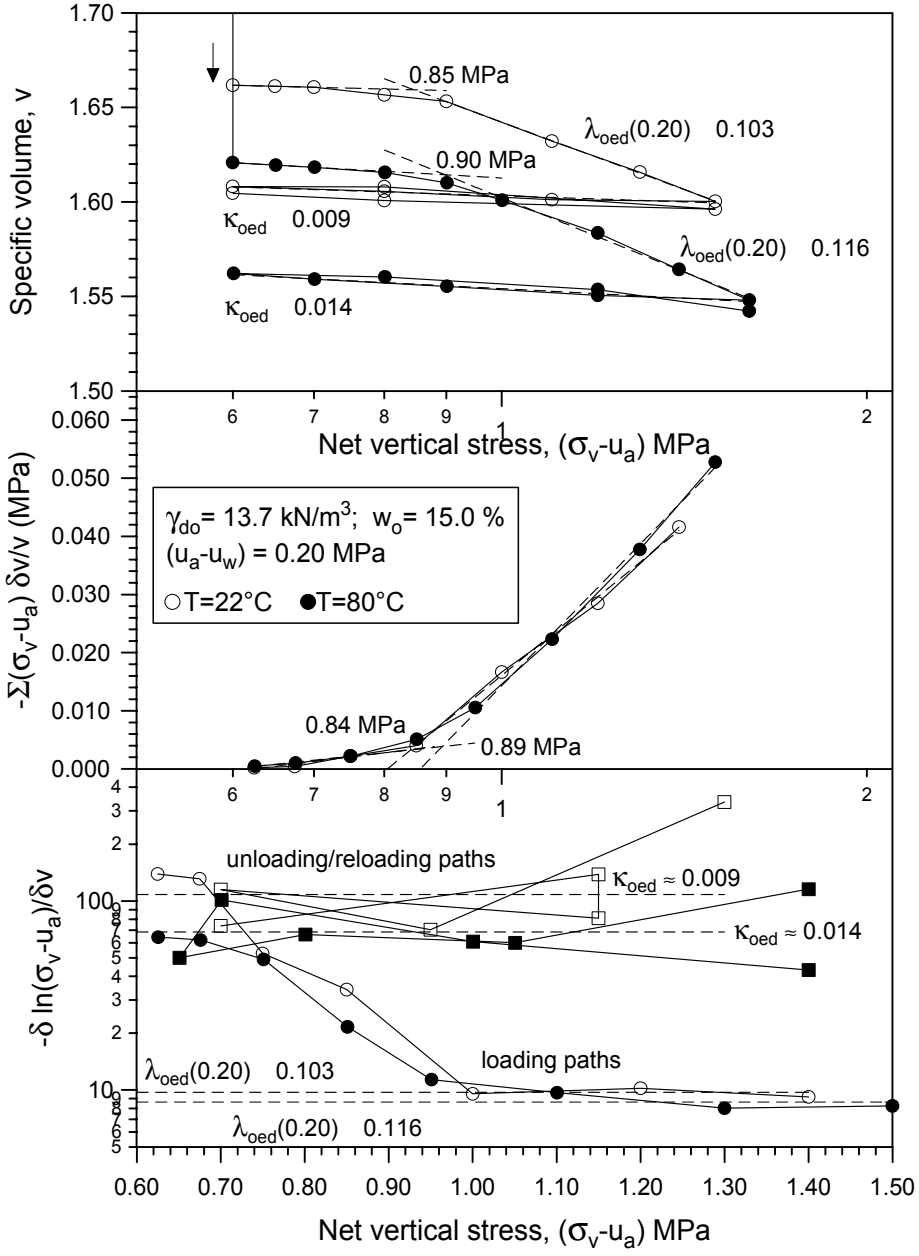

Figure 6.61 Loading-unloading paths on the high-porosity fabric at different temperatures and at constant (u_a-u_w) = 0.20 MPa.

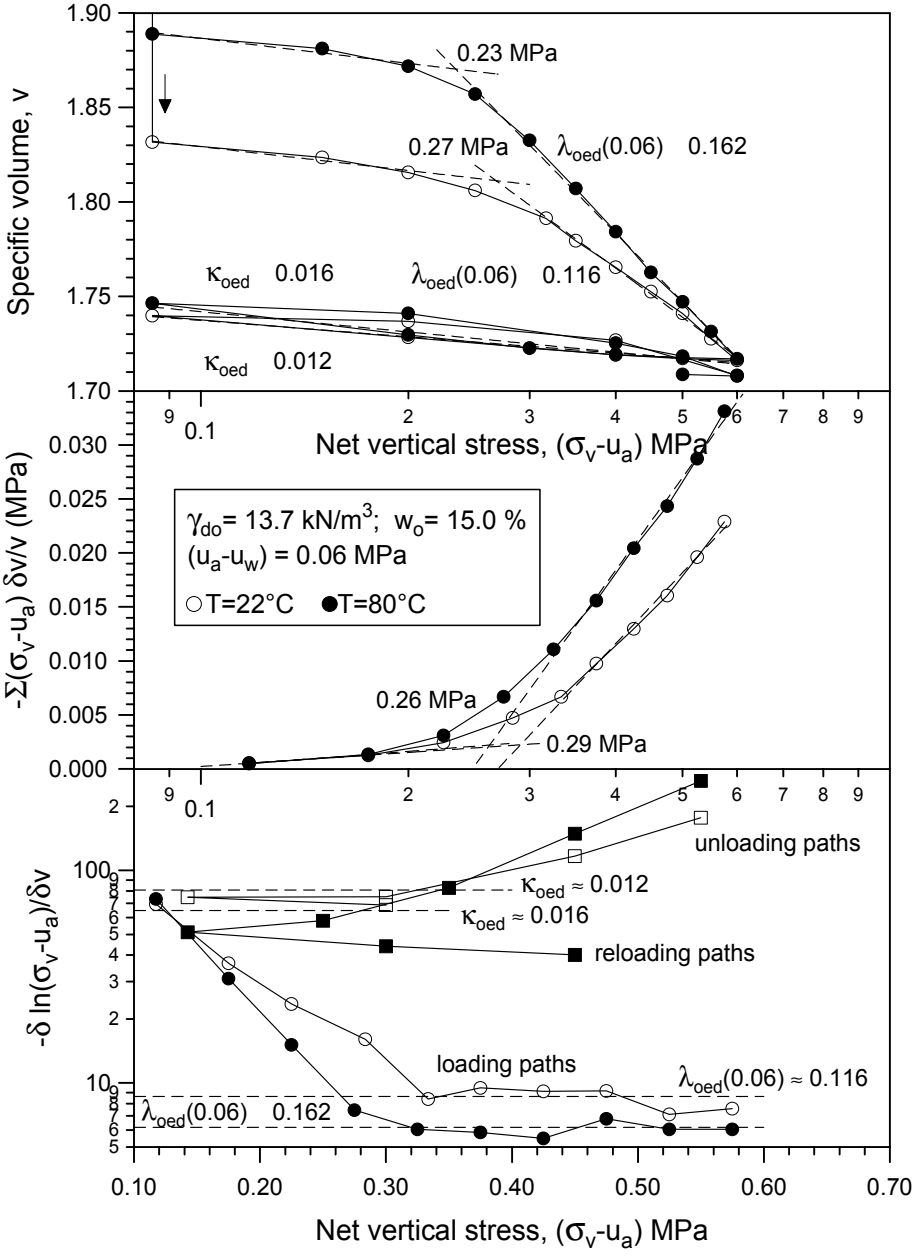

Figure 6.62 Loading-unloading paths on the high-porosity fabric at different temperatures and at constant (u_a-u_w) = 0.06 MPa.

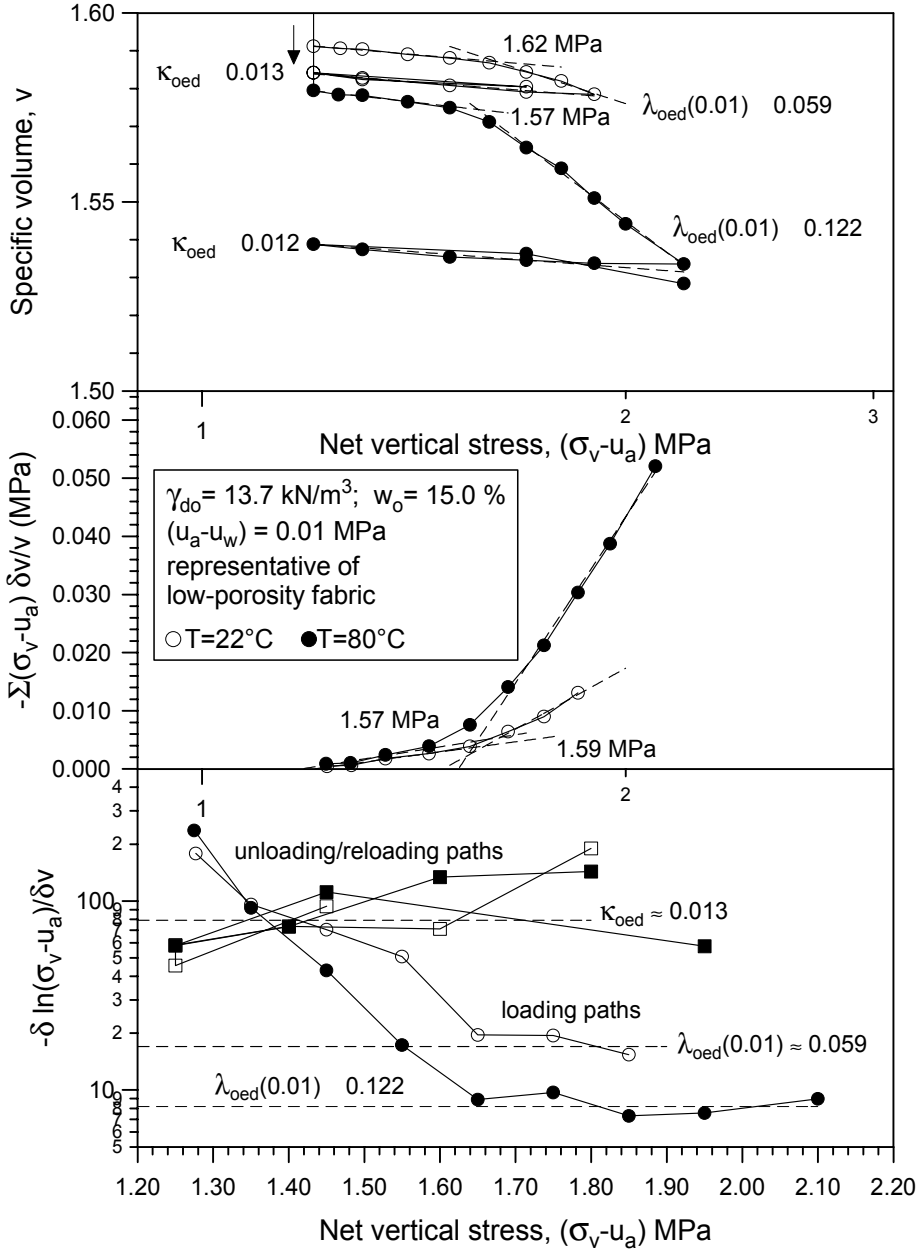

Figure 6.63 Loading-unloading paths on the high-porosity fabric at different temperatures and at constant $(u_a-u_w) = 0.01$ MPa.

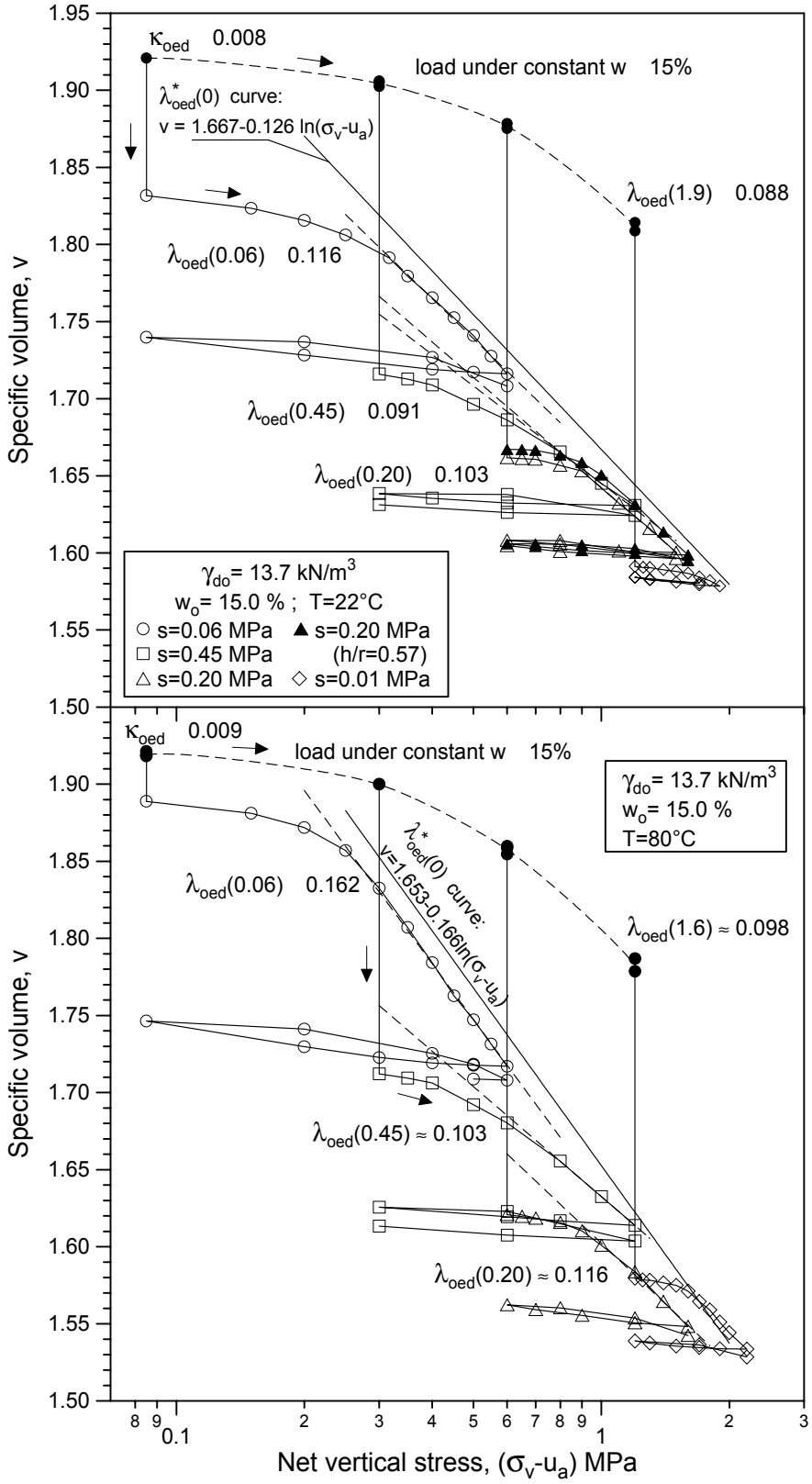

Figure 6.64 Specific volume : $\ln(\sigma_v\text{-}u_a)$ loading-unloading curves obtained at different matric suctions and temperatures (high-porosity fabric).

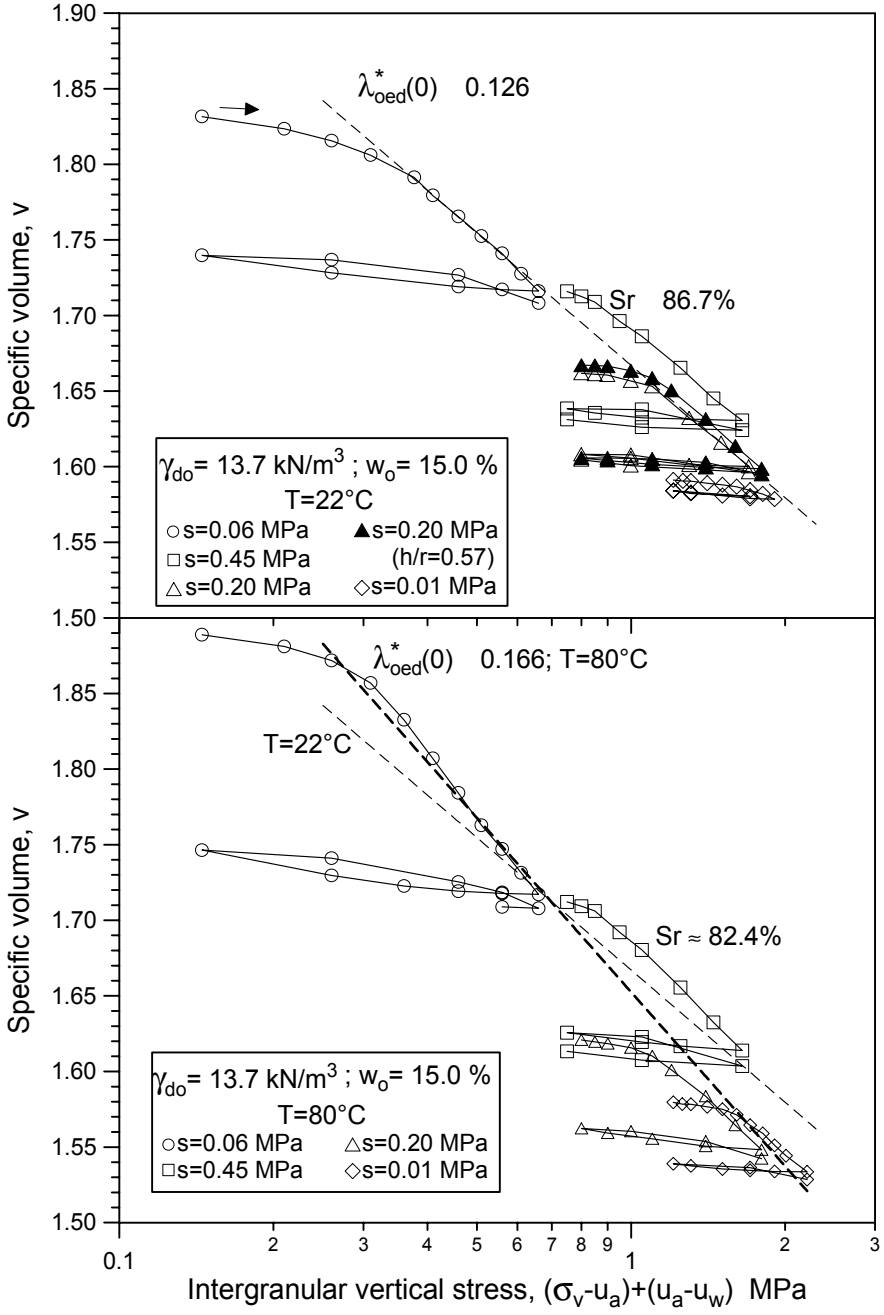

Figure 6.65 Specific volume : $\ln[(\sigma_v-u_a)+(u_a-u_w)]$ loading-unloading curves obtained at different matric suctions and temperatures (high-porosity fabric).

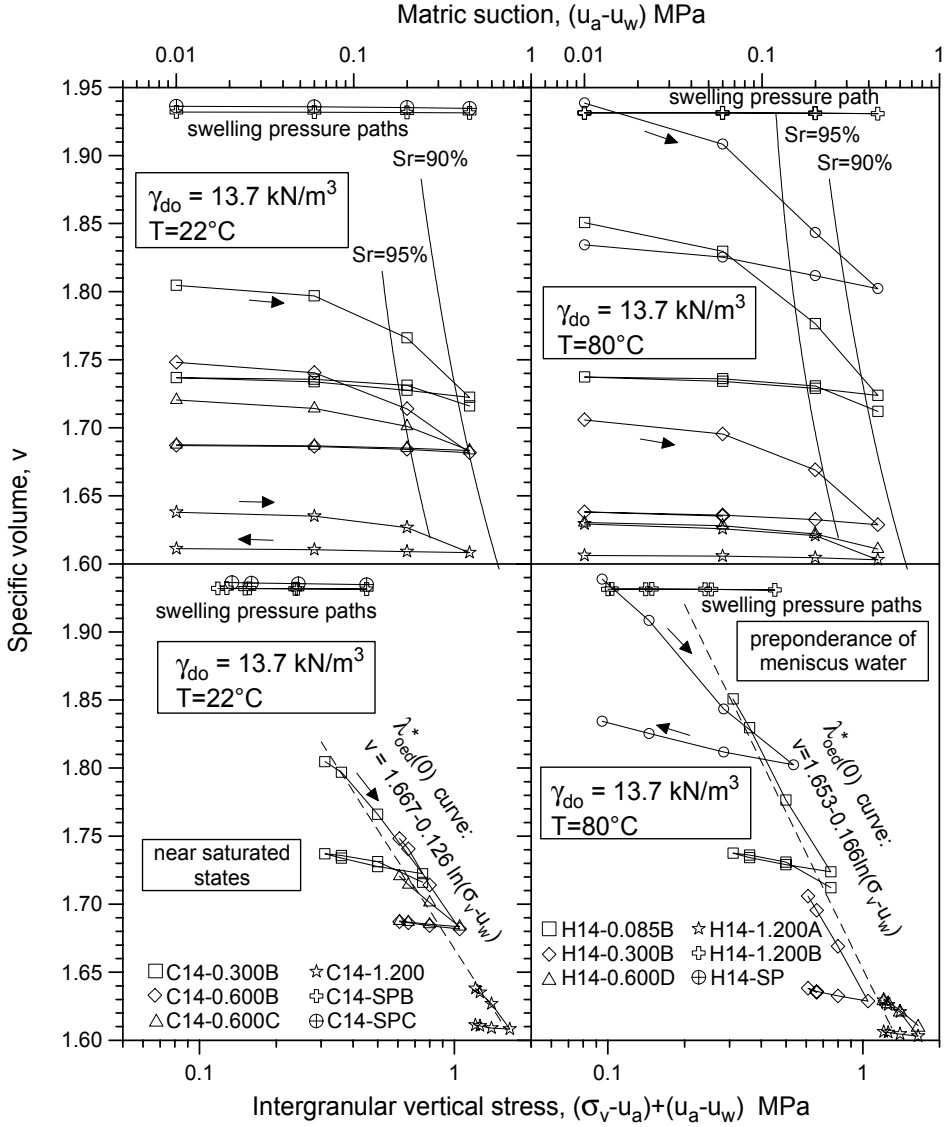

Figure 6.66 Specific volume : $\ln(\sigma_v-u_a)$ and specific volume : $\ln[(\sigma_v-u_a)+(u_a-u_w)]$ main drying-scanning wetting curves obtained at different matric suctions and temperatures (high-porosity fabric).

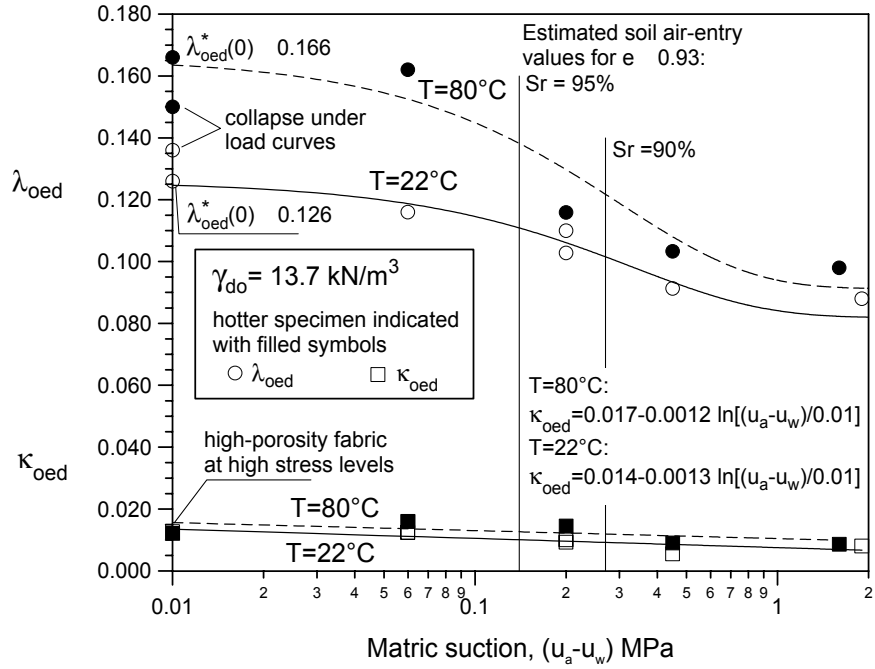

Figure 6.67 λ_{oed} and κ_{oed} values at different matric suctions and temperatures (high-porosity packing).

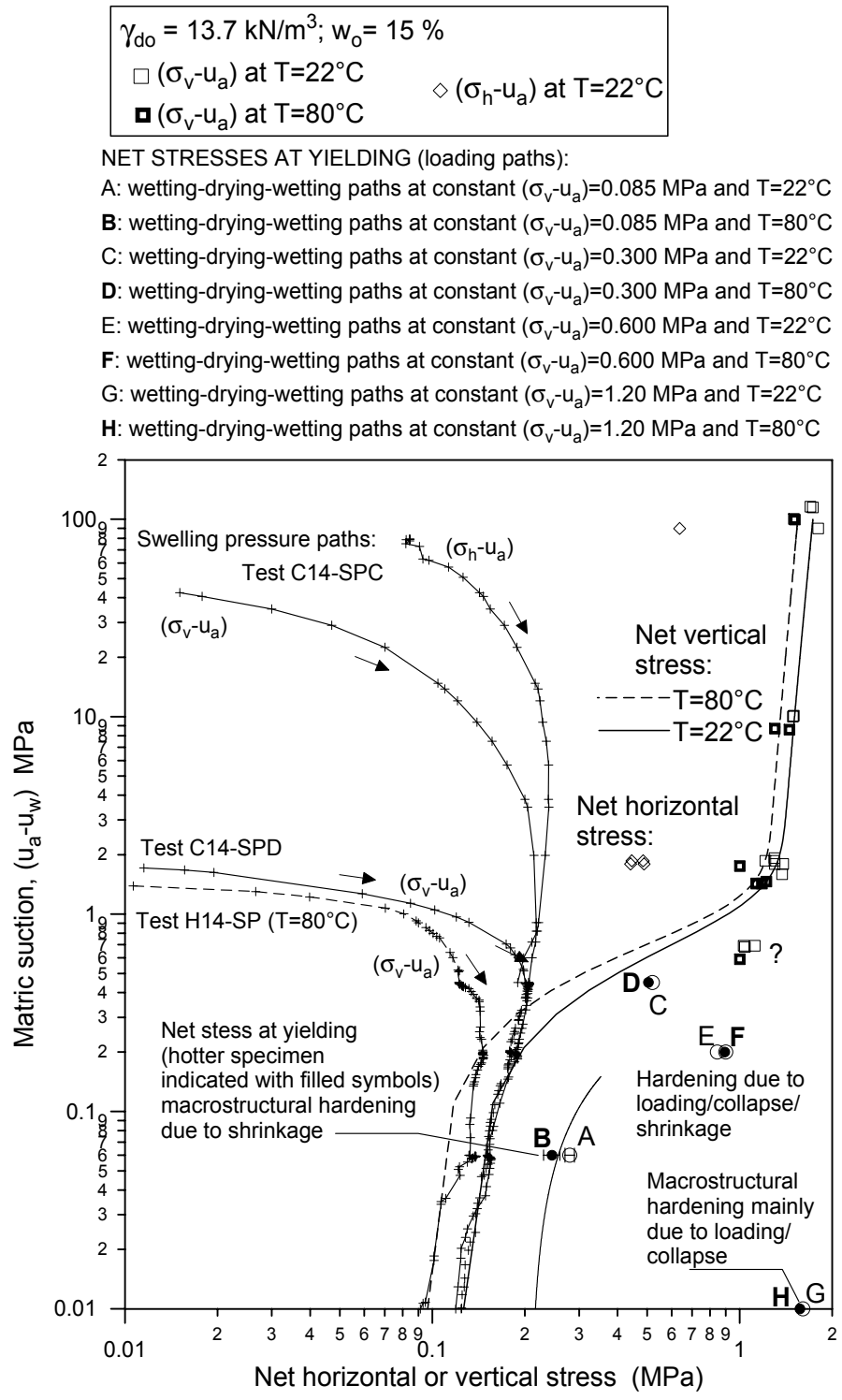

Figure 6.68 LC yield curve for the high-porosity fabric from static compaction and suction controlled tests. Macrostructural hardening due to collapse.

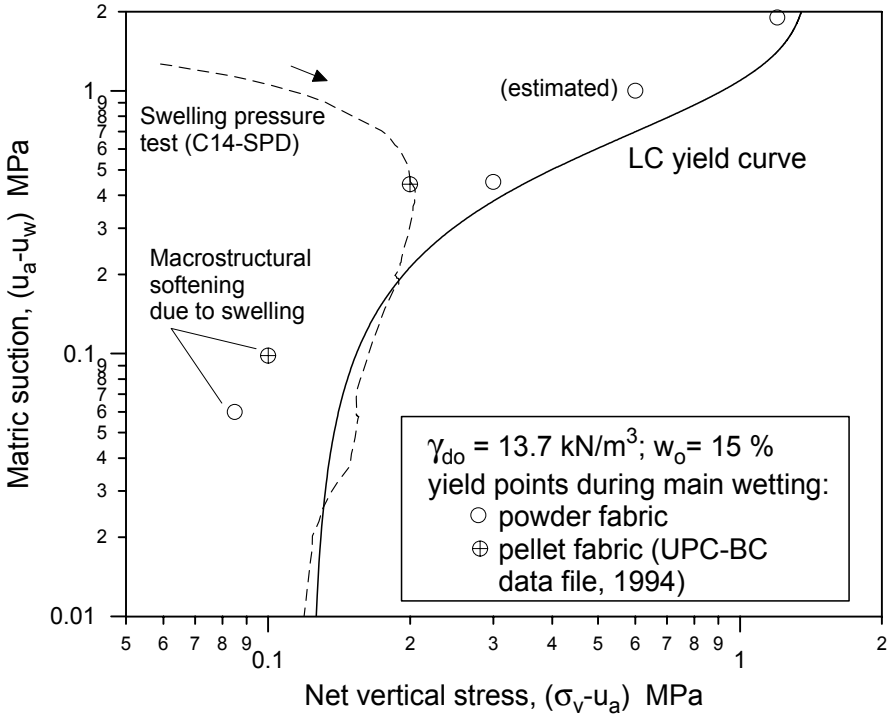

Figure 6.69 LC yield curve and yield points during main wetting (high-porosity fabric).

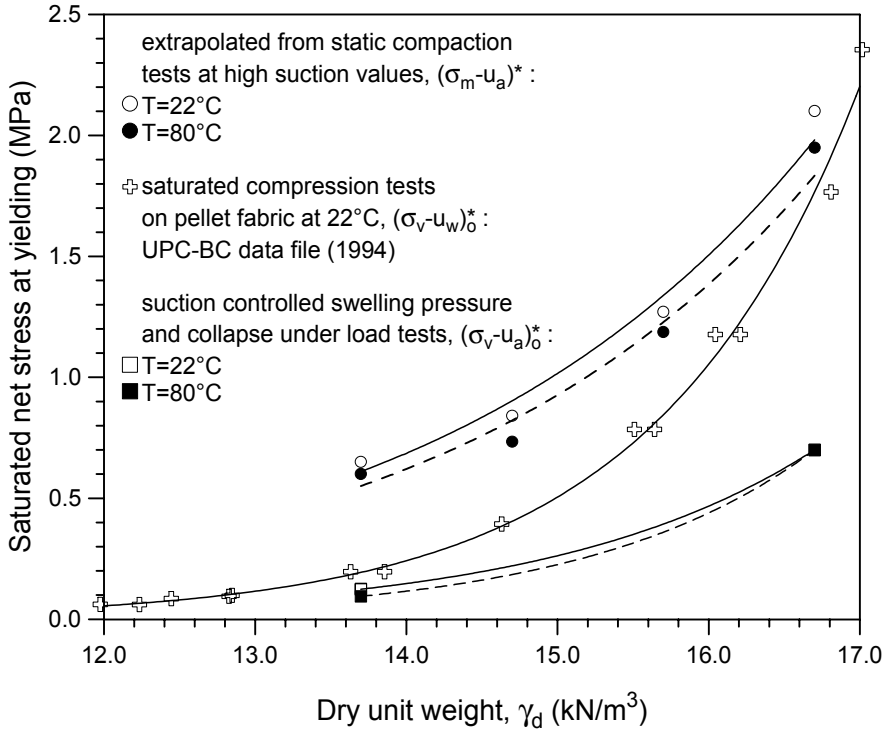

Figure 6.70 Saturated net stress at yielding obtained from static compaction, compression and suction controlled tests as a function of dry unit weight.

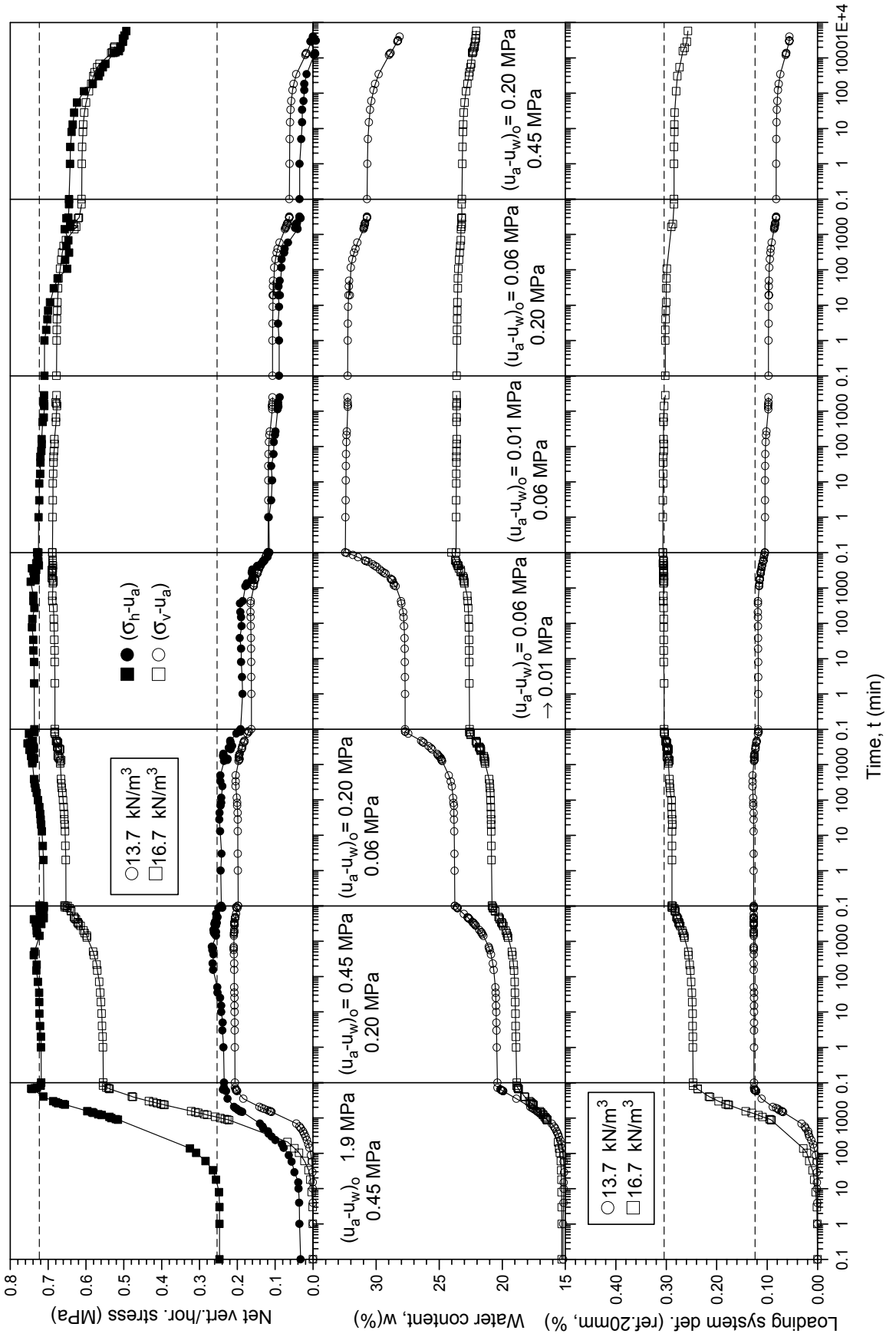

Figure 6.71 Time evolution of vertical and lateral swelling pressures, water content and loading system compressibility in a main wetting-drying cycle (high-density and high-porosity fabrics).

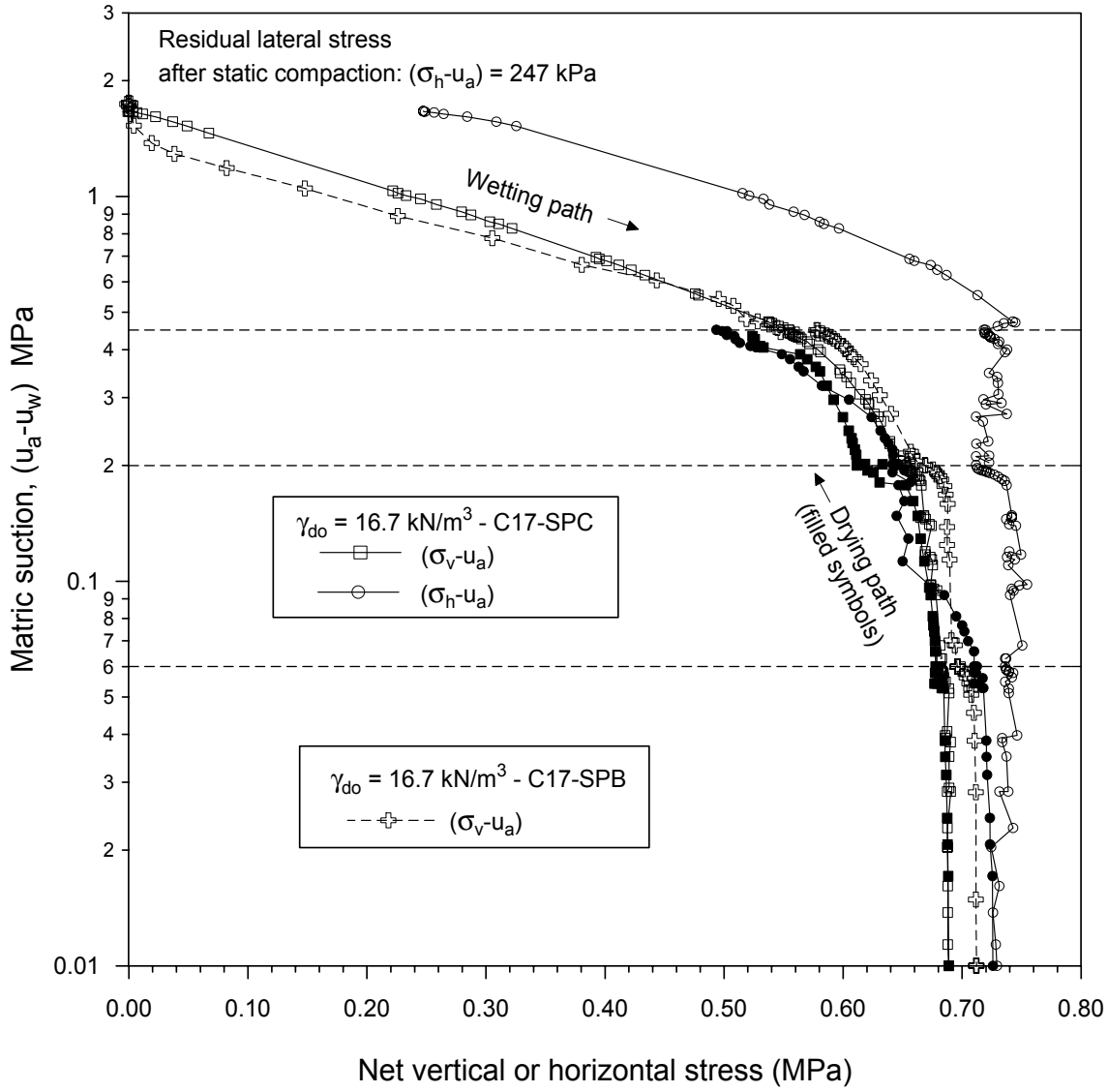

Figure 6.72 Vertical and horizontal swelling and shrinkage pressure paths in the high-density packing.

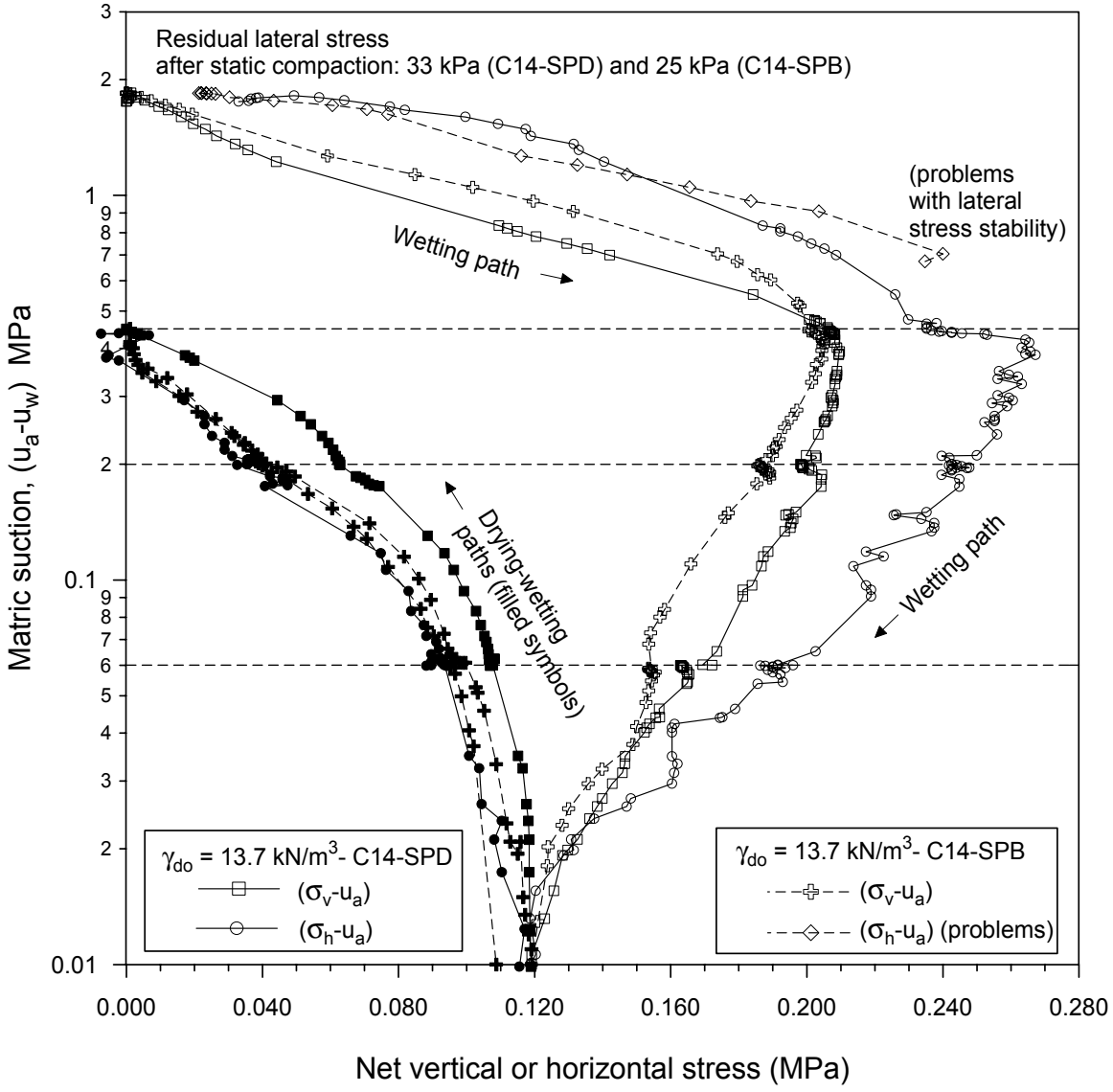

Figure 6.73 Vertical and horizontal swelling and shrinkage pressure paths in the high-porosity packing.

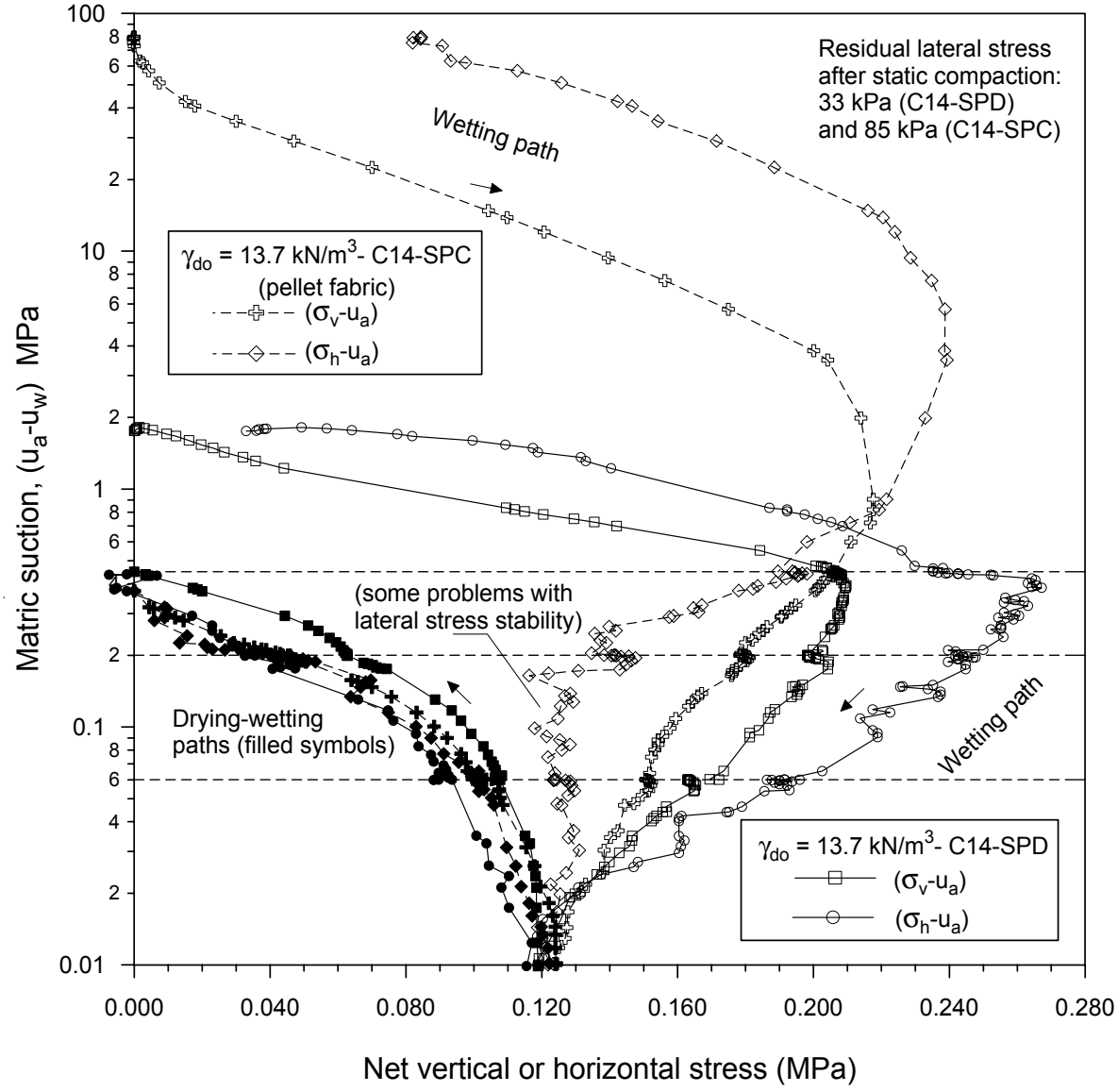

Figure 6.74 Vertical and horizontal swelling and shrinkage pressure paths in the high-porosity packing (comparison of pellet and aggregated fabrics).

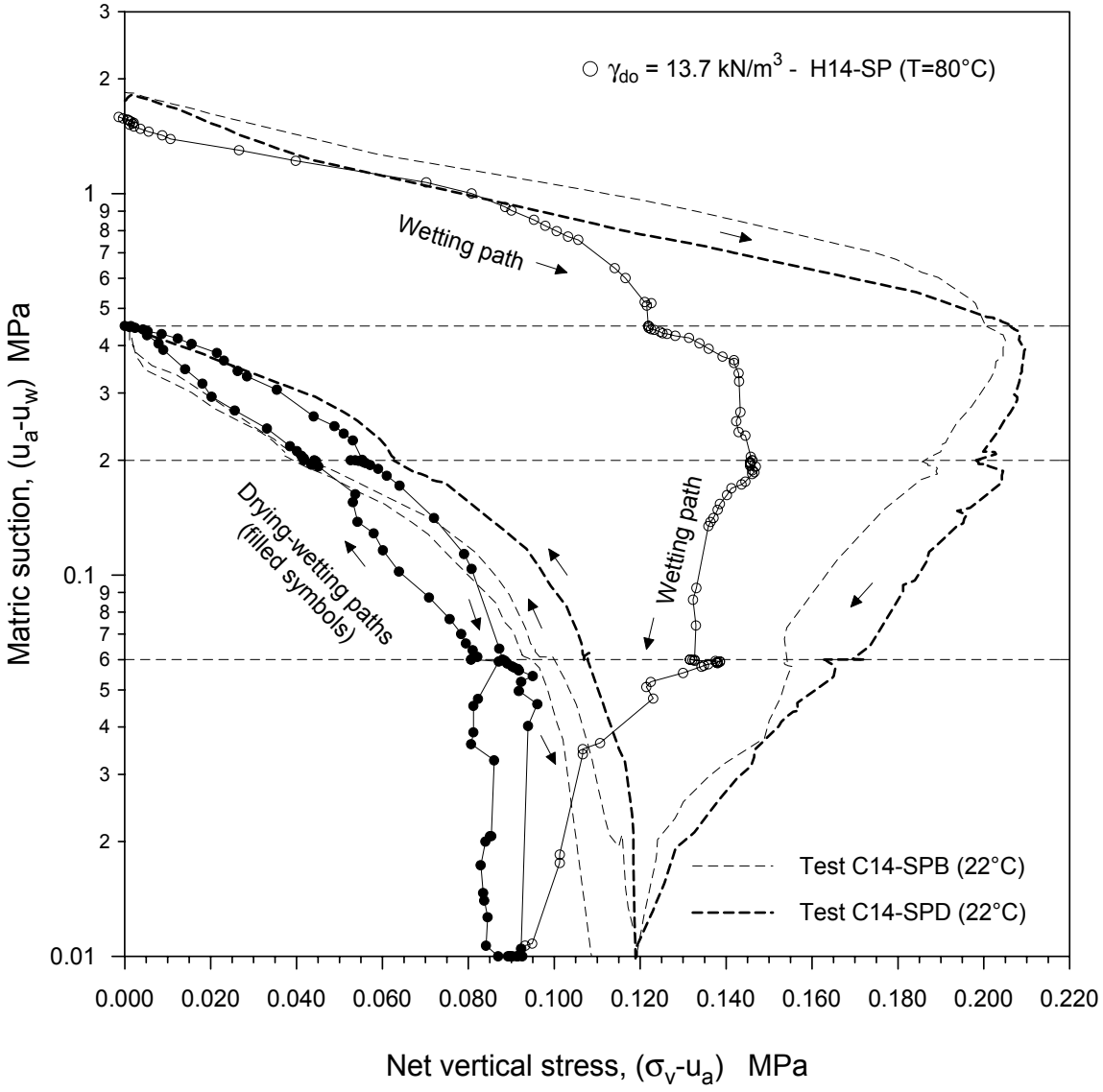

Figure 6.75 Vertical swelling and shrinkage pressure paths in the high-porosity packing at different temperatures.

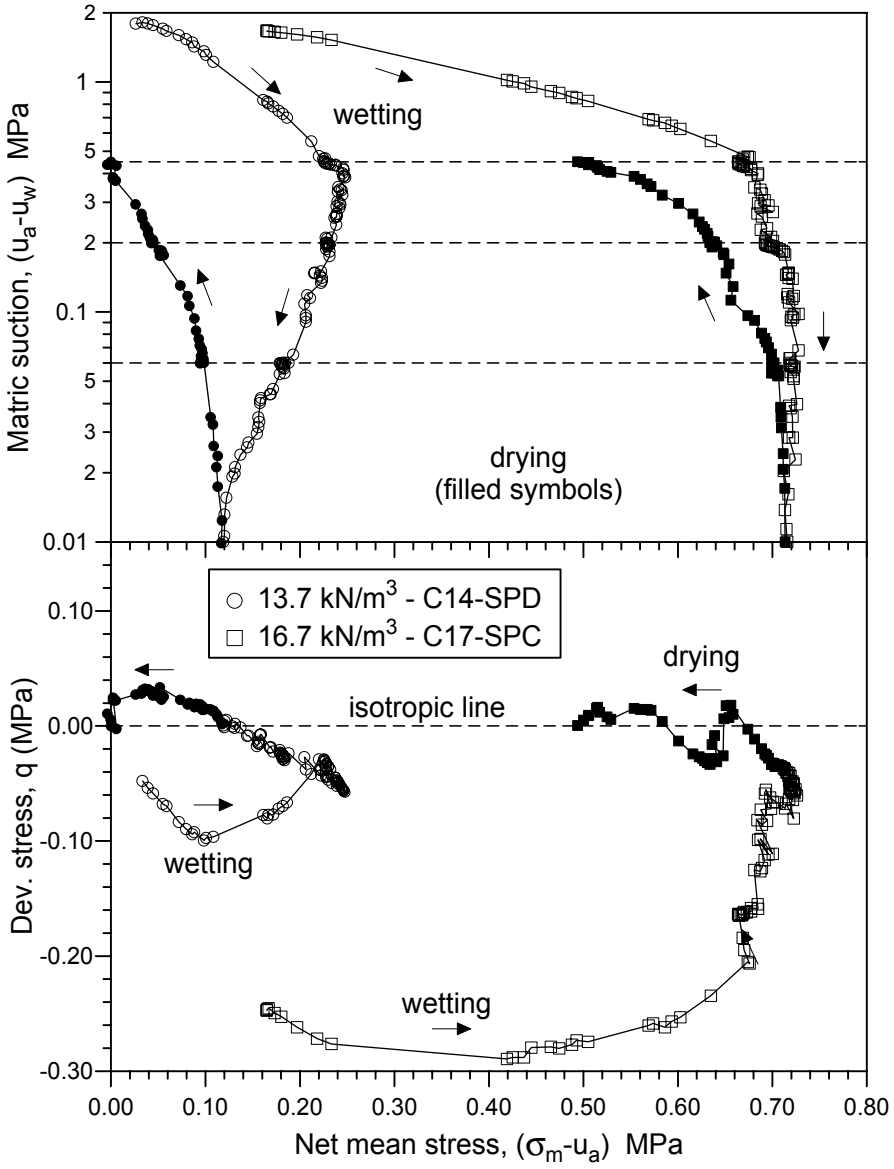

Figure 6.76 Swelling and shrinkage pressure paths in s : p and q : p planes for both packings.

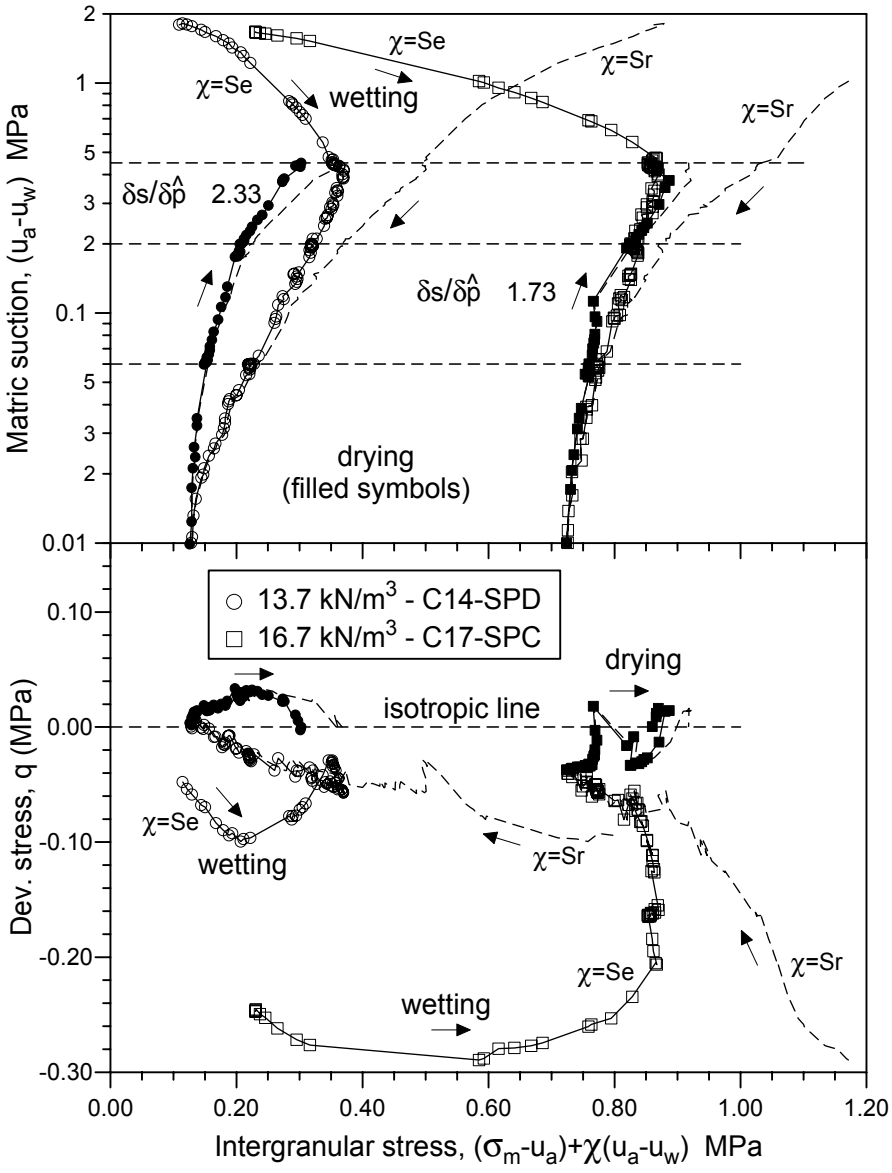

Figure 6.77 Swelling and shrinkage pressure paths in $s:\hat{p}$ and $q:\hat{p}$ planes for both packings.

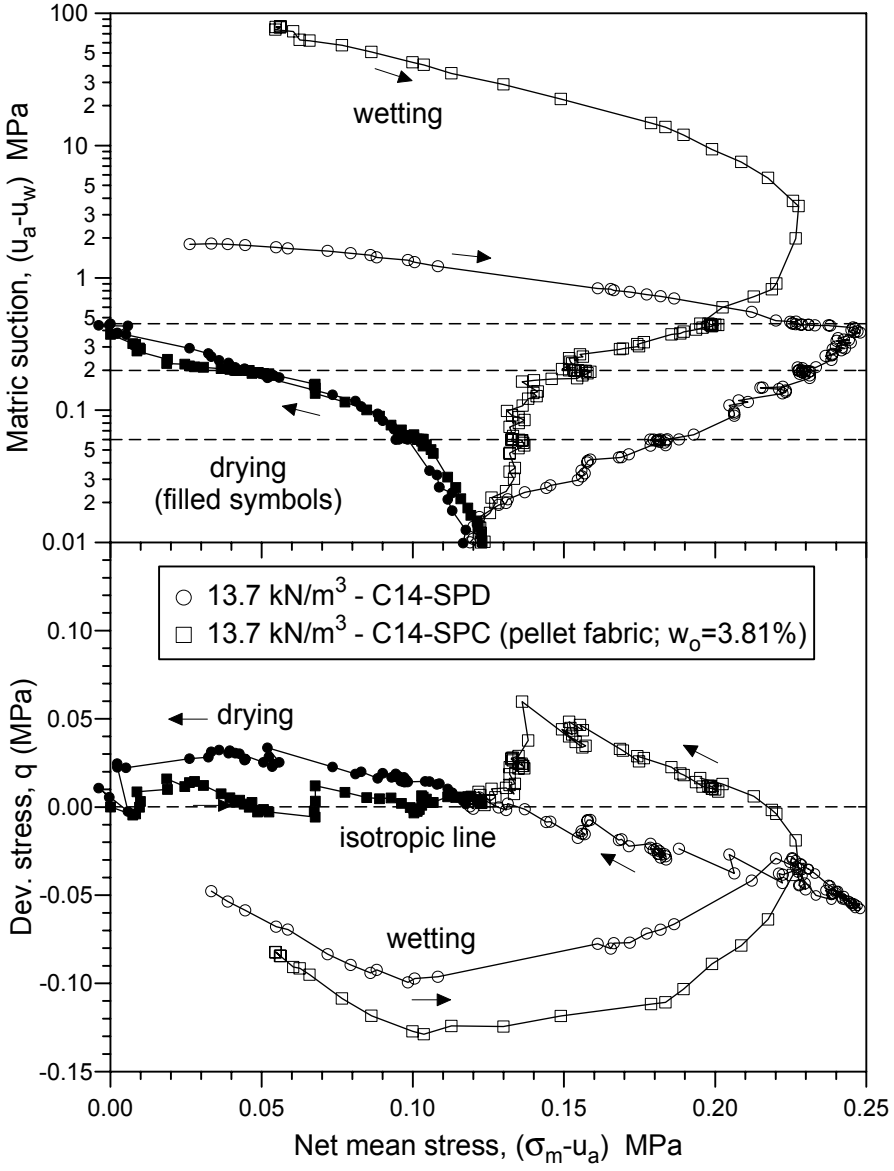

Figure 6.78 Swelling and shrinkage pressure paths in s : p and q : p planes for the high-porosity packing (pellet and aggregated fabrics).